Creation of Morphology Controlled TiO_2 Nanoparticle Assemblies with Unique Surface Structures and their Applications

by

DURIYASART Farkfun
Student ID Number: 1196009

A dissertation submitted to the
Engineering Course, Department of Engineering,
Graduate School of Engineering,
Kochi University of Technology,
Kochi, Japan

in partial fulfillment of the requirements for the degree of
Doctor of Philosophy

Assessment Committee:
Supervisor: Kazuya Kobiro
Co-Supervisor: Ryuichi Sugimoto
Co-Supervisor: Nagatoshi Nishiwaki
Akimitsu Hatta
Masataka Ohtani
Masayoshi Fuji, Nagoya Institute of Technology

March 2018

ABSTRACT

TiO_2 nanoparticle assemblies as a promising material used in a wide area of applications have been synthesized by the previously reported one-pot single-step solvothermal reaction. Besides previously synthesized spherical nanoparticle assemblies named **mi**cro/**me**soporously **a**rchitected **r**oundly **i**ntegrated **me**tal **o**xide (MARIMO), the current study revealed a successfull synthesis of a novel TiO_2 nanoparticle assemblies with three-dimensionally branched nanostructure named "cheek-brush". Their growth mechanism and applications as a crosslinker to improve mechanical strength of a poly(*N*-isopropylacrylamide) hydrogel have been proposed. Dimethyl phthalate is a key material controlling the brush morphology in the solvothermal treatment of a titanium tetraisopropoxide in methanol. Standing of the precursor mixture (20 min), heating rate (5–6 °C/min), final reaction temperature (300 °C), and holding time at the final temperature (10 min) are crucial for the formation of cheek-brush morphology.

A surface activation was confirmed by facile treatment using helium atmospheric pressure plasma jet (APPJ) on TiO_2 MARIMOs, of which photocatalytic activities were significantly improved without any damage in morphology and surface properties by the treatment. A cylindrical dielectric barrier discharge system was used to treat the catalysts. After treatment under appropriate conditions depending on working distance and treatment time, SEM images and XRD patterns showed that the treated samples completely retained their original morphologies and crystalline patterns, respectively. Quantitative analyses of contaminants were executed using surface assisted laser desorption ionization (SALDI) mass spectroscopy technique, where the mass spectra of the assemblies revealed that almost all peaks observed in as-prepared samples were disappeared after the plasma treatments.

A surface modification by depositing nano-sized noble metal catalysts on TiO_2 was studied. The Au catalyst on different kinds of TiO_2 supports (MARIMO, ST-01, and P25) were prepared by a conventional deposition-precipitation method. TEM and HAADF-STEM images of the obtained Au/TiO_2 catalysts clearly indicate the excellent dispersion ability of Au nanoparticles on the unique surface roughness of MARIMO derived from their fine primary particles. Extremely exothermic CO oxidation was performed as a probe reaction using the prepared Au/TiO_2 as catalysts. CO conversions shows high activity of Au/MARIMO even at lower temperatures as compared to those of other kinds of support. Stabilities and durabilities of the catalysts were confirm by CO conversions from 10 cycle of high (140 °C) and low temperature (0°C) CO oxidations, alternatively.

ACKOWLEDGEMENTS

This dissertation could not have been completed without my academic advisor. Professor Dr. Kazuya KOBIRO, who encouraged and gave precious suggestions and discussion through my academic program. Not only chemistry, but life. I truly appreciate your time and effort. Thank you very much.

I would also be grateful to Professor Dr. Ryuichi SUGIMOTO, and Professor Dr. Nagatoshi NISHIWAKI as the co-supervisors, Professor Dr. Akimitsu HATTA, and Professor Dr. Masayoshi FUJI, as the members of thesis committee. Thank you very much for the valuable comments and suggestions on my researches.

In additions, I would like to express my sincere gratitude to Assistant Professor Dr. Masataka OHTANI for teaching me many experimental skills and for useful advices. Also, thank my colleagues, my lab members for their assistance and supports during my stay in Japan; both experimental work and daily life here.

Another group of people I would like to thank is my Thai friends here. Thank you for sharing memorable time during these three years. Also, thank you for your sympathetic ear and encouragement.

Most of all, I would like to express my deepest gratitude to my family who always pay attention to me all the times, I could not have a chance to do what I am doing without them. The most success of the graduation is devoted to my family.

CONTENTS

LIST OF TABLES

LIST OF FIGURES

CHAPTER I

General Introduction:

Motivation and Objective

Nanoparticles are defined as small particles with size ranging from 1 to 100 nm. Since all of the nanoparticles are surrounded by interfacial layer, they exhibit totally different physical and chemical properties as well as reactivities as compared to those of bulk materials. One of the attractive properties of nanoparticles is their large surface area (Figure 1-1), which is advantageous especially for catalysts and absorbents. On the other hand, several characteristics of nanoparticles would be both benefit and constraint. Most typical one is agglomeration of the nanoparticles, which commonly occurs due to their interaction between their interfacial layers. The agglomeration can be a benefit, if it is controllable, otherwise it would be shortcoming leading to deactivation of the surface of the nanoparticles.

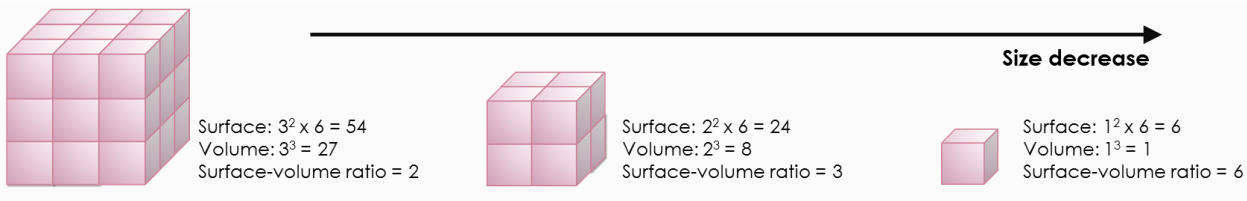

Figure 1-1. Schematic illustration of a relationship between surface area and size of material.

On the other hand, TiO_2 or titanium(IV) oxide is well known as one of the promising functional materials. It is a white solid inorganic material being used as a white pigment, an opacifier, and a UV resistant agent due to its attractive light-scattering and absorption properties depending on the range of light. Further studies on TiO_2 extended the use of it to wide range of applications due to its unique properties, such as transparency to visible light, high refractive index,

low light absorption coefficient, and capability of photocatalytic degradation of organic materials. A breakthrough moment of TiO_2 studies was when TiO_2 electrode was found to be an effective photocatalyst in water decomposition in 1972 by Fujishima et al.[1] The excellent property influences much attention on the synthesis of TiO_2 nanoparticles and tremendous amounts of basic researches as well as practical applications of TiO_2 have been done.

For TiO_2 nanoparticles, they exhibit quite different properties as compared to those of bulk one, for example significant low melting point, optical property change, quantum confinement effect, chemical activity increase, less probability for defects and residual stress, and conductivity change. Their characteristic properties can be adjusted by their particle sizes and structures derived from different preparation methods. Therefore, the preparation methods of TiO_2 nanoparticles have been focused in numerous researches.[5-12] The methods can be divided into two categories, one is bottom-up and the other is top-down approach. Physical or chemical approaches correspond to them, respectively, where milling, evaporation and quenching, sputtering deposition, and laser ablation are considered as examples for the former approaches, while chemical approaches correspond to the result of chemical reactions.

Focusing on chemical approaches to obtain TiO_2 nanoparticles, many methods such as common sol-gel processes, co-precipitation methods, conventional hydrothermal/solvothermal reactions, and chemical vapor deposition have been reported. Among these methods, sol-gel processes are most widely used as they are simple and suitable for large-scale production without complication. However, the method regularly requires calcination step under high temperature conditions to dehydrate the obtained gel of $Ti(OH)_4$. In the same way, the simplest method of co-precipitation usually requires multi-step reaction with long reaction time.

Relevant methods should be considered to produce nanoparticles with desired properties, since different preparation methods result in different morphologies and properties of TiO_2 nanoparticles. As previously mentioned, one of the constraints character of nanoparticles is the agglomeration. For an example, relatively large size particles are preferred in the application of TiO2 in photo-anode of dye-sensitized solar cells (DSCs), since the nanoparticles generally have weak light scattering property in the region of visible light wavelength. However, larger size particles suitable for better scattering have comparatively low surface area, which limits the dye-loading amount leading to low efficiency of DSCs. The controllable agglomerates or assemblies of nanoparticles show essential properties of primary particles such as their large surface area and uniformity. In the same time, the nanoparticle assemblies usually contain porous structures without aggregation, which results in a great stability, ease of handling, and an ability to have various chemical functionalities on the surface. Therefore, the preparation of uniform size of agglomerates is preferred to eliminate the disadvantages of the uncontrollable agglomeration. Accordingly, preparation of the uniform size of TiO_2 nanoparticle assemblies/agglomerates are obtained by several methods such as evaporation, polymer-assisted sol-gel, and solvothermal methods.[13-15]

Concerning on hydrothermal/solvothermal reactions, several approaches; mainly the use of a template/surfactant as shown in Figure 1-2, have been applied to control the morphology of TiO_2 products. For example, TiO_2 nanoparticle assemblies with hierarchical morphology were yielded by template/surfactant-assisted hydrothermal processes promoted the performance of solar cells with high efficiency.[16-21]

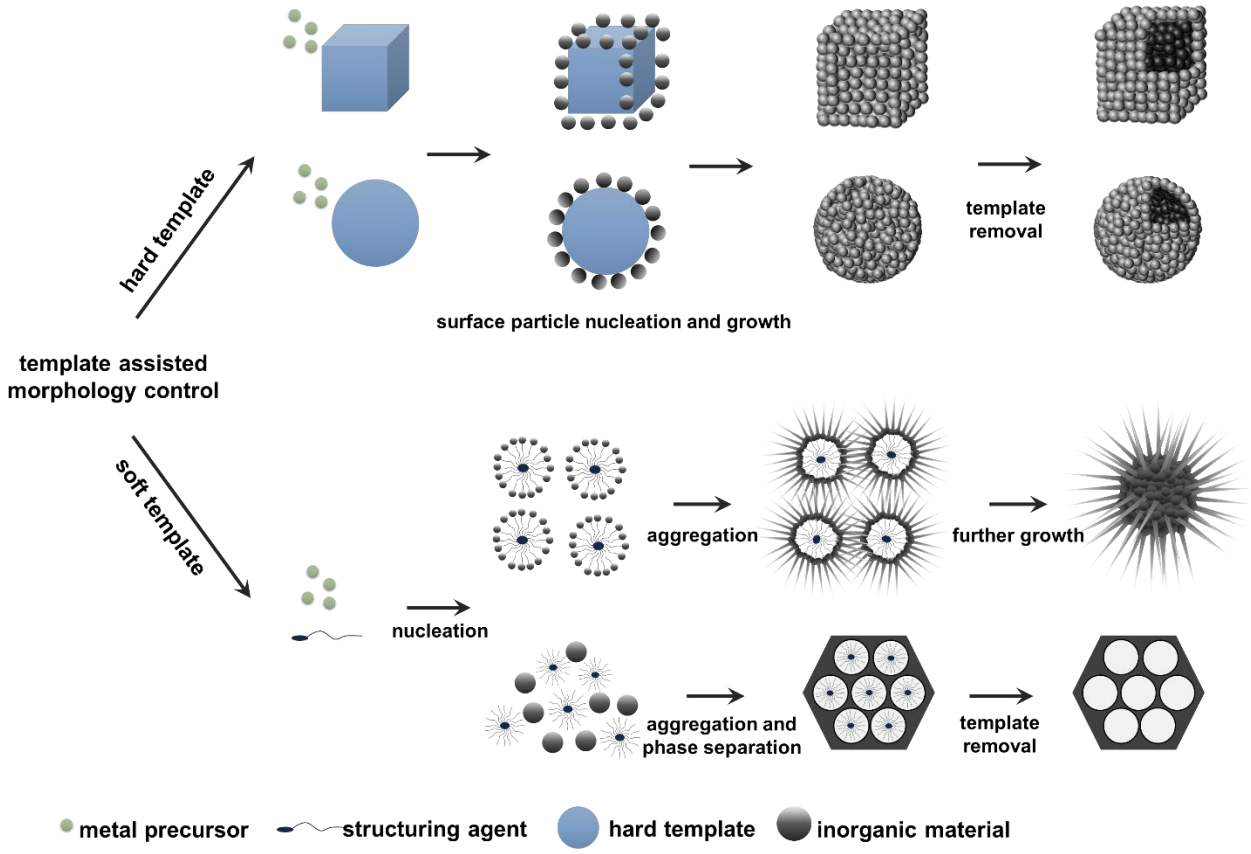

Figure 1-2. Scheme illustrated examples of controlled morphology of inorganic materials using template-assisted method.

For common solvothermal methods yielding metal oxide nanoparticles, precursor solutions containing metal sources, appropriate solvents, and additives such as organic acid and surfactants, are heated to high temperature and high pressure, where different nucleation and condensation mechanisms of metal oxide nanostructures were reported. As a result, tunable surface property and morphology can be achieved. However, longer reaction time reaching several days required in conventional solvothermal reactions are a crucial issue to be solved to synthesize nanoparticle assemblies.

Meanwhile, Wang P. et al. reported a successful one-pot single-step solvothermal reaction to prepare mesoporous nanoparticle assemblies of TiO_2 as shown in Figure 1-3.[22] The preparation method affording anatase TiO_2 nanoparticle assemblies is totally easy and the reaction was performed under usual solvothermal temperature of around 300 ºC. Also, a process scale-up can be achieved by using continuous reactors. The technique under adequate conditions can easily control the product morphology by adjusting reaction parameters such as precursor solutions, heating rates, and reaction temperatures. A crystallinity of the resulted TiO_2 can be controlled by heating rate to obtain amorphous and anatase TiO_2, respectively. Importantly, the TiO_2 assemblies are found as almost perfect spherical nanoparticle assemblies with fine primary particles of which the average size is less than 5 nm, and high surface area (>200 m2/g) with mesopores in their structures resulting in the unique surface structure and properties.

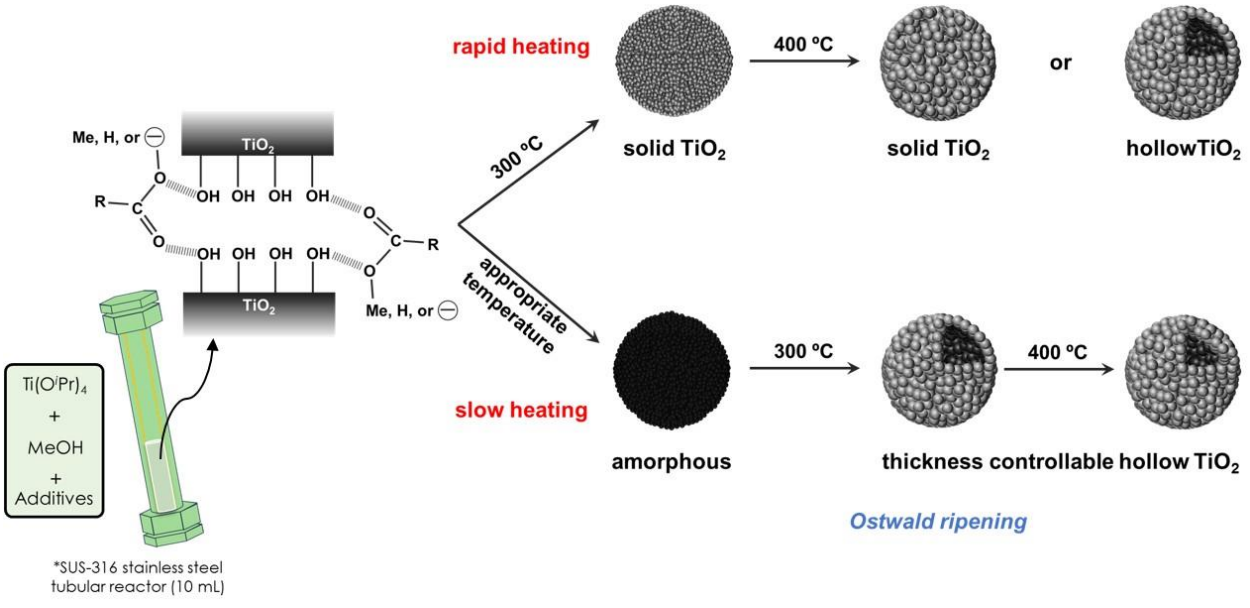

Figure 1-3. Solvothermal preparation of TiO_2 spherical nanoparticle assemblies: conditions and plausible mechanism.[10]

Since morphologies of materials can be defined by their surface structures. Both of the morphology and surface properties play main roles in designing material applications, especially for nano-scale materials, therefore, understanding and controlling of material surface and morphology are necessary. In addition, surface improvement of nanoparticle assembly can be further conducted as a post-treatment step, which the desired specific character can be achieved directly. Different kinds of post-treatments have been reported such as chemical treatment or high temperature treatment for contaminant removal, surface modification by functional group coating to improve hydrophobic property.[23-25]

Despite the fact that spherical nanoparticle assembly of TiO_2 with a mesoporous structure is one of the most promising functional materials, the creation of dimensionally controlled inorganic nanomaterial is one of the interesting challenges in the field of material science, since the controlled morphology can be further considered to design an application of each prepared nanomaterials. From nanocrystals to nanoparticle assemblies, several type of organic additives have been used to control the morphology of TiO_2 synthesized by solvothermal methods as reported in many publications. Sun W. et al. reported a coordination effect of acetic acid and *N*,*N*-dimethylformamide controlling size and shape in nanocrystal scale of anatase TiO_2 nanoplates.[26] The importance of hydrolysis and nucleation rate control was reported by Cheng H. et al, which showed the assistance of urea via Ostwald ripening in the preparation of TiO_2 core-shell spherical nanoparticle, instead of using only H_2O_2 to obtain microsphere TiO_2.[27] The current study revealed a successful synthesis of a novel type of TiO_2 nanoparticle assemblies with three-dimensionally branched nanostructure by the use of ester additives to control the morphology of product in the mentioned tunable solvothermal method.

A post treatment of as-prepared materials should be well considered to emerge their intrinsic performance of the materials. Then, a selection and adjustment of surface treatment technique and conditions could be also explored through a greater amount of applications of the TiO_2 nanoparticle assemblies. The objective of surface treatment can be as followed, to cover, to alter the surface, and to remove contaminants on the surface of the materials. For the surface contaminant removal of porous materials, several methods such as chemical treatment or wet cleaning, thermal treatment, ozone, and UV light treatment were employed based on the type of contaminants and the core materials.[28-31] The easiest and widely used thermal treatment usually causes sintering of the nanoparticles to reduce their surface areas, while ozone diffusion and UV light penetration could remove contaminants only from the surface of the porous materials. Therefore, non-thermal much effective methods are strongly desired.

Atmospheric pressure plasma jet (APPJ) technique is considered as an alternative choice for contaminants removal from nanoparticle surface as well as surface activation. Helium APPJ, generation, which requires non-severe conditions of high temperature and high vacuum with complex system, can be used in a wide range of applications. The optimization of the treatment conditions is crucial for the treatment of mesoporous nanostructure materials, where their structures are usually fragile and the pore structures can be easily collapsed. Moreover, the plasma contains positive ions and free electrons, which are reactive species capable of oxidizing contaminants that deactivate active sites of catalysts. Therefore, the synthesized spherical nanoparticle assemblies of TiO_2 can be expected to show their photocatalytic activity enhancement by this helium APPJ treatment without any deconstruction of their morphology.

Another interesting surface treatment of metal oxides is a surface modification by depositing nano-sized noble metal catalysts on their surface, particularly the use of metal oxides as catalyst supports. As mentioned earlier, TiO_2 has been widely used as a catalyst support due to its high physical and chemical stability. Specially, the spherical nanoparticle assemblies of TiO_2 possess fine primary particles of which the average size is less than 5 nm, and high surface area with mesopores in their structures. The assemblies have unique surface roughness originated from their fine primary particles resulting in plausibly high surface defects, which are expected to disperse metal nanoparticle well. Among a numerous amount of researches mentioned, one of the most serious deactivation factors of catalysts is sintering. A major cause of the sintering is a nanoparticle migration, which is commonly occurred at high temperature due to an increase of the catalyst mobility, leading to the growth into large particles and the decrease of active sites on the catalysts. To prevent the sintering, confinement of catalyst nanoparticles by support materials is considered as one of the strategies. On the other hand, good-dispersion and strong interaction of metal catalyst on the support are crucial factors to prevent the sintering. From these strategies, the support has been focused as one of the important factor as reported in several researches to design a stable catalyst. Here, a hypothesis of using nanoparticle assemblies TiO_2 with nanoscale concave-convex surface structure as an effective and stable catalyst support to prevent the thermal catalyst sintering is proposed.

From this angle, the overall goal of these researches is to synthesize the morphology controllable of highly active TiO_2 nanoparticle assemblies using the simple one-pot single-step solvothermal reaction.

Scope

This study manifests the synthesis and application of the morphology controlled of TiO_2 nanoparticle assemblies with totally unique three-dimensionally branched nanostructure, affording the enhancement of mechanical strength on nanocomposite polymer hydrogel, demonstrated by adjusting the solvothermal reaction conditions in the preparation of spherical morphology of TiO_2 nanoparticle assemblies. Also, surface treatments of the solvothermally prepared TiO_2 spherical nanoparticle assemblies were studied. A facile treatment without damage on morphology and surface properties of TiO_2 by atmospheric pressure plasma treatment was studied to enhance the ability of the synthesized TiO_2 as a highly active photocatalyst since TiO_2 is well known for its photocatalytic activity. Besides, a surface modification by Au metal catalyst deposition on the prepared TiO_2 spherical nanoparticle assembly was studied to understand the advantage of the TiO_2 spherical nanoparticle assemblies with unique surface comparing to other common TiO_2 supports. Their catalytic activity was studied through CO oxidation reaction as a probe reaction. Furthermore, the TiO_2 support stability was also investigated.

Dissertation outline

This dissertation is divided into five chapters. The first chapter describes a general introduction of the research containing motivation and objective, scope, and dissertation outline. Chapter II explains a synthesis of TiO_2 with novel morphology and its polymer nanocomposite application focusing on the assemblies' unique three-dimensionally branched nanostructure. Chapter III discusses surface treatment of TiO_2 spherical nanoparticle assemblies by APPJ and their photocatalytic activity enhancement. Chapter IV describes the use of TiO_2 spherical

nanoparticle assemblies as effective supports for Au nanoparticle catalyst in a probe reaction of CO oxidation, followed by Chapter V; the last chapter, which concludes the results and gives some recommendations for future works.

References

[1] Fujishima A. and Honda K. Electrochemical photolysis of water at a semiconductor electrode, *Nature* **1972**, 238, 37-38.

[2] Low J., Cheng B., and Yu J. Surface modification and enhanced photocatalytic CO_2 reduction performance of TiO_2: a review, *Appl. Surf. Sci.* **2017**, 392, 658-686.

[3] Liu P., Qin R., Fu G., and Zheng N. Surface coordination chemistry of metal nanomaterials, *J. Am. Chem. Soc.* **2017**, 139, 2122-2131.

[4] Biesinger M. C., Payne B. P., Grosvenor A. P., Lau L. W. M., Gerson A. P., and Smart R. St. C. Resolving surface chemical states in XPS analysis of first row transition metals, oxides and hydroxides: Cr, Mn, Fe, Co and Ni, *Appl. Surf. Sci.* **2011**, 257, 2717-2730.

[5] Sato K., Yamamoto Y., Fujishiro Y., and Uchida S. Intercalation of iron oxide in layered $H_2Ti_4O_9$ and $H_4Nb_6O_{17}$: visible-light induced photocatalytic properties, *J. Chem. Soc.Faraday Trans.* **1996**, 92, 5089-5092.

[6] Uchida S., Yamamoto Y., Fujishiro Y., Watanabe A., Ito O., and Sato T. Intercalation of titanium oxide in layered $H_2Ti_4O_9$ and $H_4Nb_6O_{17}$ and photocatalytic water cleavage with

$H_2Ti_4O_9$/(TiO_2, Pt) and $H_4Nb_6O_{17}$/(TiO_2, Pt) nanocomposites, *J. Chem. Soc. Faraday Trans.***1997**, 93, 3229-3234.

[7] Xu N., Shi Z., Fan Y., Dong J., Shi J, and M. Z. C. Hu. Effects of Particle Size of TiO_2 on Photocatalytic Degradation of Methylene Blue in Aqueous Suspensions, *Ind. Eng. Chem. Res.* **1999**, 38, 373-379.

[8] Reijnders L. Hazard reduction for the application of titania nanoparticles in environmental technology, *J. Hazard. Mater.* **2008**, 152, 440-445.

[9] Kwon, Shin H., Kim, Choi, and Yoon. Degradation of methylene blue via photocatalysis of titanium dioxide, *Mater. Chem. Phys.* **2004**, 86, 78-82.

[10] Farrokhpay S., Morris G., Fornasiero D., and Self P. Titania pigment particles dispersion in water-based paint films, *J. Coat. Technol. Res.* **2006**, 3, 275-283.

[11] Inoue S., Kodou H., Muto A., and Ono T. Novel preparation of titania (TiO_2) catalyst support by applying the multi-gelation method for ultra-deep HDS of diesel oil, *Fuel Chem. Div. Prepr.* **2003**, 48, 88-89.

[12] Xiao Y., Wu J, Yue G., Xie G., Lin J., and Huang M. The preparation of titania nanotubes and its application in flexible dye-sensitized solar cells, *Electrochim. Acta* **2010**, 55, 4573-4578.

[13] Park Y.-C., Chang Y.-J., Kum B.-G., Kong E.-H., Son J. Y., Kwon Y. S., Park T., and Jang H. M. Size-tunable mesoporous spherical TiO_2 as a scattering overlayer in high-performance dye-sensitized solar cells, *J. Mater. Chem.* **2011**, 21, 9582-9586

[14] Sun W., Chen M., Zhou S., and Wu L. Synthesis of hierarchically nanostructureed TiO_2 spheres with tunable morphologies based on a novel ampliphilic polymer precursor and their use for heavy metal ion sequestration, *J. Mater. Chem. A* **2014**, 2, 14004-14013.

[15] Liu X., Duan W., Chen Y., Jiao S., Zhao Y., Kang Y., Li L., Fang Z., Xu W., and Pang G. Porous TiO_2 assembled from monodispersed nanoparticles, *Nanoscale Res. Lett.* **2016**, 11, 159-166

[16] Cabral K. P., Kurniawan W., and Hinode H. Three-dimensional sea urchin-like TiO_2 synthesized via facile hydrothermal method: Its properties and solar photocatalytic activity, *J. Environ. Chem. Eng.* **2015**, 3, 2786-2796.

[17] Zhao W., Wang H., Feng X., Zhang Y., and Zhang S. Control over morphology of TiO_2 hierarchically structured microspheres in solvothermal synthesis, *Mater. Lett.* **2015**, 158, 174-177.

[18] Lekphet W., Ke T.-C., Su C., Kathirvel S., Sireesha P., Akula S. B., and Li W.-R. Morphology control studies of TiO_2 microstructurees *via* surfactant-assisted hydrothermal process for dye-synsitized solar cell applications, *Appl. Surf. Sci.* **2016**, 382, 15-26.

[19] Yan L., He X., Wang Y., Li J., and Wang D. Template-free solvothermal synthesis and photocatalytic properties of TiO_2 hollow spheres, *J. Mater. Sci: Mater Electron* **2016**, 27, 4068-4073.

[20] Sun X., Xu S., Gao Y., Yue M., Yue Q., and Gao B. 3D hierachical golden wattle-like TiO_2 microspheres: polar acetone-based solvothermal synthesis and enhanced water purification performance, *CrystEngComm* **2017**, 19, 2187-2194.

[21] Li Z.-Q., Mo L.-E., Chen W.-C., Shi X.-Q., Wang N., Hu L.-H., Hayat T., Alsaedi A., and Dai S.-Y. Solvothermal Synthesis of Hierarchical TiO_2 Microstructures with high crystallinity and superior light scattering for high-performance dye-sensitized solar cells, *ACS Appl. Mater. Interfaces* **2017**, 9, 32026-32033.

[22] Wang P., Ueno K., Takigawa H., and Kobiro K. Versatility of one-pot, single-step synthetic approach for spherical porous (metal) oxide nanoparticles using supercritical alcohols, *J. Supercrit. Fluids* **2013**, 78, 124-131.

[23] Colon G., Sanchez-Espana J. M., Hidalgo M. C., and Navio J. A. Effect of TiO_2 acidic pretreatment on the photocatalytic properties for phenol degradation, *J. Photochem. Photobiol. A* **2006**, 179, 20-27.

[24] M. Fadoni, L. Lucarelli, in *Surface Science and Catalysis*, Vol. 120, ed. A. Dabrowski, Elsevier Science B.V., Amsterdam, Netherlands, 1999, pp. 177-225.

[25] Sharifi N., Pugh M., Moreau C., and Dolatabadi A. Developing hydrophobic and superhydrophobic TiO_2 coatins by plasma spraying, *Surf. Coat. Technol.* **2016**, 289, 29-36.

[26] Sun W., Liu H., Hu J., and Li J. Controllable synthesis and morphology-dependent photocatalytic performance of anatase TiO_2 nanoplates, *RSC Adv.* **2015**, 5, 513-520.

[27] Cheng H., Chen G., Zhang W., Qiu M., Yang Z., Zhu X., Ma G., and Fu Y. A novel hydrolytic reaction to morphology-controlled TiO_2 micro/nanostructures for enhanced photocatalytic performances, *RSC Adv.* **2015**, 5, 43630-43638.

[28] Colon G., Sanchez-Espana J. M., Hidalgo M. C., and Navio J. A. Cu-doped TiO_2 systems with improved photocatalytic activity, *J. Photochem. Photobiol. A* **2006**, 179, 20-27.

[29] Fadoni M., and Lucarelli L., in *Surface Science and Catalysis*, Vol. 120, ed. A. Dabrowski, Elsevier Science B.V., Amsterdam, Netherlands, 1999, pp. 177-225.

[30] Vig J. R., and Bus J. W. UV/ozone cleaning of surfaces, *IEEE Trans. Parts, Hybrids, Packag.* **1976**, 4, 365-370.

[31] Hook A. A., Ohlhausen J. A., Krim J., and Dugger M. T. Evaluation of oxygen plasma and UV ozone methods for cleaning of occluded areas in MEMS device, *J. Microelectromech. Syst.* **2010**, 19, 1292-1298.

CHAPTER II

A Novel Three-dimensionally Branched TiO_2 with Cheek-brush Morphology and its Application in an Improvement of Hydrogel Polymer Strength

2.1 Introduction

Dimensionally controlled inorganic nanomaterials have been paid much attention in material science for both of their synthesis and application. In particular, a nanoscale branched structure providing high surface area improves surface adsorption and adhesion, which facilitates strong interaction to molecules, polymers, biomaterials, and so on. For example, such inorganic materials have significant attention as a crosslinker to create mechanically stable polymer hydrogels. They are key materials to improve physical and mechanical strength of polymers, since they connect polymer chains each other to enhance the mechanical stability of polymer network.[1-7] Role of the crosslinkers is considerably essential in the field of polymer hydrogels. Typically, these polymer hydrogels consist of a polymer networks and a large amount of water, where water is weakly fixed into polymer networks. In this context, many types of crosslinkers, both organic and inorganic, have been developed.[8-10] One of the most interesting crosslinkers used in polymer hydrogels is clay nanosheets, because their wide flat surface structures enable strong interactions between the clay nanosheet surface and polymer chains at their interface.[11–17] Clay nanosheets can also be used to construct house-of-cards structures consisting of clay platelets by ionic interactions between their faces and edges, as reported for the preparation of a nanocomposite hydrogel composed of poly(*N*-isopropyl-acrylamide) and clay.[18,19] One-dimensional

nanomaterials such as nanorods, nanofibers, and nanotubes have also been studied for the preparation of attapulgite/poly(acrylic acid), carbon nanotube fillers in gellan gum hydrogels, and ultra-high-molecular weight polyethylene fibers in poly(vinyl alcohol).[20-22]

Among many kinds of crosslinkers, TiO_2 nanoparticles also have been used in many polymer nanocomposites including polymer hydrogels.[23-30] However, Haraguchi et al. used TiO_2 nanoparticles as a filler in the preparation of polyacrylamide/poly(*N*-isopropylacrylamide) copolymer hydrogels, then they found that the spherical nanosized TiO_2 did not act as a crosslinker, instead dispersed uniformly.[18] Recently, Ishida and Aida et al. introduced a new concept in hydrogel chemistry by using two-dimensional TiO_2 nanosheets.[31-33] Thus, the hydrogel performance is significantly affected by surface nanostructure of crosslinkers. In other words, polymer composite hydrogels can be used as a new tool to evaluate surface properties of the higher-ordered TiO_2 nanoparticle assemblies though their mechanical strength.

Previously, the successful synthesis of porous spherical TiO_2 nanoparticle assemblies with large surface areas using an original, simple, one-pot, single-step, and template-free preparation method was reported, involving heating a homogeneous precursor methanol solution of titanium tetraisopropoxide, as a titanium source, and phthalic acid, as an additive, to 300 °C (Figure 2-1).[34] Solid and hollow structure can be easily controlled by tuning reaction conditions such as heating rate. This type of porous spherical metal oxide was named as a MARIMO nanoparticle assembly; the acronym is derived from **m**icro/**m**esoporously **a**rchitected **r**oundly **i**ntegrated **m**etal **o**xide (Figure 2-2a). Because of the high reaction temperature, *dimethyl phthalate* could be generated in the reaction mixture (Figure 2-1), and that the generated ester could be a key material in the formation of MARIMO morphologies. Therefore, the additive in the precursor solution was changed from phthalic acid to dimethyl phthalate to clarify the effect of the ester.

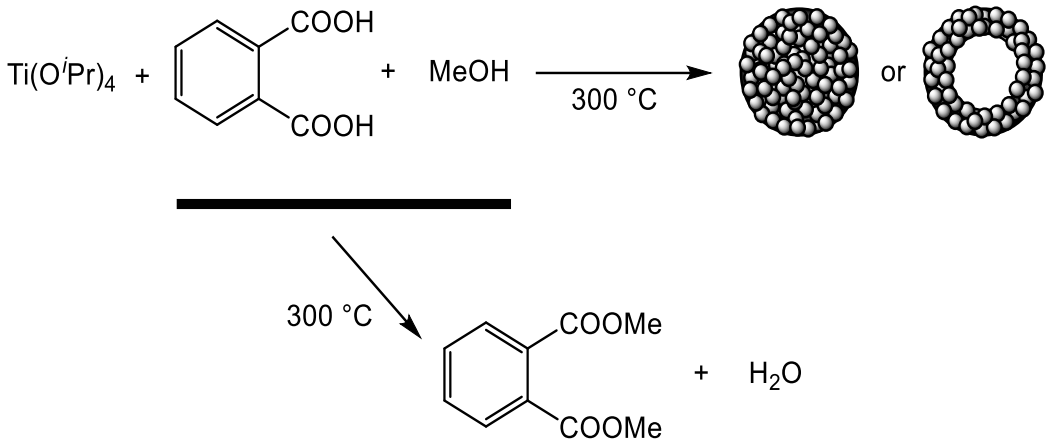

Figure 2-1. Solvothermal synthesis of TiO_2 spherical nanoparticle assemblies.

Then, similar solvothermal treatment of a mixture of titanium tetraisopropoxide and dimethyl phthalate in methanol serendipitously gave a completely different morphology, affording high-order structure of TiO_2 assemblies with nanofiber bundles morphology (Figure 2-2b). The particle assemblies were named "cheek-brush" nanofiber bundles because their morphologies resemble makeup brushes.

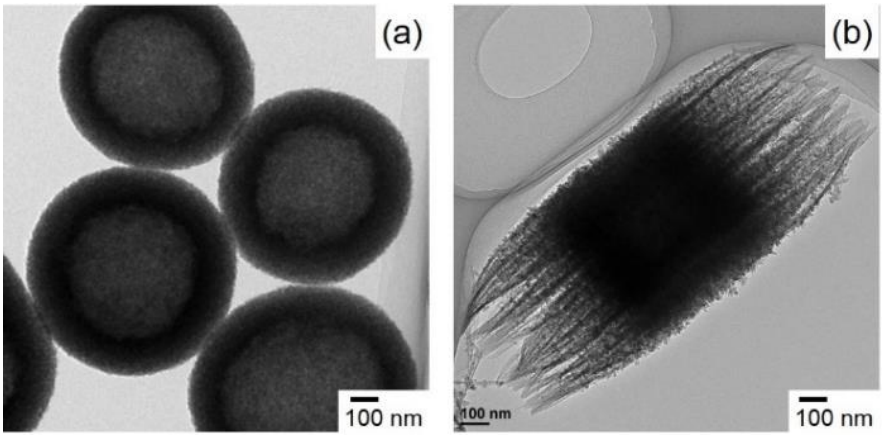

Figure 2-2. TEM images of TiO_2 with MARIMO assemblies (a) and cheek-brush assemblies (b).

In this chapter, an exhaustive study on the reaction conditions to yield the cheek-brush morphology of TiO_2 nanofiber bundles and an evaluation of the unique surface nanostructure through mechanical tensile strength of polymer hydrogels are discussed.

2.2 Experiment

2.2.1 Materials

Methanol, ethyl acetate, titanium tetraisopropoxide, titanium tetra-*n*-butoxide, dimethyl phthalate, diethyl phthalate, di-*n*-butyl phthalate, di-*n*-octyl phthalate, methyl benzoate, *N*-isopropylacrylamide, *N*,*N*,*N'*,*N'*-tetramethylethylenediamine, and potassium peroxodisulfate were purchased from the Wako Pure Chemical Industries Co., Ltd. and were used as received. Reverse osmosis water was used throughout the experiments.

2.2.2 Preparation of cheek-brush assemblies of TiO_2

Cheek-brush nanofiber assemblies of TiO_2 were prepared using a previously reported method.[34] Precursor solutions containing 0.5 mol/L organic additives were prepared by mixing an aliquot of the additive with methanol (3.5 mL) using a Vortex mixer, followed by addition of titanium tetraisopropoxide (105 µL, 0.353 mmol). The precursor solution was transferred to an SUS-316 stainless-steel tubular reactor of inner volume 10 mL. The reactor was sealed with a screw cap and left to stand at room temperature for 20 min. It was heated at a rate of 5.4 °C/min to 300 °C; the temperature was maintained for 10 min. The reaction was quenched by putting the

reactor in an ice-water bucket. The obtained mixture was centrifuged and washed with methanol; the procedure was repeated three times. The final suspended mixture was completely dried under vacuum and a powdery product was obtained.

2.2.3 Nanoparticle assembly characterizations

The morphologies of the obtained particles were observed using scanning electron microscopy (SEM; JEOL JSM-7300F) and transmission electron microscopy (TEM; JEOL JEM-2100F). The product particle sizes were calculated from the images. The crystalline phase was identified using X-ray diffraction (XRD; Cu Kα radiation, Rigaku SmartLab). Mass spectra of the precursor solutions were obtained using electrospray ionization mass spectrometry (ESI-MS; AB Sciex Triple TOF 4600).

2.2.4 Preparation of hydrogels and mechanical strength measurements

Hydrogels were prepared using a modified version of a previously reported method for the synthesis of hydrogels consisting of poly(*N*-isopropylacrylamide) and clay.[12] The crosslinker nanoparticles were dispersed in water with N_2 bubbling (0.02wt%), and then *N*-isopropylacrylamide was added to the solution (20wt%). The mixture was stirred for 30 min and then potassium persulfate and *N*,*N*,*N*′,*N*′-tetramethylethylenediamine were added. The mixture was carefully transferred to glass tubes of inner diameter 1.0 cm. The upper dead volume in the tubes was purged with N_2 and the tubes were closed tightly with screw caps. After 72 h, the glass tube was cut and the polymer hydrogel was removed. Hydrogel rods of diameter 1.0 cm and length 3.0 cm were used for mechanical strength measurements. A tensile force was applied to the specimens

in the axial direction, and the deformation length of the hydrogel and the applied force were measured using a tensile tester (Shimadzu EZ Test).

2.3 Result and Discussion

2.3.1 Synthesis of cheek-brush assemblies of TiO_2

The procedure for the synthesis of cheek-brush TiO_2 assemblies was simple. A precursor mixture of titanium tetraisopropoxide, dimethyl phthalate, and methanol was heated to 300 °C under solvothermal conditions. However, when the reactions were repeated, sometimes a perfect cheek-brush morphology was achieved, but sometimes not, even under similar conditions. The reproducibility of the cheek-brush morphology formation was therefore erratic. Each procedure was checked thoroughly, including preparation of the precursor mixture, heating process, concentration of the materials, and molar ratios of the reagents, individually.

2.3.1.1 Effect of standing period of precursor mixture

Standing period means a step that the precursor was kept stand for a while after titanium source was added (Figure 2-3a). When the mixture was left to stand for 20 min at room temperature before heating (heating rate, 5.4 °C/min; final temperature, 300°C; and holding time at final temperature, 10 min), TiO_2 assemblies with a perfect cheek-brush morphology were obtained (Figure 2-3b, i). However, without standing before heating, urchin-shaped assemblies with short needles were obtained (Figure 2-3b, ii). Mechanical stirring or mixing of the precursor mixture instead of standing gave urchin-shaped rather than cheek-brush assemblies, suggesting that there

might be weak interactions between the components. These results indicate that the formation of higher-ordered assemblies connected through weak interactions could be a key factor in obtaining TiO_2 assemblies with a cheek-brush morphology.

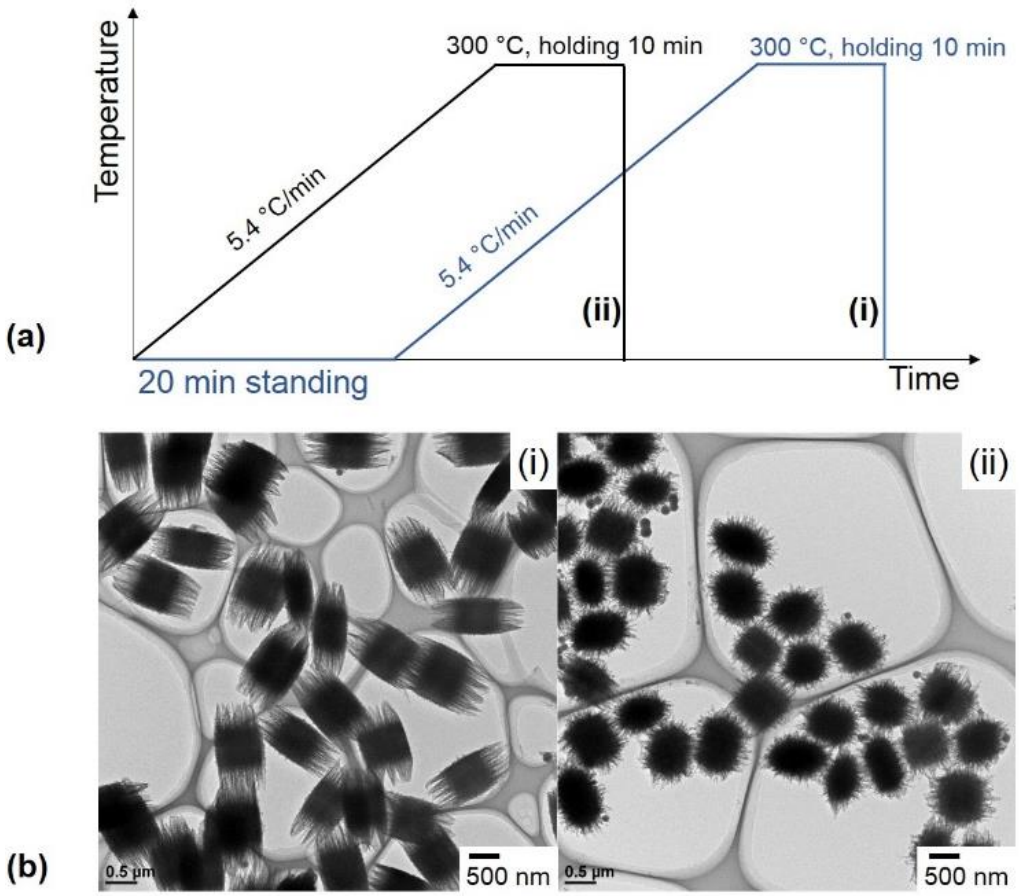

Figure 2-3. (a) Schematic illustration of experimental path after the preparation of precursor mixture and (b) TEM images of TiO_2 assemblies obtained from precursor solution consisting of 0.1 mol/L titanium tetraisopropoxide and 0.5 mol/L dimethyl phthalate in methanol with (i) 20 min standing period and (ii) without standing period at room temperature before heating.

The precursor mixture was studied using ESI-MS to clarify what happens during standing (Figure 2-4 and 2-5). When titanium tetraisopropoxide and dimethyl benzoate were mixed in

methanol, several peaks were observed in the 1000 (*m*/*z*) region using ESI-MS in positive-ion mode. The peak at 989 mass units can be ascribed to a cluster peak consisting of five titanium tetramethoxide molecules, four methanol molecules, and one proton. The peak at 1021 mass units can be ascribed to a cluster peak consisting of five titanium tetramethoxide molecules, five methanol molecules, and one proton. The formation of titanium tetramethoxide in the precursor mixture is reasonable, because slow transesterification between titanium tetraisopropoxide and methanol can occur to yield the corresponding titanium tetramethoxide with less-bulky methyl groups.[35]

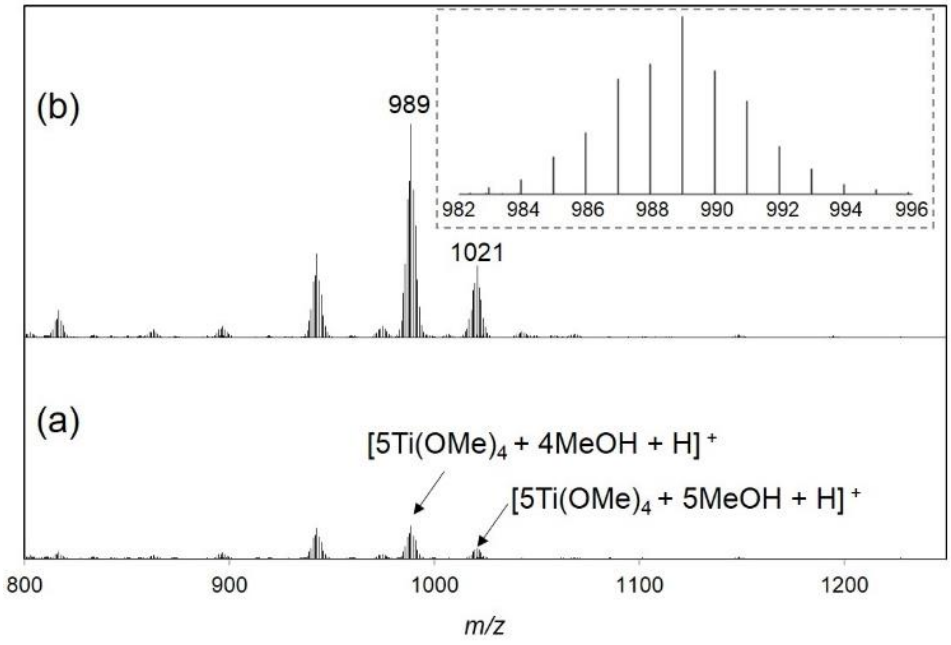

Figure 2-4. ESI-MS spectra obtained from precursor solution consisting of 0.1 mol/L titanium tetraisopropoxide and 0.5 mol/L dimethyl phthalate in methanol with (a) 20 min standing period and (b) without standing period at room temperature before heating.

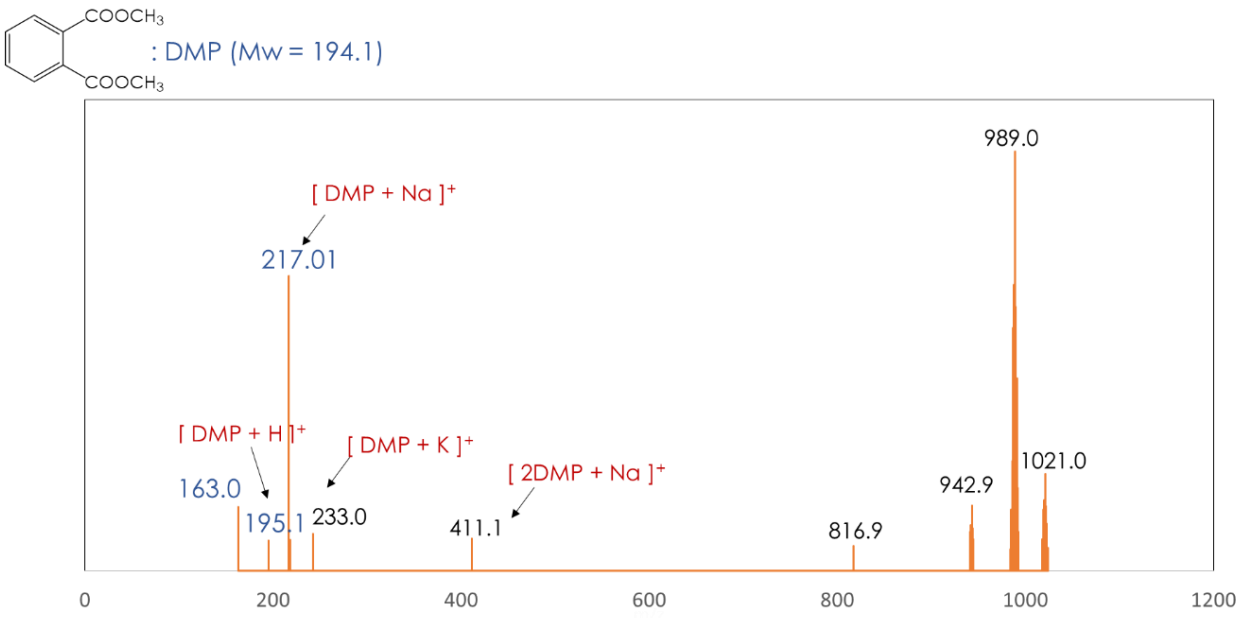

Figure 2-5. ESI mass spectra of precursor solutions prepared from 0.1 mol/L of titanium tetraisopropoxide and 0.5 mol/L of dimethyl phthalate in 3.5 mL of methanol with standing period 20 min.

Moreover, in the previously reported procedure for the preparation of MARIMO TiO_2, a precursor mixture consisting of titanium tetraisopropoxide, phthalic acid, and methanol gave a transparent solution, as shown in Figure 2-6a.[34] However, the use of dimethyl phthalate instead of phthalic acid resulted in a white turbid dispersion, as shown in Figure 2-6b. The white dispersion was not dissolved in methanol, and could be a high-molecular weight associate generated in the mixture. After several minutes, the turbidity increased in accordance with the formation of titanium tetramethoxide. Additionally, other kinds of ester were also studied as additives and the ESI-MS results of the precursor solutions using different types additives are shown in Figure 2-7 confirming the possibility of the complex formation.

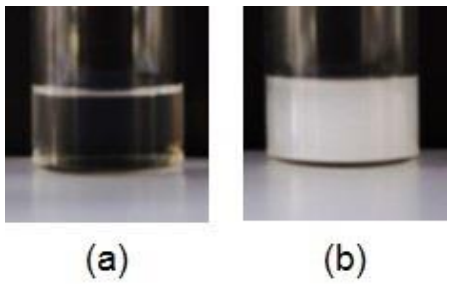

Figure 2-6. Photographs of precursor solutions containing titanium tetraisopropoxide, methanol, and (a) phthalic acid and (b) dimethyl phthalate.

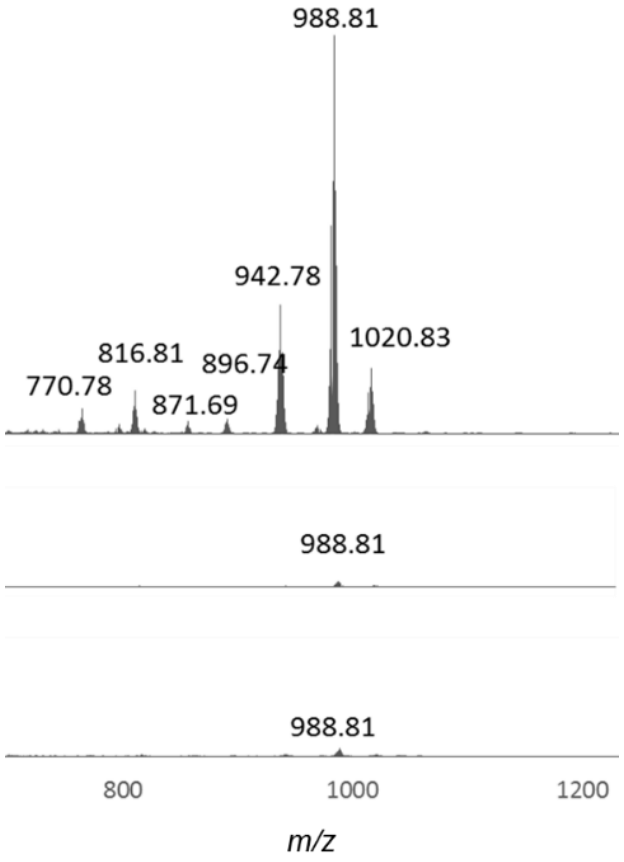

Figure 2-7. ESI mass spectra of precursor solutions prepared from 0.1 mol/L of titanium tetraisopropoxide and 0.5 mol/L of methyl benzoate (a), di-*n*-butyl phthalate (b), and di-*n*-octyl phthalate in 3.5 mL of methanol with standing period 20 min.

2.3.1.2 Effect of dimethyl phthalate concentration

The importance of dimethyl phthalate in the formation of a cheek-brush morphology was confirmed by varying the dimethyl phthalate concentration in the range from 0.25 to 1.0 mol/L (Figure 2-8). The other reaction conditions, i.e., concentration of titanium tetraisopropoxide, heating rate, final temperature, and holding time at final temperature, were fixed at 0.1 mol/L, 5.4 °C/min, 300 °C, and 10 min, respectively. Assemblies of similar size, i.e., fiber length 1300 nm (calculation shown in Appendix A), with perfect brush needles were obtained with the use of the precursor solution containing 0.5 and 0.75 mol/L dimethyl phthalate (Figure 2-8b, c). A low concentration solution, 0.25 mol/L, also yielded a cheek-brush morphology, but the brushes were not well formed and most of the assemblies were aggregated (Figure 2-8a). In the case of a high concentration, 1.0 mol/L, the assembly morphology became urchin-like. Too low and too high concentrations of the additive, therefore did not give perfect brush morphologies. These results suggest that the appropriate pre-organized structures for the asymmetrical growth of cheek-brush might be formed in the precursor solution with certain concentration of dimethyl phthalate.

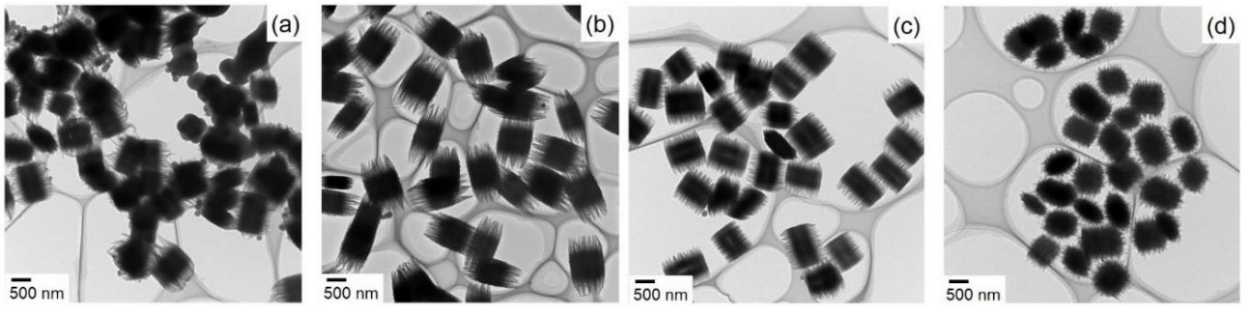

Figure 2-8. TEM images of TiO_2 assemblies obtained from precursor solutions with different concentrations of dimethyl phthalate: (a) 0.25 mol/L, (b) 0.5 mol/L, (c) 0.75 mol/L, and (d) 1.0 mol/L.

2.3.1.3 Effect of heating conditions

The effects of the heating conditions, i.e., heating rate, final temperature, and holding time at the final temperature, were also examined. Figure 2-9a–c show TEM images of the products obtained under different heating conditions. First, final temperature of 250, 275, and 300 °C were set. The other reaction conditions, i.e., concentrations of titanium tetraisopropoxide and dimethyl phthalate, heating rate, and holding time at the final temperature, were fixed at 0.1 mol/L, 0.5 mol/L, 5.4 °C/min, and 10 min, respectively. When the desired temperature was reached, the reaction was quenched by putting the reactor in an ice-water bucket to give a holding time at the final temperature of 0 min.

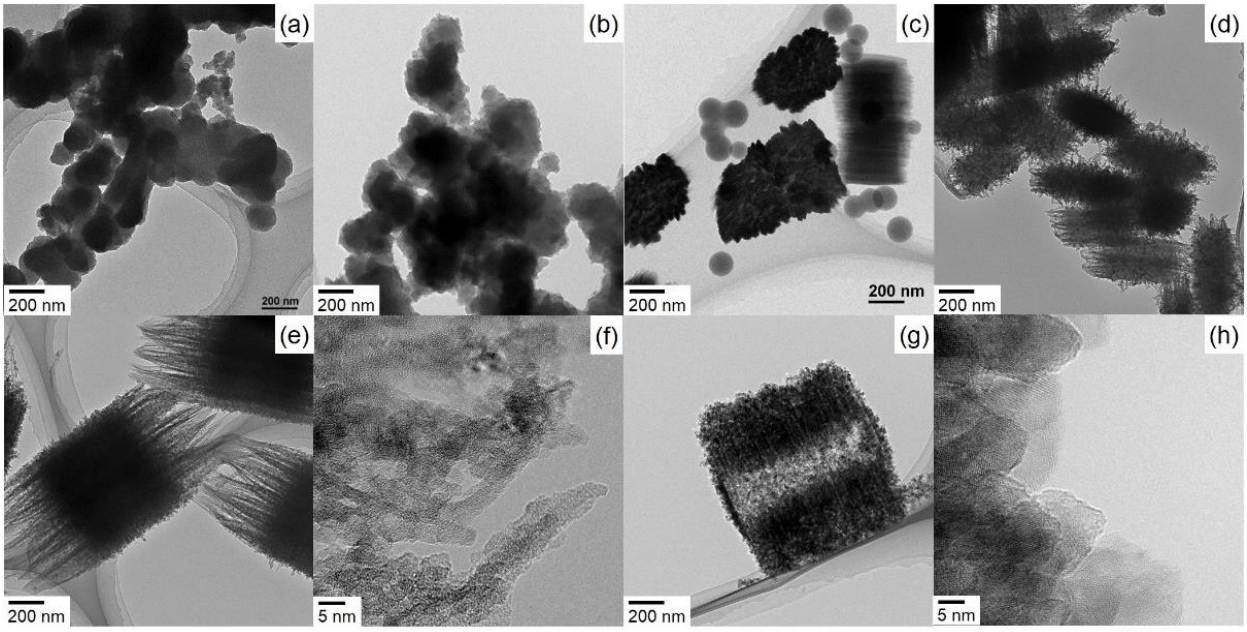

Figure 2-9. TEM images of TiO_2 assemblies heated at 5.4 °C/min (a) up to 250 °C and 0 min holding, (b) up to 275 °C and 0 min holding, (c) up to 300 °C and 0 min holding, (d) up to 300 °C and 5 min holding, (e) and (f) up to 300 °C and 10 min holding, (g) and (h) up to 300 °C and 60 min holding

Figure 2-9a–c show that the assembly morphology changed from randomly aggregated irregularly shaped particles to bundles of short fibers during heating, indicating that a high temperature such as 300 °C is necessary for formation of a brush morphology. The holding time at a final temperature of 300 °C is also an important factor (Figure 2-9d–h). The needles grew gradually at the holding time until 10 min, but further heating at 300 °C resulted in shrinkage of the brush needles and formation of tubular hollow structures.

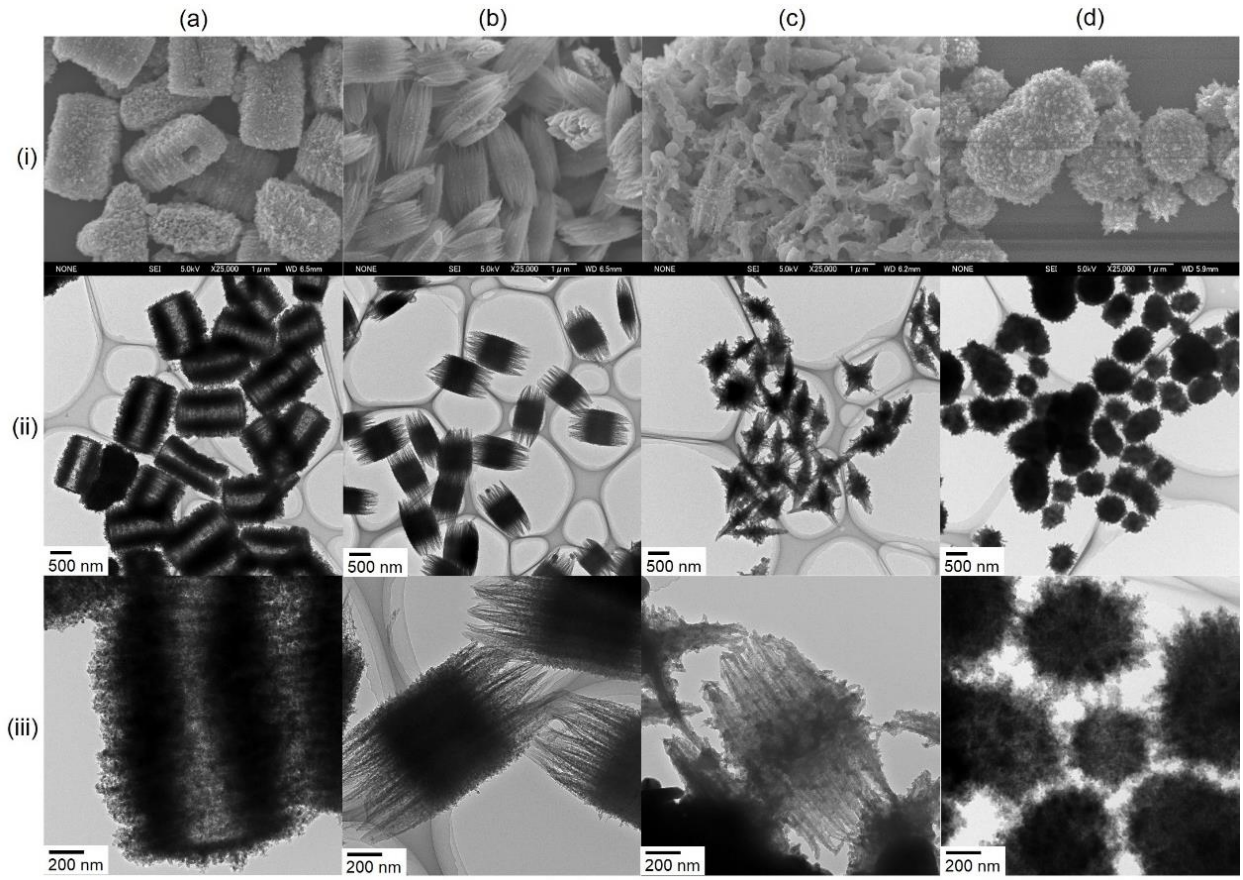

Figure 2-10. SEM and TEM images of TiO_2 assemblies obtained using different heating rates: (a) 2 °C/min, (b) 5.4 °C/min, (c) 10 °C/min, and (d) 500 °C/min ((i), SEM; (ii), TEM at low magnification; (iii), TEM at high magnification.

Secondly, the effect of the heating rate on brush morphology formation was examined (Figure 2-10). The concentrations of titanium tetraisopropoxide and dimethyl phthalate were fixed at 0.1 and 0.5 mol/L, respectively. The final temperature and holding time were fixed at 300 °C and 10 min, respectively. Figure 2-10a shows that slow heating, at 2 °C/min, resulted in formation of tube-shaped assemblies with short needles. The tube length was ca. 2 μm and the width was ca. 900 nm. Faster heating, i.e., at 10 and 500 °C/min, led to broken cheek-brush or urchin-like morphologies with shorter needles (Figure 2-10c, d). A heating rate of 5.4 °C/min gave the ideal cheek-brush morphology (Figure 2-10b).

The high-resolution TEM images in Figures 2-9f and 2-11 confirm that the brushes consist of small single crystals of TiO_2. The crystal structures of the assemblies obtained using different heating rates were also investigated using XRD (Figure 2-12). All the assemblies consisted of anatase phase TiO_2, but the broad diffraction peaks indicate that a fine and/or almost amorphous anatase phase was obtained in the case of relatively rapid heating, i.e., at 10 °C/min. A series of experimental results about heating conditions indicates that the growth of brush fiber transiently occurred at the certain time period during the heating process. Moreover, the excessive heating of cheek-brush leads to further crystallization with shrinking of the fiber structures.

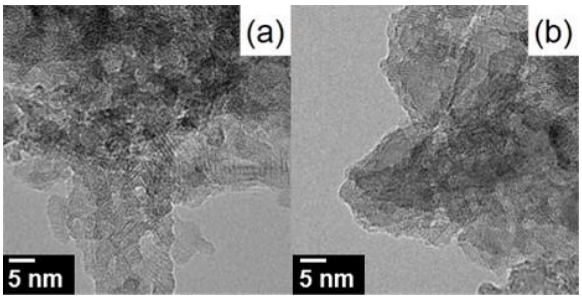

Figure 2-11. HR-TEM of TiO_2 prepared from 300 °C, 10 min holding at final temperature with heating rate of 5.4 °C/min (a) and 2 °C/min (b).

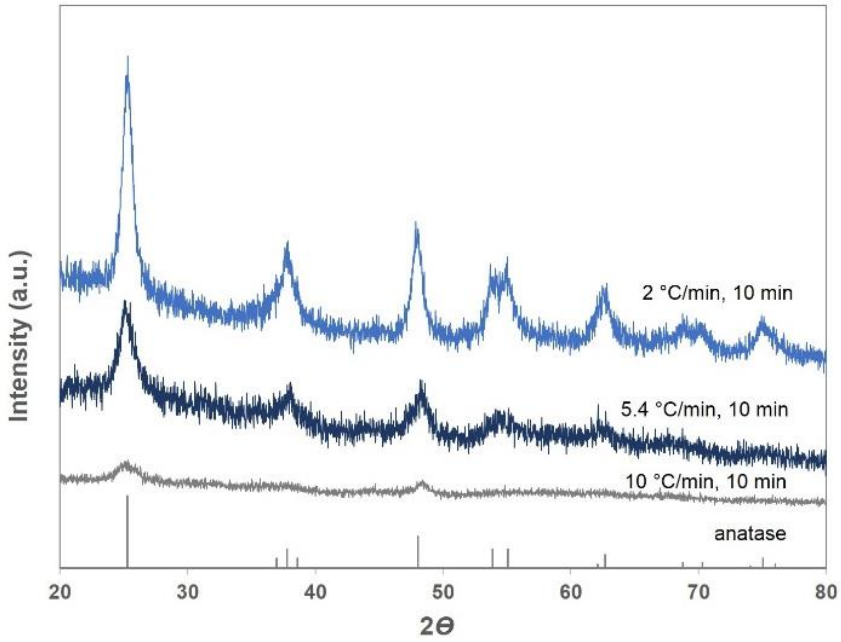

Figure 2-12. XRD patterns of TiO_2 assemblies obtained at heating rates of 2 °C/min, 5.4 °C/min, and 10 °C/min.

2.3.1.4 Effect of aromatic ester additive

Other esters, i.e., methyl benzoate, diethyl phthalate, di-*n*-butyl phthalate, di-*n*-octyl phthalate, and ethyl acetate, were used instead of dimethyl phthalate as the additive to clarify the effect of the ester structure on the formation of a cheek-brush morphology (Figure 2-13). The other experimental conditions, i.e., the concentrations of titanium tetraisopropoxide and esters, heating rate, and holding time at the final temperature, were fixed at 0.1 mol/L, 0.5 mol/L, 5.4 °C/min, 300 °C, and 10 min, respectively. Methyl benzoate, which has only one ester bond, gave a well-formed cheek-brush morphology (Figures 2-13a, 2-14), indicating that one ester bond is enough to produce this morphology. A well-formed cheek-brush morphology was also obtained with diethyl phthalate, which has one more methylene unit (Figures 2-13b, 2-15).

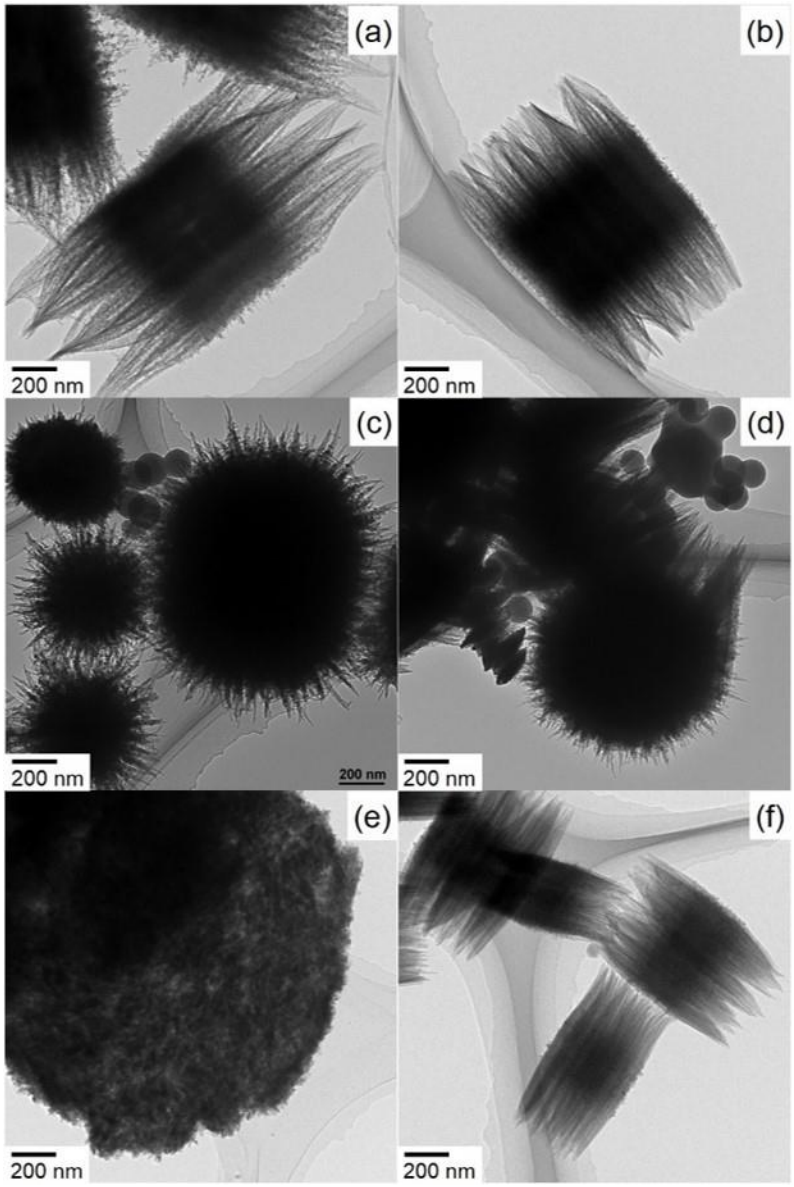

Figure 2-13. TEM images of TiO_2 assemblies obtained using (a) methyl benzoate and titanium tetraisopropoxide, (b) diethyl phthalate and titanium tetraisopropoxide, (c) dibutyl phthalate and titanium tetraisopropoxide, (d) di-*n*-octyl phthalate and titanium tetraisopropoxide, (e) ethyl acetate and titanium tetraisopropoxide, and (f) dimethyl phthalate and titanium tetra-*n*-butoxide.

In contrast, dibutyl and di-*n*-octyl phthalates as additives, which have longer alkyl chains as compared with above aromatic esters, gave urchin-like morphologies (Figures 2-13c, 2-13d, 2-16, 2-17). These observation suggests that the bulkiness of the alkyl chain is one of the important factors to control the growth of the length of brush structure.

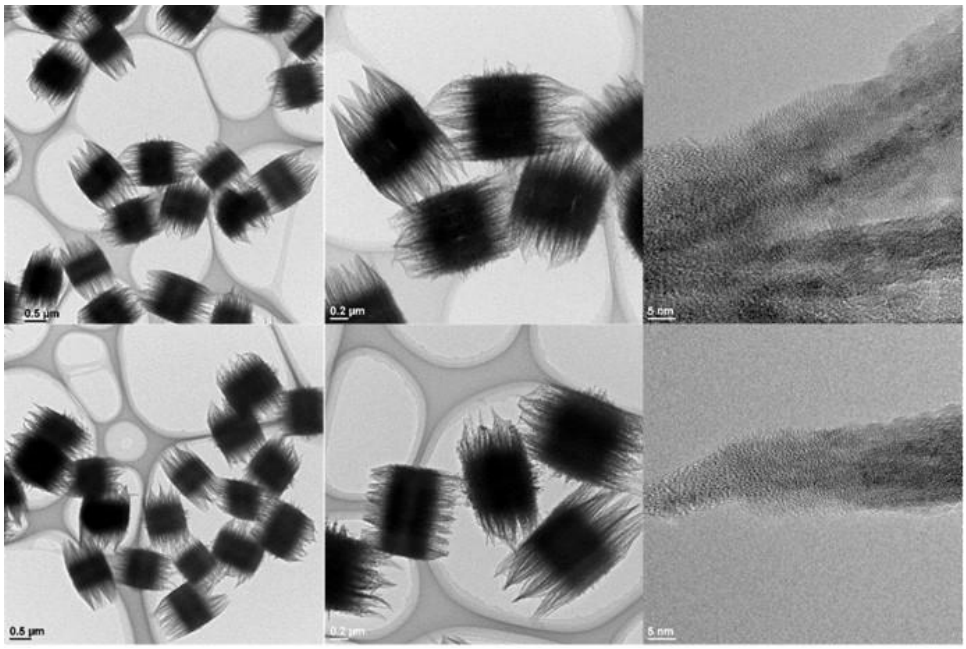

Figure 2-14. TEM images of TiO_2 assemblies obtained from precursor solutions consiting of methyl benzoate, titanium tetraisopropoxide, and methanol with heating rate 5.4 °C/min, 300 °C final temperature and 10 min holding at final temperature.

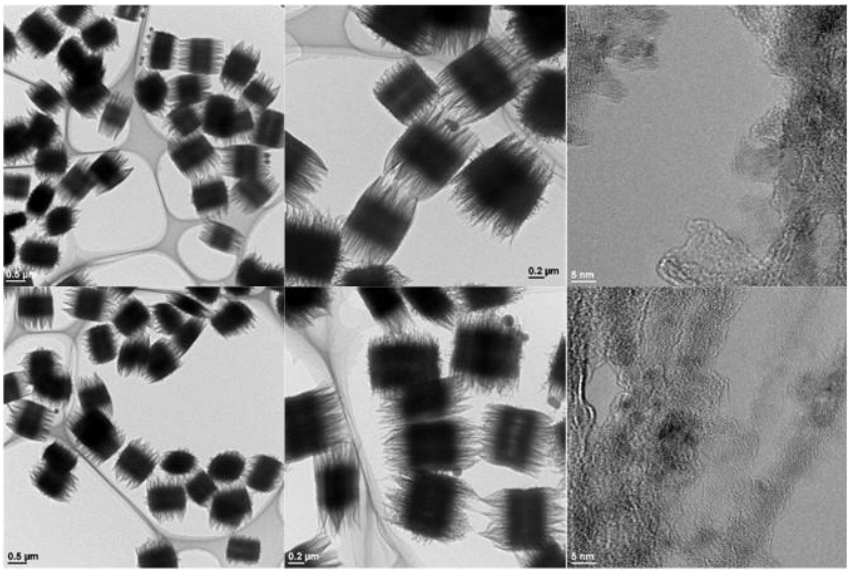

Figure 2-15. TEM images of TiO_2 assemblies obtained from precursor solutions consiting of diethyl phthalate, titanium tetraisopropoxide, and methanol with heating rate 5.4 °C/min, 300 °C final temperature and 10 min holding at final temperature.

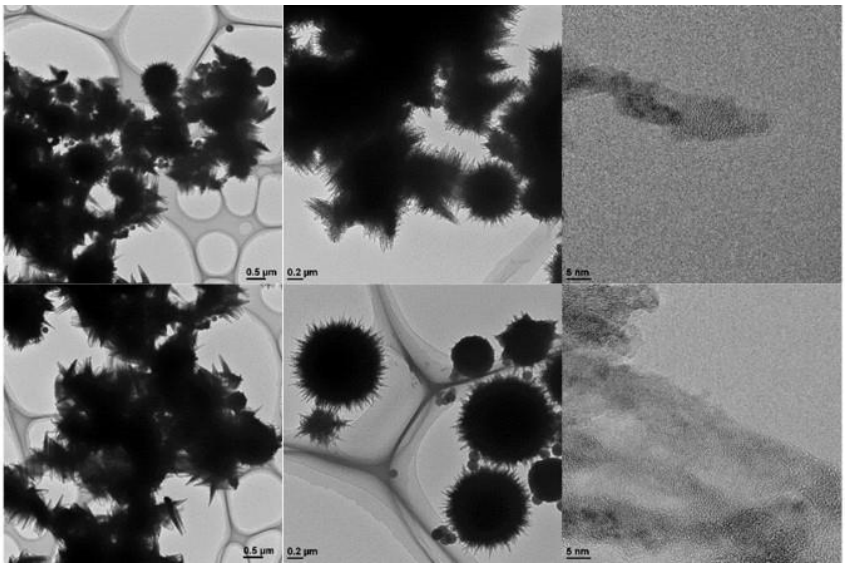

Figure 2-16. TEM images of TiO_2 assemblies obtained from precursor solutions consiting of di-*n*-butyl phthalate, titanium tetraisopropoxide, and methanol with heating rate 5.4 °C/min, 300 °C final temperature and 10 min holding at final temperature.

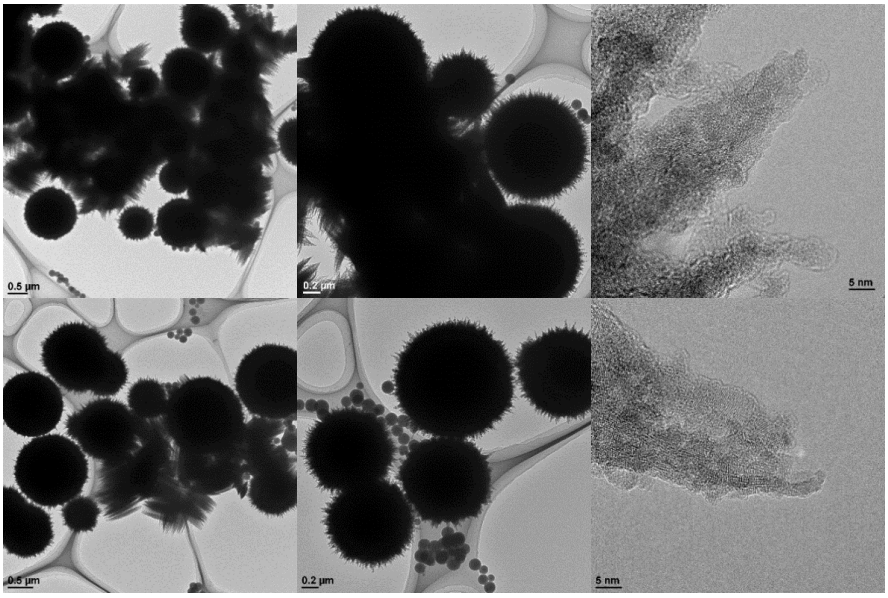

Figure 2-17. TEM images of TiO_2 assemblies obtained from precursor solutions consiting of di-*n*-octyl phthalate, titanium tetraisopropoxide, and methanol with heating rate 5.4 °C/min, 300 °C final temperature and 10 min holding at final temperature.

All the obtained assemblies contained needle-like crystals on the particle surface, regardless of the aromatic ester used. However, ethyl acetate, which is an aliphatic ester, gave a micron-sized sheet structure (Figures 2-13e, 2-18). This indicates the aromatic moiety in the ester compounds affects the formation of needle-like structure.

Another titanium alkoxide, namely titanium tetra-*n*-butoxide, also gave a perfect cheek-brush morphology (Figures 2-13f, 2-19), clearly indicating that the titanium alkoxide structure has almost no effect on cheek-brush morphology formation.

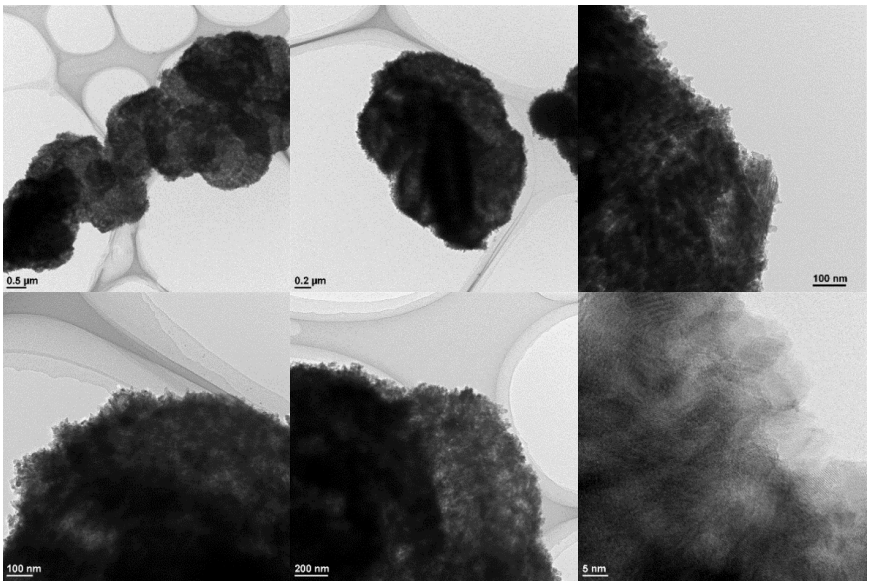

Figure 2-18. TEM images of TiO_2 assemblies obtained from precursor solutions consiting of ethyl acetate, titanium tetraisopropoxide, and methanol with heating rate 5.4 °C/min, 300 °C final temperature and 10 min holding at final temperature.

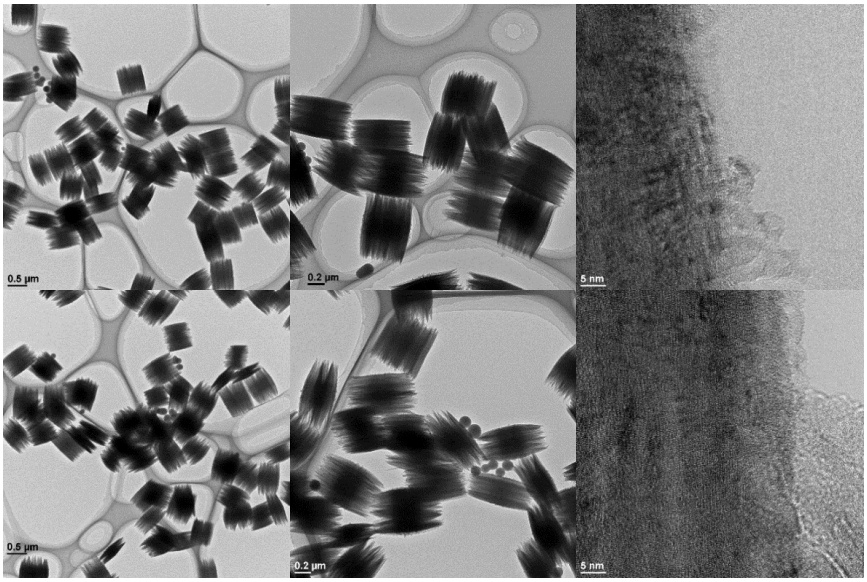

Figure 2-19. TEM images of TiO_2 assemblies obtained from precursor solutions consiting of dimethyl phthalate, titanium tetrabutoxide, and methanol with heating rate 5.4 °C/min, 300 °C final temperature and 10 min holding at final temperature.

2.3.2 Plausible mechanism of brush-like structure growth

As mentioned above, the critical conditions for cheek-brush morphology formation are i) allowing the precursor mixture to stand for 20 min before heating, ii) a final heating temperature of 300 °C, iii) a moderate heating rate of 5.4 °C/min, and iv) use of aromatic esters as additives. Based on all the experimental results, a plausible mechanism for formation of TiO_2 assemblies with a cheek-brush morphology is proposed, as shown in Figure 2-20. Judging from the periodic brush structure observed in TEM and SEM images, the cheek-brush morphology is supposed to be derived from an intermediate with striped structure consisted of titanium-rich phase and ester-rich phase generated during the standing step. In order to support this hypothesis, as shown in Figure 2-4, ESI-MS spectra of the precursor solution indicate the intermediates complexes consisting of several titanium tetramethoxide and methanol molecules. Thus, titanium-rich and ester-rich phases are assumed to be arranged alternately and independently in the stripe-like structure. The origin of the turbidity observed in the precursor mixture (Figure 2-5b) could be these clusters and/or cluster-derived higher molecular weight materials. It is important that cheek-brush morphology formation was never observed without an aromatic ester.

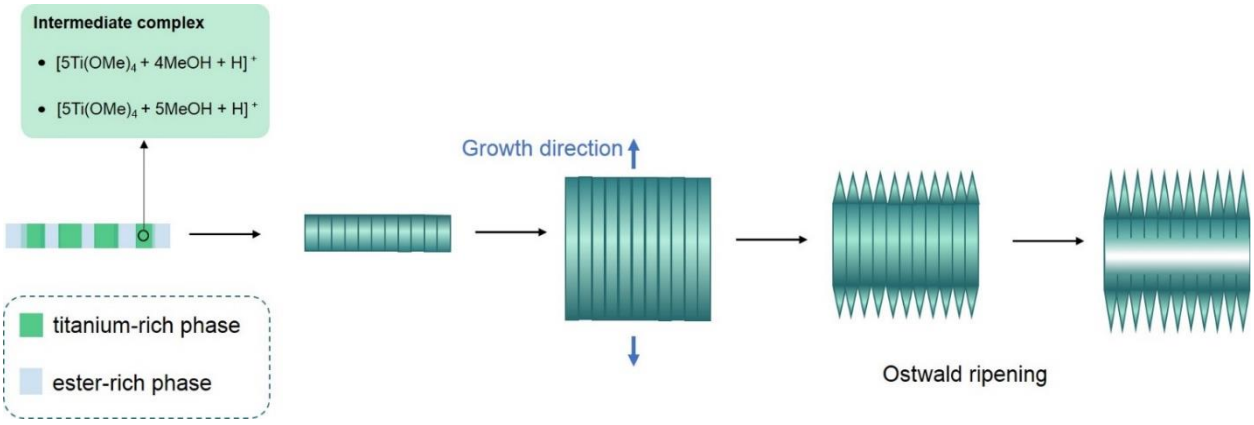

Figure 2-20. Plausible formation mechanism.

However, the same cluster peaks were observed for precursor mixtures with other aromatic esters in ESI-MS spectra (Figure 2-7), suggesting that the aromatic ester did not directly affect the formation of titanium tetramethoxide, but some soft architectures were formed between titanium tetramethoxide and the aromatic ester in the precursor mixtures, which could be dissociated under ESI-MS conditions. The stripe structure then grows in only one direction because of the prevention of fiber growth at side by the ester-rich phase. After that, water generated by methanol condensation under high-temperature conditions hydrolyses the titanium alkoxide to TiO_2. Pyrolysis of clusters under high-temperature solvothermal conditions can also produce TiO_2. The ester-rich phase then dissolves in methanol to give a cheek-brush morphology with nanofiber bundles. Further heating would induce Ostwald ripening to elongate the needles and construct hollow structures.[36] Prolonged heating causes shrinkage of the needle structures, resulting in highly crystalline TiO_2, as shown in Figures 2-9g and h. Similar structure of short fibers were obtained when the cheek-brush assemblies were further calcined at high temperature of 600 °C as shown in SEM image (Figure 2-21), confirming their structure stability as consistent with TG/DTA result (Figure 2-22).

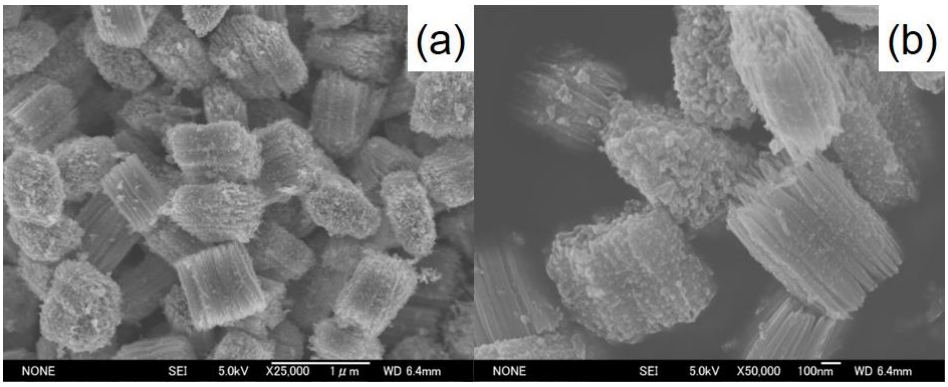

Figure 2-21. SEM images of the cheek brush TiO_2 after calcination at 600 °C with heating rate 10 °C/min.

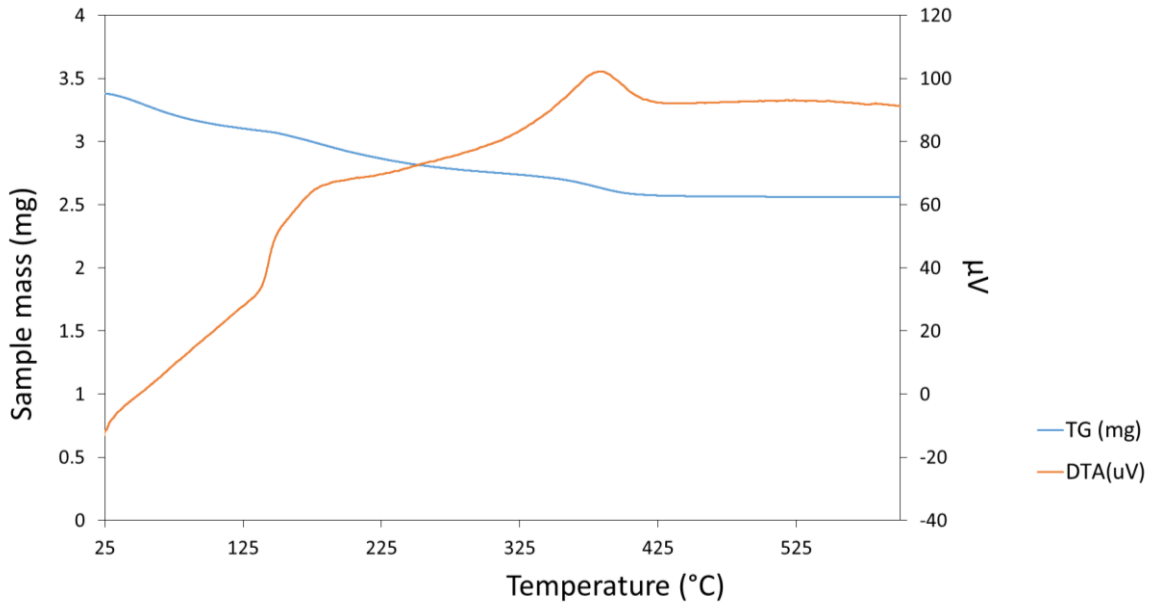

Figure 2-22. TGA/DTA curves of the cheek brush TiO_2 in air with heating rate 10 °C/min.

2.3.3 Nanocomposite hydrogel with cheek-brush TiO_2

To emphasize the surface properties of the cheek-brush-shaped nanofiber bundles of TiO_2, they were attempted to be used as a hydrogel crosslinker. Typically, a hydrogel consists of a small amount of polymer and a large amount of water. The mechanical properties of hydrogels, such as ultimate tensile strength and elongation ability, are sensitive to the crosslinker shape. The interactions between assemblies and polymer chains can be easily estimated from the mechanical properties, because the large numbers of nanofibers in the assemblies become entangled with the polymer chains as illustrated in Figure 2-23. The effect of the shape of TiO_2 prepared using the similar solvothermal method was investigated by measuring the tensile strength of a hydrogel prepared from 20wt% polymer and 0.02wt% TiO_2 nanoparticle assembly crosslinkers with spherical, urchin-like, and cheek-brush shapes. The tensile strengths of poly(*N*-

isopropylacrylamide) hydrogels containing various shapes of TiO_2 nanoparticle were measured, as shown in Figure 2-24. Table 2-1 shows the ultimate tensile strengths and elongation abilities measured from the stress-strain curves of hydrogel samples prepared using cheek-brush assemblies of TiO_2 or other shapes of TiO_2 nanoparticles as shown in Figure 2-25. The hydrogel containing cheek-brush nanoparticle assemblies has the highest ultimate tensile strength and elongation ability, i.e., around 6900 kPa and 600%, respectively. The ultimate tensile strength is 11% higher and the elongation ability is 9.1% higher than those of the hydrogel without a crosslinker. By mean of this, the hydrogel with cheek-brush TiO_2 can withstand at higher tensile force before it was broken and stretched longer before it was permanently deformed comparing with the blank hydrogel without a crosslinker.

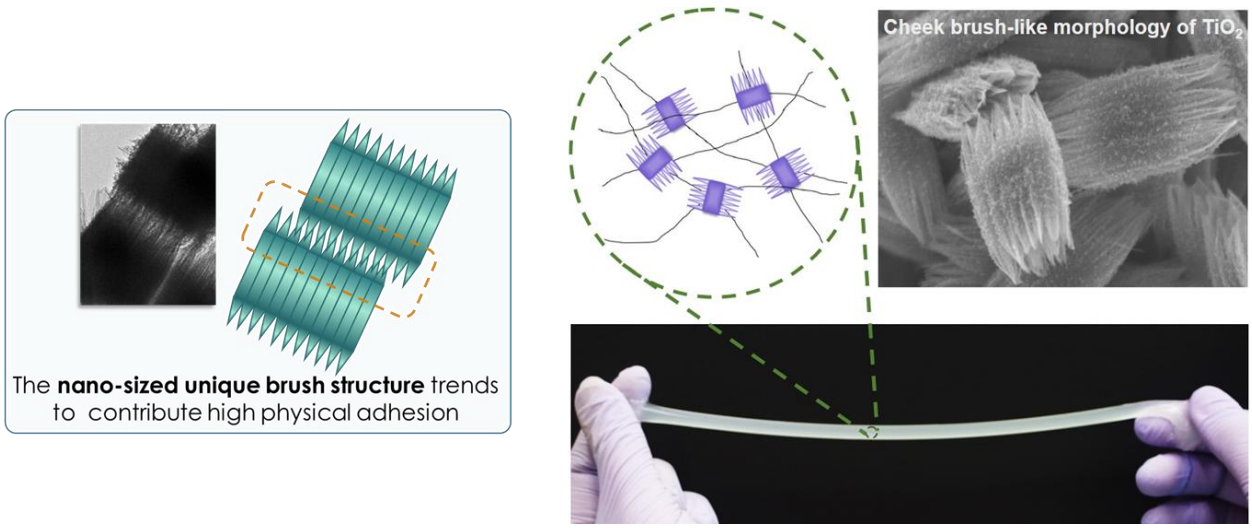

Figure 2-23. Photographs and illustration indicating entangled polymer chains with brush structure.

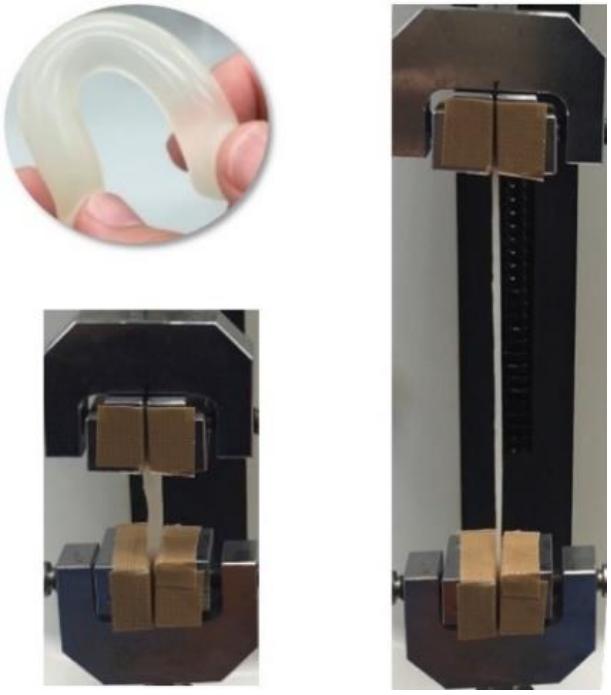

Figure 2-24. Photographs of tensile tests on polymer hydrogel containing cheek-brush TiO_2 nanoparticle assemblies as crosslinker

Table 2-1. Ultimate tensile strengths and elongation abilities of 20wt% poly(*N*-isopropyl acrylamide) hydrogels containing different types of crosslinkers.

	ultimate tensile Strength		elongation ability	
	(kPa)	% improvement compared with blank	(%)	% improvement compared with blank
Blank	6200		550	
Cheek-brush TiO_2	6900	+11	600	+9.1
MARIMO TiO_2	5500	-11	450	-18
Urchin-like	6500	+4.8	580	+5.4

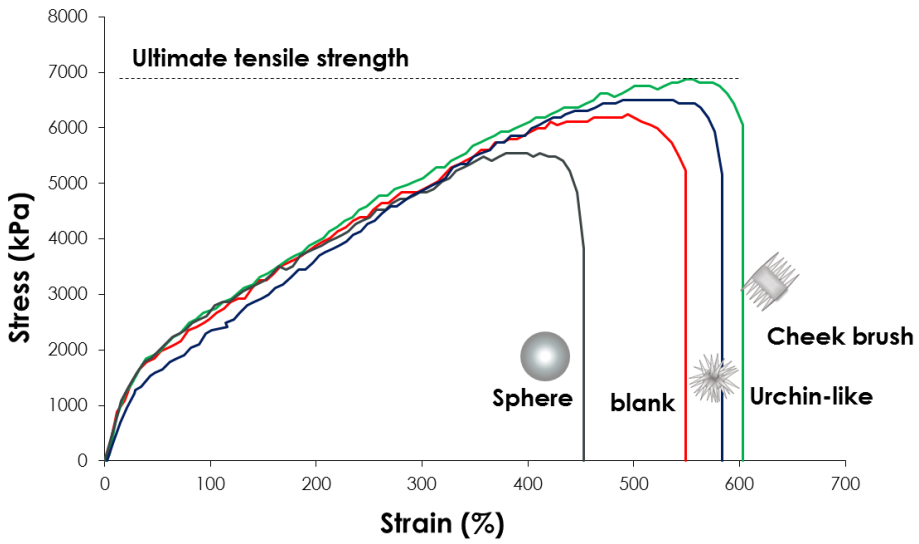

Figure 2-25. Stress–strain curves for 20wt% poly(*N*-isopropylacrylamide) hydrogels without crosslinker and with 0.02wt% differently shaped TiO_2 crosslinkers, i.e., cheek-brush, urchin-like, and spherical (MARIMO).

Although there are several researches that have been studied and shown the improvement of tensile strength in various kinds of polymer hydrogels containing TiO_2 nanoparticles with spherical shape as a filler, the optimum amount of TiO_2 nanoparticles was found to be at least 0.2wt% in the hydrogels.[36-38] In this work, only 0.02wt% of MARIMO TiO_2, spherical TiO_2 nanoparticle assembly, were used in the hydrogels in order to compare the property with the cheek-brush TiO_2 nanoparticle assembly. The results of tensile measurement in Figure 2-23 and Table 2-1 show that both tensile strength and elongation ability of the hydrogel containing MARIMO TiO_2 were decreased, confirming that MARIMO structure did not act as an effective crosslinker in hydrogel formation. Thus, the tensile tests on hydrogels containing the crosslinkers show that higher-ordered nanoparticle assemblies consisting of brush-like structures significantly improve the tensile strength and elongation ability of the hydrogel.

2.4 Conclusions

Nanofiber bundles of anatase TiO_2 with a cheek-brush morphology were successfully synthesized by a one-pot, single-step, solvothermal reaction from titanium tetraalkoxides and aromatic esters in methanol at 300 °C under high pressure. The morphology of the product can be tuned by adjusting the reaction parameters, i.e., the additive concentration, heating rate, reaction time, and standing of precursors. Use of the cheek-brush nanoparticle assemblies as a crosslinker improved the mechanical properties of a polymer hydrogel. This study provides new insights into the synthesis of novel TiO_2 nanomaterials and the chemistry of hydrogels with three-dimensional physical crosslinking.

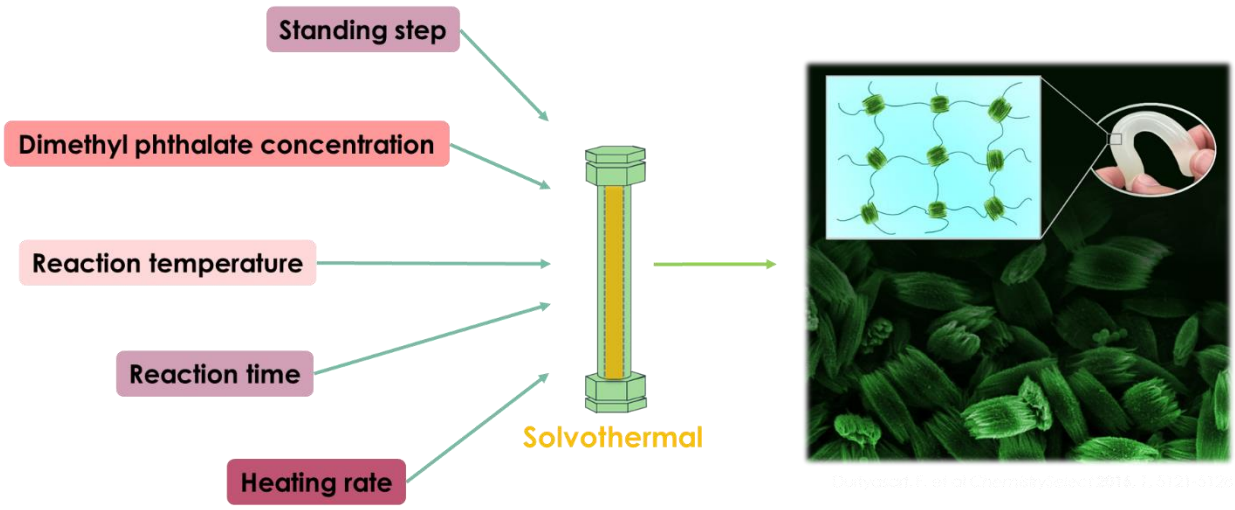

Figure 2-26. Illustration of the conclusions for "cheek brush" TiO_2 synthesis and its application.

References

[1] Sun J.-Y.; Zhao X.; Illeperuma W. R. K.; Chaudhuri O.; Oh K. H.; Mooney D. J.; Vlassak J. J.; and Suo Z. Highly stretchable and tough hydrogels, *Nature* **2012**, 489, 133–136.

[2] Nakajima T.; Furukawa H.; Tanaka Y.; Kurokawa T.; Osada Y.; and Gong J. P. True Chemical Structure of Double Network Hydrogels, *Macromolecules* **2009**, 42, 2184.

[3] Esser-Kahn A. P.; Iavarone A. T.; and Francis M. B. Metallothionein-cross-linked hydrogels for the selective removal of heavy metals from water, *J. Am. Chem. Soc.* **2008**, 130, 15820–15822.

[4] Fukasawa M.; Sakai T.; Chung U.-I.; and Haraguchi K. Synthesis and mechanical properties of a nanocomposite gel consisting of a tetra-PEG/clay network, *Macromolecules* **2010**, 43, 4370–4378

[5] Wang J.; Lin L.; Cheng Q.; Jiang L. A Strong Bio-Inspired Layered PNIPAM–Clay Nanocomposite Hydrogel, *Angew. Chem. Int. Ed.* **2012**, 51, 4676–4680.

[6] Spizzirri U. G.; Curcio M.; Cirillo G.; Spataro T.; Vittorio O.; Picci N.; Hampel S.; Iemma F.; and Nicoletta, F. P. Recent Advances in the Synthesis and Biomedical Applications of Nanocomposite Hydrogels, *Pharmaceutics* **2015**, 7, 413–437.

[7] Haraguchi K.; and Takehisa T. Nanocomposite Hydrogels: A Unique Organic–Inorganic Network Structure with Extraordinary Mechanical, Optical, and Swelling/De-swelling Properties, *Adv. Mater.* **2002**, 14, 1120–1124.

[8] Ahmed M. E. Hydrogel: Preparation, characterization, and applications: A review, *J. Adv.Res.* **2015**, 6, 105-121.

[9] Yamamoto H.; and Tanisho H. Gel formation and its properties as hydrogel of cross-linked lysine polypeptides using organic cross-linking agents, *Mater. Sci. Eng. C* **1993**, 1, 45-51.

[10] Kabiri K.; Omidian H.; Hashemi S. A.; and Zohuriaan-Mehr M. J. Synthesis of fast-swelling superabsorbent hydrogels: effect of crosslinker type and concentration on porosity and absorption rate, *Eur. Polym. J.* **2003**, 39, 1341-1348.

[11] Haraguchi K.; Farnworth R.; Ohbayashi A.; and Takehisa, T. Compositional Effects on Mechanical Properties of Nanocomposite Hydrogels Composed of Poly(*N*,*N*-dimethylacrylamide) and Clay, *Macromolecules* **2003**, 36, 5732–5741.

[12] Haraguchi K.; Takehisa T.; and Fan S. Effects of Clay Content on the Properties of Nanocomposite Hydrogels Composed of Poly(*N*-isopropylacrylamide) and Clay, *Macromolecules* **2002**, 35, 10162–10171.

[13] Singh T.; Patnaik A.; Satapathy B. K.; Kumar M.; and Tomar B. S. Effect of Nanoclay Reinforcement on the Friction Braking Performance of Hybrid Phenolic Friction Composites, *J. Mater. Eng. Perform.* **2012**, 22, 796–805.

[14] Wang Q.; Mynar J. L.; Yoshida M.; Lee E.; Lee M.; Okuro K.; Kinbara K.; and Aida T. High-water-content mouldable hydrogels by mixing clay and a dendritic molecular binder, *Nature* **2010**, 463, 339–343.

[15] Tamesue S.; Ohtani M.; Yamada K.; Ishida Y.; Spruell J. M.; Lynd N. A.; Hawker C. J.; and Aida T. Linear versus Dendritic Molecular Binders for Hydrogel Network Formation with Clay Nanosheets: Studies with ABA Triblock Copolyethers Carrying Guanidinium Ion Pendants, *J. Am. Chem. Soc.* **2013**, 135, 15650–15655.

[16] Wu L.; Ohtani M.; Tamesue S.; Ishida Y.; and Aida T. High water content clay–nanocomposite hydrogels incorporating guanidinium-pendant methacrylamide: Tuning of mechanical and swelling properties by supramolecular approach, *J. Polym. Sci. A Polym. Chem.* **2013**, 52, 839–847.

[17] Wu C.-J.; Gaharwar A. K.; Chan B. K.; and Schmidt G. Mechanically Tough Pluronic F127/Laponite Nanocomposite Hydrogels from Covalently and Physically Cross-Linked Networks, *Macromolecules* **2011**, 44, 8215.

[18] Haraguchi K.; Li H.-J.; Matsuda K.; Takehisa T.; and Elliott, E. Mechanism of Forming Organic/Inorganic Network Structures during In-situ Free-Radical Polymerization in PNIPA−Clay Nanocomposite Hydrogels, *Macromolecules* **2005**, 38, 3482–3490.

[19] Liu Y.; Zhu M.; Liu X.; Zhang W.; Sun B.; Chen Y.; and Adler H.-J. P. High clay content nanocomposite hydrogels with surprising mechanical strength and interesting deswelling kinetics, *Polymer* **2006**, 47, 1–5.

[20] Liu P.; Jiang L.; Zhu L.; and Wang A. Attapulgite/Poly(acrylic acid) Nanocomposite (ATP/PAA) Hydrogels with Multifunctionalized Attapulgite (org-ATP) Nanorods as Unique Cross-linker: Preparation Optimization and Selective Adsorption of Pb(II) Ion, *ACS Sustain. Chem. Eng.* **2014**, 2, 643–651.

[21] Ferris C. J.; and in het Panhuis M. Conducting bio-materials based on gellan gum hydrogels, *Soft Matter* **2009**, 5, 3430–3437.

[22] Holloway J. L.; Lowman A. M.; VanLandingham M. R.; and Palmese G. R. Interfacial optimization of fiber-reinforced hydrogel composites for soft fibrous tissue applications, *Acta Biomater.* **2014**, 10, 3581–3589.

[23] Nguyen V. G.; Thai H.; Mai D.H.; Tran H. T.; Tran D. L.; and Vu, M. Effect of titanium dioxide on the properties of polyethylene/TiO_2 nanocomposites, *Compos. B* **2013**, 45, 1192-1198.

[24] Dzunuzovic E.; Jeremic K.; and Nedeljkovic J. M. In situ radical polymerization of methyl methacrylate in a solution of surface modified TiO_2 and nanoparticles, *Eur. Polym. J.* **2007**, 43, 3719-3726.

[25] Wu G.; Gan S.; Cui L.; and Xu Y. Preparation and characterization of PES/TiO_2 composite membranes, *Appl. Surf. Sci.* **2018**, 254, 7080-7086.

[26] Sathish S.; Chandar B.; and Bhavyasree B. T. Nano Composite PVA-TiO_2 Thin Films for OTFTs, *Adv. Mater. Res.* **2013**, 678, 335-342.

[27] Xu B.; Li H.; Wang Y.; Zhang G.; and Zhang Q. High strength nanocomposite hydrogels with outstanding UV-shielding property, *Polym. Compos.* **2016**, 37, 810-817.

[28] Li C.; Zheng Y. F.; and Lou X. Calcification capacity of porous pHEMA-TiO_2 composite hydrogels, *J. Mater. Sci. Mater. Med.* **2009**, 20, 2215-2222.

[29] Zhai Y.; Duan H.; Meng X.; Cai K.; Liu Y.; and Lucia L. Reinforcement Effects of Inorganic Nanoparticles for Double-Network Hydrogels, *Macromol. Mater. Eng.* **2015**, 12, 1290-1299.

[30] Zhang D.; Yang J.; Bao S.; Wu Q.; and Wang Q. Semiconductor nanoparticle-based hydrogels prepared via self-initiated polymerization under sunlight, even visible light, *Sci. Rep.* **2013**, 3, 1399.

[31] Liu M.; Ishida Y.; Ebina Y.; Sasaki T.; and Aida T. Photolatently modulable hydrogels using unilamellar titania nanosheets as photocatalytic crosslinkers, *Nature Communications* **2013**, 4, 2029.

[32] Liu M.; Ishida Y.; Ebina Y.; Sasaki T.; Hikima T.; Takata M.; and Aida T. An anisotropic hydrogel with electrostatic repulsion between cofacially aligned nanosheets, *Nature* **2014**, 517, 68–72.

[33] Kim Y. S.; Liu M.; Ishida Y.; Ebina Y.; Osada M.; Sasaki T.; Hikima T.; Takata M.; and Aida T. Thermoresponsive actuation enabled by permittivity switching in an electrostatically anisotropic hydrogel, *Nature Materials* **2015**, 14, 1002–1007

[34] Wang P.; Ueno K.; Takigawa H.; and Kobiro K. Versatility of one-pot, single-step synthetic approach for spherical porous (metal) oxide nanoparticles using supercritical alcohols, *J. Supercrit. Fluids* **2013**, 78, 124–131.

[35] Stephens H. P.; and Dosch, R. G. Preparation of Catalysts IV, Elsevier, **1987**; Vol. 31.

[36] Yang H. G.; and Zeng, H. C. Preparation of Hollow Anatase TiO_2 Nanospheres via Ostwald Ripening, *J. Phys. Chem. B* **2004**, 108, 3492-3495.

CHAPTER III

Surface Activation of TiO_2 Spherical Nanoparticle Assemblies by Atmospheric Pressure Plasma Jet and their Photocatalytic Activity Enhancement

3.1 Introduction

Nanomaterials with porous structure are used in various applications such as catalysts, catalyst supports, and absorbents due to their large surface areas and specific surface properties. On the other hand, those properties make porous nanomaterials strongly adsorb/absorb contaminants on their surfaces, which would reduce their inherent properties as derived from their size-dependent lattice parameters.[1-3] These contaminants including residues from their preparation process or a trace amount of impurities should be removed from the surfaces to allow high performances when the nanomaterials are used in practical applications, which can include catalysts, catalyst supports, adsorbents, and electrodes.[4-8] Currently, thermal and chemical processes are commonly used to remove surface contaminants as the example shown in Figure 3-1.[9,10]

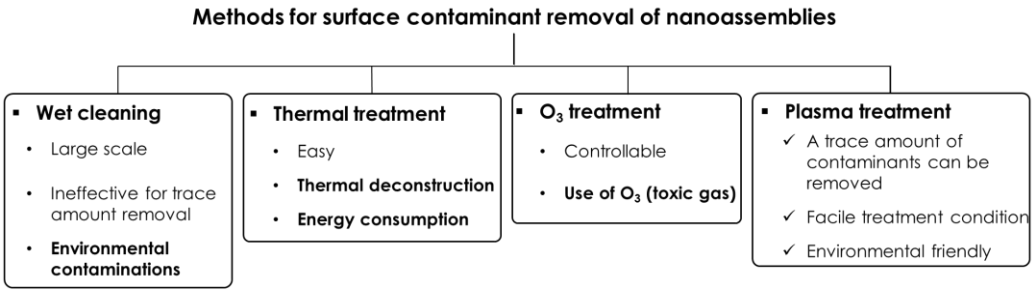

Figure 3-1. Schematic of methods for surface contaminant removal.

High temperature treatments are generally known to be one of the easiest ways to remove surface contaminants, however this consumes large amount of energy and often causes sintering or pore collapses that can result in loss of surface area, and thus low performance of catalysts. Chemical treatments sometimes require multi-step processes with concomitant waste treatments. Thus, simple, easy, and versatile non-thermal processes for surface treatment are necessary. Ozone (O_3) exposure and UV irradiation are relatively common methods of non-thermal surface treatment, especially in the field of thin-layer materials. However, in the case of O_3 treatment, contaminants can only be removed by diffusion of O_3 on the surface, while UV irradiation can only clean the outer surfaces of nanoparticles because of the difficulty of enabling UV light penetration deep inside the layers or nanoparticle agglomerates.[11,12]

Low-pressure plasma treatment is an alternative method of removing surface contaminants. This traditional plasma treatment often requires expensive vacuum equipment and high purity gases to generate plasma.[13-16] However, in recent years there has been much interest in developing plasmas that can operate at atmospheric pressure for use in cost-effective processes from the micrometer to the centimeter length scales. One alternative plasma device is the non-thermal helium atmospheric pressure plasma jet (APPJ), which can be utilized in a wide range of areas including biology, agriculture, medicine, and polymer science due to its facile operation under atmospheric conditions.[17-22] A helium APPJ generates highly reactive neutral and ionic species, which are delivered to the target surface via helium gas flow.[23-26] Helium is commonly used as a plasma medium, requiring a relatively low breakdown voltage and allowing plasma to be sustained at voltages below 10 kV at atmospheric pressure. The plasma is non-equilibrium; typically,

electron densities and temperatures in APPJs are $n_e \leq 10^{13}$ cm^{-3} and T_e = 1–2 eV, respectively.[27] Interestingly, the gas temperature is low, at close to room temperature.[22,28,29] As described above, when a helium APPJ is generated in ambient air, highly reactive oxygen species are generated by interactions between main plasma species (He^+ ions, metastable He, and electrons) and ambient air. ·O and ·OH are common reactive species due to the existence of O_2 and small amounts of moisture in air, and both are capable of oxidizing contaminants.[30-32] When compared to the diffusion controlled O_3 treatment and the surface UV treatments, helium APPJs can penetrate deep inside porous materials.[11,12] Moreover, a helium APPJ operated at room temperature and atmospheric pressure would cause less damage to fragile materials.

Nanoscale TiO_2 with a mesoporous structure has been focused on as one of the most promising functional materials.[33] However, the particles also suffer intrinsic contaminants on their surfaces because of the inherent properties of nanoparticles. The one-pot, single-step solvothermal was developed for a synthesis TiO_2 nanoparticle assemblies with mesoporous morphologies, which were named **m**icro/**m**eso-porously **a**rchitected **r**oundly **i**ntegrated **m**etal **o**xides (MARIMOs).[34] However, some of the organic materials used in the synthetic process remained in the final products as contaminants, which affected their activity when they were used as catalysts. Spherical mesoporous TiO_2 MARIMO assemblies could be an excellent probe to check the efficiency of the non-thermal helium APPJ treatment of nanomaterials as illustrated in Figure 3-2, since both the ultra-fine convex-concave nano-surface and the spherical secondary structure are quite fragile and sensitive to thermal circumstances, as sintering of the primary particles can occur to yield larger particles while the secondary spherical morphology can collapse easily.

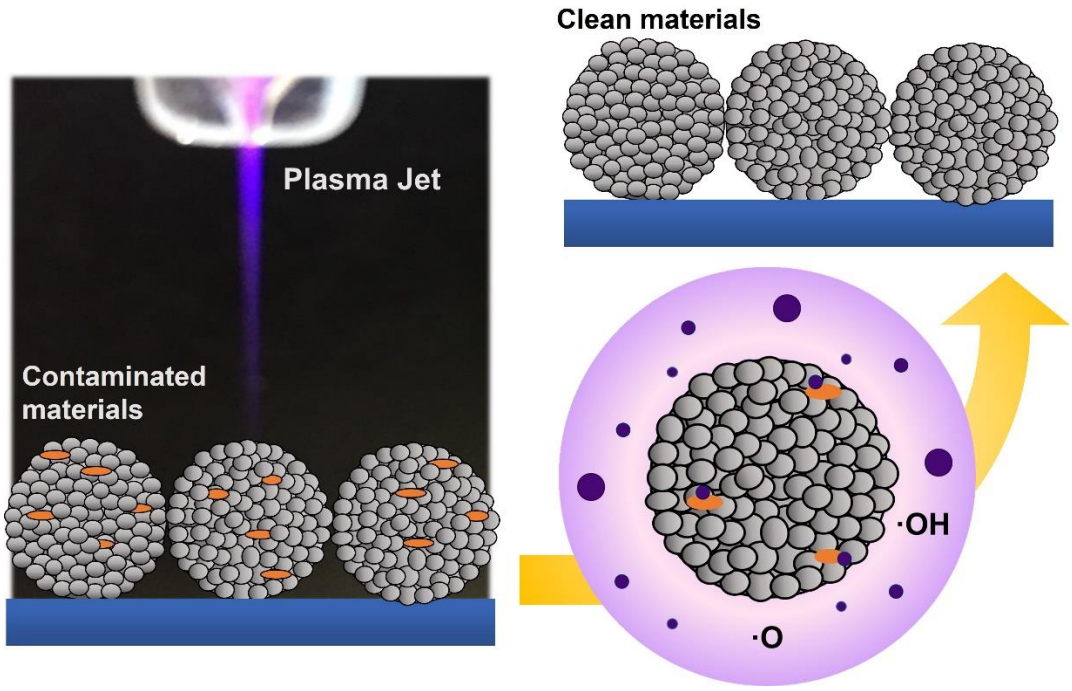

Figure 3-2 Illustrator of APPJ treatment on MARIMO assemblies of TiO_2

In this chapter, TiO_2 MARIMO nanoparticle assemblies were selected for use as a probe nanomaterial to check the efficiency of facile treatment by non-thermal helium APPJ. The efficiency was confirmed by LDI-TOF MS, which was firstly applied for the quantification of trace amount contaminants on porous nanomaterials. TEM, SEM, BET, and XRD measurements also use to confirm the treatment ability. Surface activation was estimated through photocatalytic degradation of an organic dye and transient photocurrent measurements under UV irradiation. The non-thermal helium APPJ apparatus was assembled according to a previously reported method as shown in Figure 3-3.[25]

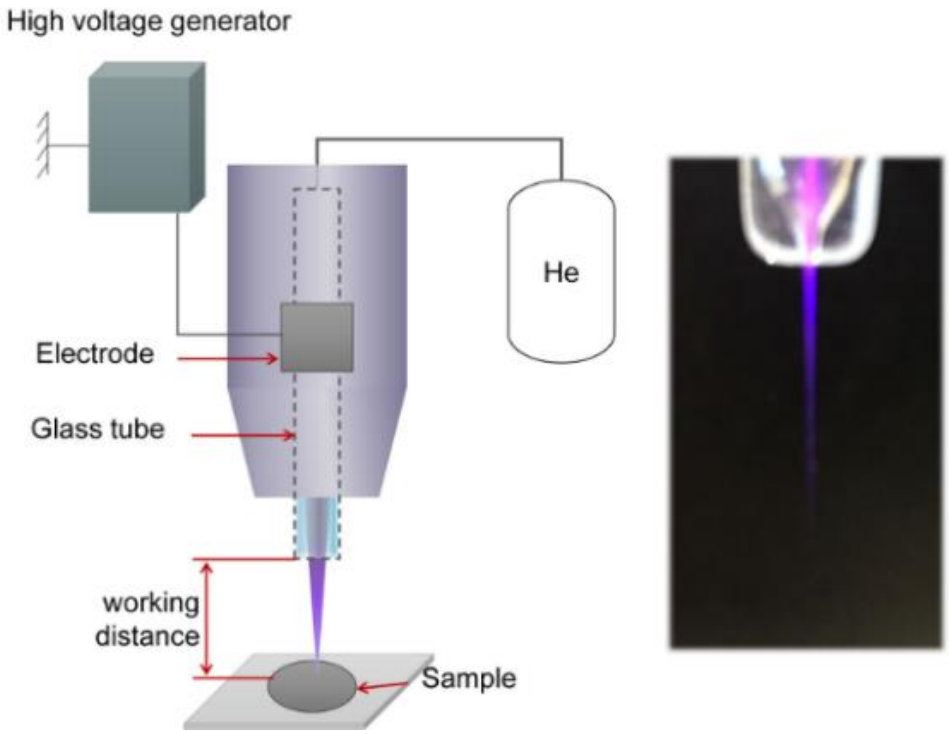

Figure 3-3. A schematic illustration of the non-thermal helium atmospheric pressure plasma jet (APPJ) apparatus used for nanomaterial treatment. Right: a photograph of helium plasma jet.

3.2 Experiment Section

The summary of experiment procedures is shown in Figure 3-4. TiO_2 MARIMOs as probe materials were investigated their contaminants and their properties before APPJ treatment. Then, those properties and contaminant levels were confirmed again. After APPJ treatment conditions were optimized, the material surface activation were investigated by their improvement on photocatalytic activity.

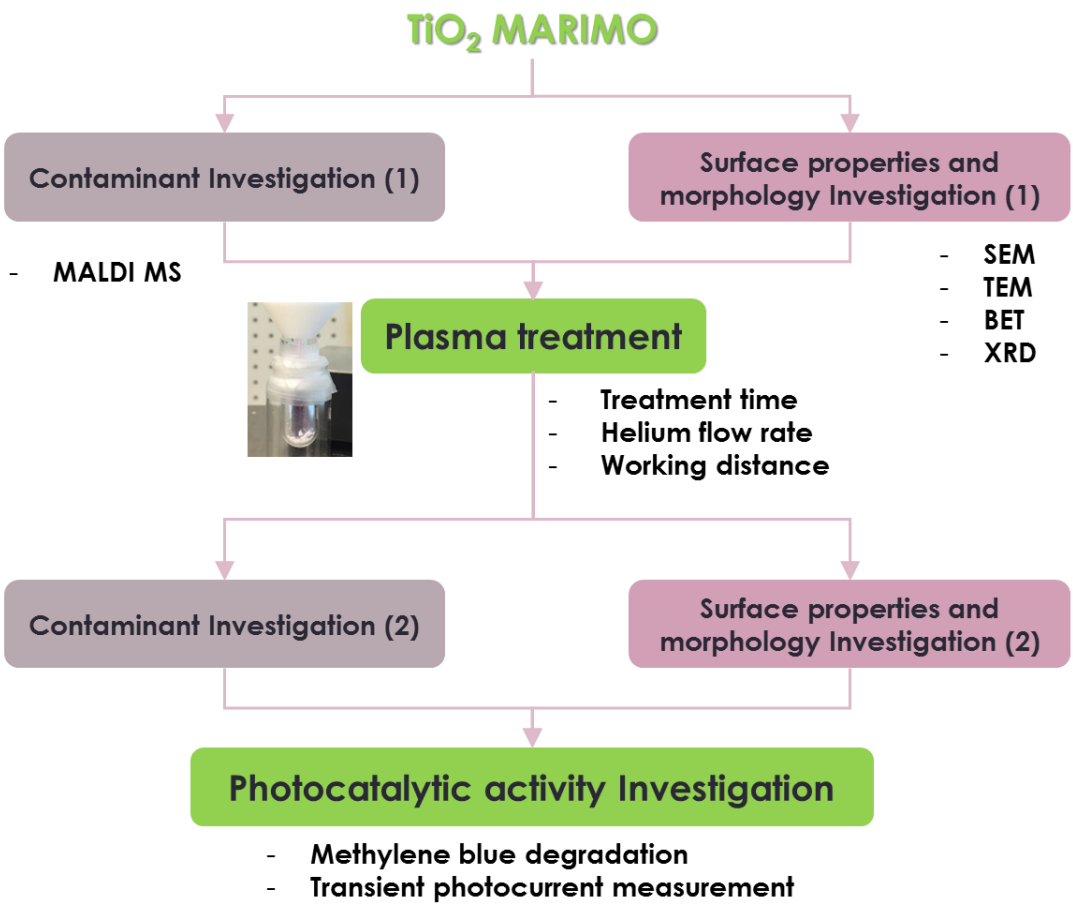

Figure 3-4 Schematic illustrated the summary of experimental procedures.

3.2.1 Materials

Methanol, ethanol, titanium tetraisopropoxide, formic acid, phthalic acid, methylene blue, triethylamine, and potassium chloride were purchased from Wako Pure Chemical Industries Co., Ltd. Commercial SiO_2 nanoparticles (Sciqas 1.0 μm) were received from Sakai Chemical Industry Co., Ltd. All chemicals were used as received without further treatment. Water purified by reverse osmosis was used throughout the experiments.

3.2.2 Synthesis of TiO_2 nanoparticle assemblies

TiO_2 MARIMO, cheek-brush, and urchin-like assemblies were prepared using previously reported methods.[34,35] Precursor solutions containing organic additives (0.5 mol/L) were prepared by mixing an aliquot of each organic additive with methanol (3.5 mL) using a Vortex mixer, followed by addition of titanium tetraisopropoxide (105 µL, 0.353 mmol). The precursor solution was transferred to an SUS-316 stain-less-steel tubular reactor with an inner volume of 10 mL. The reactor was sealed with a screw cap and heated at a rate of 5.4 °C/min to 300 °C, and then this temperature was maintained for 10 min. The reaction was quenched by placing the reactor in an ice-water bucket. The obtained mixture was centrifuged and washed with methanol; this procedure was repeated three times. The final suspended mixture was completely dried under vacuum and a powdery product was obtained.

3.2.3 *Plasma treatment*

The system consisted of a 15 cm glass tube and an external electrode in a cylindrical dielectric barrier discharge configuration.[36] The nozzle exit was tapered from an inner diameter of 4 mm to 800 µm at the orifice. The emerging plasma jet was used to treat the catalysts. Helium gas was fed through the tube at a flow rate of 1.62 L/min. A sinusoidal high voltage of 10 kV at a fixed frequency of 50 kHz was applied to sustain the helium plasma. The length of the emerging plasma jet was 1 cm under the plasma operating conditions. Catalyst powder was placed downstream of the plasma jet. The working distance from the nozzle tip to the sample surface and the exposures time were varied.

3.2.4 *Nanoparticle assembly characterization*

The morphologies of the obtained materials were observed using scanning electron microscopy (FE-SEM, Hitachi S8020) and transmission electron microscopy (TEM, JEOL JEM-2100F). The crystalline phase was identified by X-ray diffraction (XRD, Cu Kα radiation, Rigaku SmartLab). Mass spectra were obtained using laser desorption/ionization time-of-flight mass spectrometry (LDI-TOF MS, Bruker Autoflex speed TOF/TOF).

3.2.5 Evaluation of photocatalytic activity

The photocatalytic activities of the prepared and plasma-treated TiO_2 spherical nanoparticle assemblies were evaluated by methylene blue degradation. In these reactions, 5 mg of TiO_2 MARIMO assemblies were added to well-mixed aqueous solutions containing 10 mg/L of methylene blue. The suspensions were stirred for 1 h in the dark to achieve an adsorption/desorption equilibrium. The suspensions were irradiated with UV light (300 W, Xenon Light Source MAX-301, Asahi Spectra Co., Ltd.) at room temperature. UV-Vis spectroscopy was used to measure the absorbance of the solution at given time intervals.[37]

3.2.6 Measurement of photocurrent

The photocurrent-time was measured using an electro-chemical analyzer (ECstat-300, EC Frontier Co., Ltd.) in a standard three-compartment cell consisting of a working electrode, a Pt-coil counter electrode, and a Ag/AgCl reference electrode. The working electrodes were made by drop casting TiO_2 MARIMO assemblies onto ITO glasses. Suspensions of 7 mg TiO_2 MARIMO assemblies in 1 mL methanol were prepared, and then 10 µL of these suspensions were dropped on-to 1 cm × 1 cm areas of the ITO glass electrodes (1 cm × 5 cm). The electrodes were soaked in

an electrolyte containing 0.1 mol/L of KCl and 0.1 mol/L of triethylamine in water during the measurements as an illustration shown in Appendix B, which were performed under UV light (300 W, Xenon Light Source MAX-301, Asahi Spectra Co., Ltd.) irradiation.

3.3 Results and Discussion

3.3.1 Effect of plasma treatment on surface morphology of TiO_2

The previously stated electron temperature of non-thermal helium APPJ is high enough to damage the fragile ultra-fine convex-concave nano-surface morphologies of the probe TiO_2 MARIMO assemblies under some operating conditions, thus the APPJ parameters were optimized as follows: i) the working distance from the nozzle tip to the sample, ii) the helium flow rate, and iii) the treatment time. These should be considered to obtain sufficiently clean assembly surfaces without damaging the morphology and surface properties of the probe TiO_2 MARIMO assemblies. Frequent collisions between neutral gas and electrons under atmospheric conditions mean that the electron energy reduces exponentially as the distance from the plasma region increases.[38] Thus, the working distance was altered with a fixed helium flow rate of 1.62 L/min and a treatment time of 20 min. As shown in Figure 3-5, at a distance of 1 cm, several spherical TiO_2 MARIMO assemblies were fused to afford larger assemblies with *cauliflower* shape. However, no changes in the spherical mesoporous morphology were observed when a distance of 2 cm

was used. Thus, the working distance is crucial to morphological changes in the probe TiO_2 MARIMO assemblies.

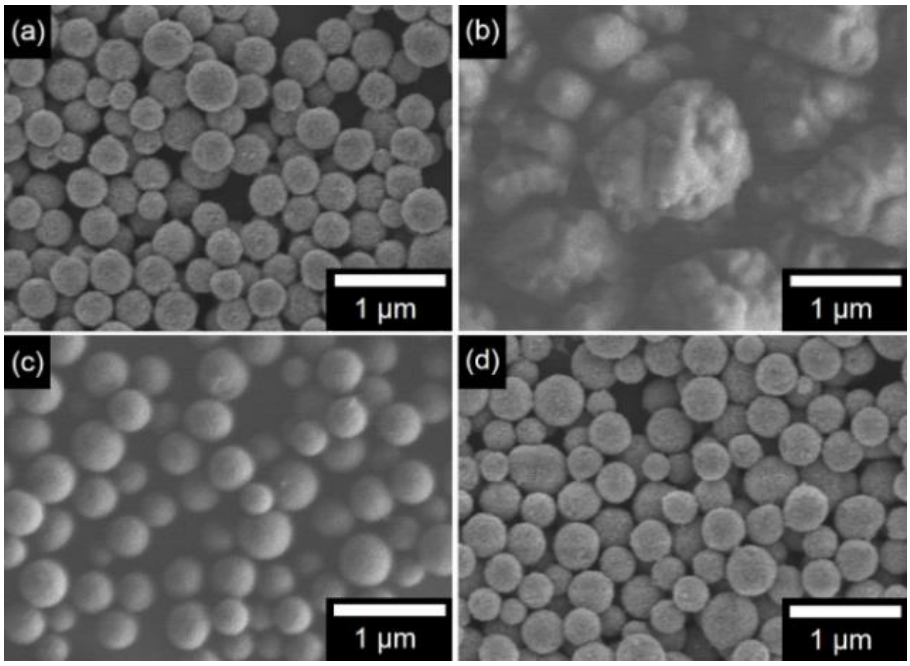

Figure 3-5. SEM images of TiO_2 MARIMO assemblies: (a) before treatment, after APPJ treatment for 20 min at a helium flow rate of 1.62 mL/min and working distances of (b) 1 cm and (c) 2 cm, and (d) after APPJ treatment for 60 min with a working distance of 2 cm.

3.3.2 Surface contaminant detections by SALDI-MS

To evaluate the cleanliness of the TiO_2 MARIMO assemblies, a new approach utilizing laser desorption/ionization time-of-flight mass spectrometry (LDI-TOF MS) was used. Matrix-assisted LDI-TOF MS (MALDI-TOF MS) using low molecular weight organic matrices is a well-known method of determining the mass-to-charge ratios (*m*/*z*) of organic compounds, polymers, biopolymers, etc.[39] Another type of surface-assisted LDI-

TOF MS (SALDI-TOF MS) using inorganic surface instead of organic matrices has been developed.[40] Here, the SALDI-TOF MS technique is extended to the detection of contaminants on the surfaces of nanomaterials. A similar approach to the detection of surface organic contaminants by time-of-flight secondary ion mass spectrometry (TOF-SIMS) using a pulsed Bi_3^+ beam has also been reported.[41] However, LDI-TOF MS instruments are popular in laboratories, and as the technique in the current study uses a laser instead of a Bi_3^+ beam, it is more versatile.

As shown in Figure 3-6, several peaks derived from contaminants were observed in the mass spectrum of the as-prepared TiO_2 MARIMO assemblies. However, these peaks completely disappeared after APPJ treatment under suitable conditions. This preliminary experiment confirmed the potential of non-thermal helium APPJ treatment for the removal of contaminants from the surfaces of the assemblies.

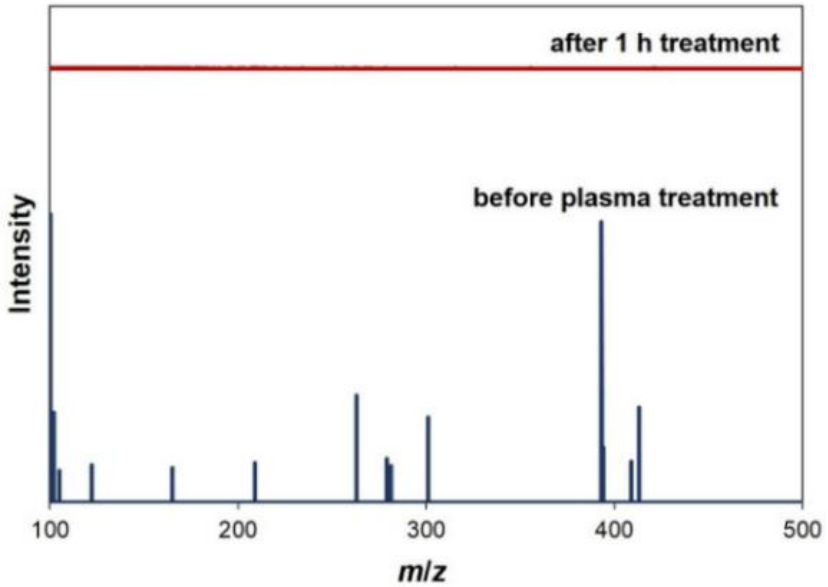

Figure 3-6 Mass spectra of TiO_2 MARIMO assemblies before and after APPJ treatment for 1 h at helium flow rate of 1.62 mL/min and a working distance of 2 cm.

In order to quantify the cleaning efficiency, the percentage decrease in the intensity of the main peak seen in the spectrum of the TiO_2 MARIMO assemblies (*m/z* = 393, Figure 3-7), was defined as expressed in Equation (1).

$$\%\text{decrease} = (I_0\text{-}I)/I_0 \times 100\% \quad (1)$$

Figure 3-7a shows that there was no significant trend in %decrease when the helium flow rate was varied between 0.8 and 1.9 L/min at a fixed working distance of 1 cm and a fixed treatment time of 20 min. However, treatment time was a critical factor when cleaning the TiO_2 MARIMO assemblies, as shown in Figure 3-7b. A treatment time of 60 min was necessary for 100% removal of the contaminants, suggesting that it takes time for the APPJ to reach deep inside of the mesoporous spherical assemblies.

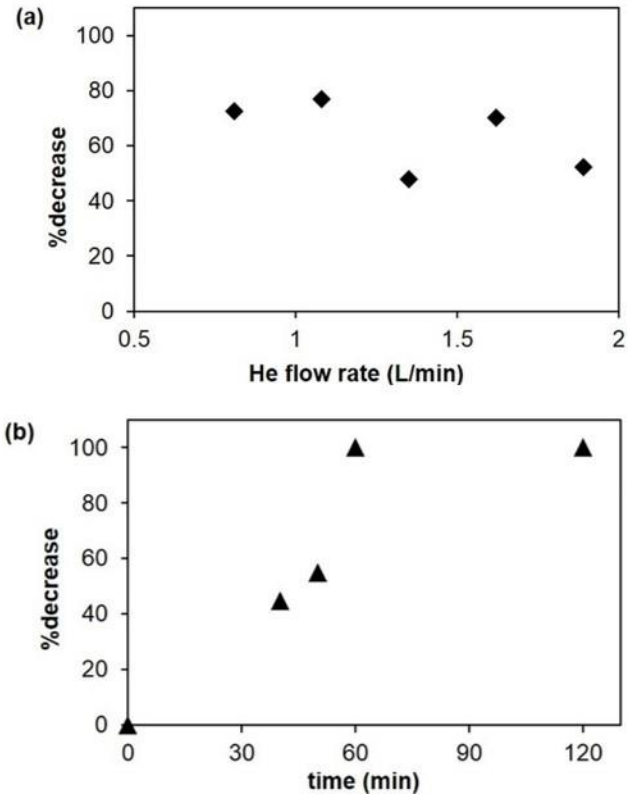

Figure 3-7. Plots of percentage decrease in the intensity of the main peak (*m/z* = 393) against (a) helium flow rate and (b) treatment time.

The TiO_2 MARIMO assemblies were sufficiently cleaned without any damage to the nano convex-concave morphology under the following optimal plasma treatment conditions: working distance = 2 cm, helium flow rate = 1.62 L/min, and treatment time = 1 h. This was confirmed by SEM and TEM observations, as shown in Figure 3-5 and 3-8. N_2 adsorption/desorption isotherms before and after the APPJ treatment of the TiO_2 MARIMO assemblies resulted in similar patterns (Fig. 3-9). The calculated BET specific surface areas were also similar, with values of 180 and 174 m^2/g for TiO_2 spherical nanoparticle assemblies before and after the APPJ treatment, respectively.

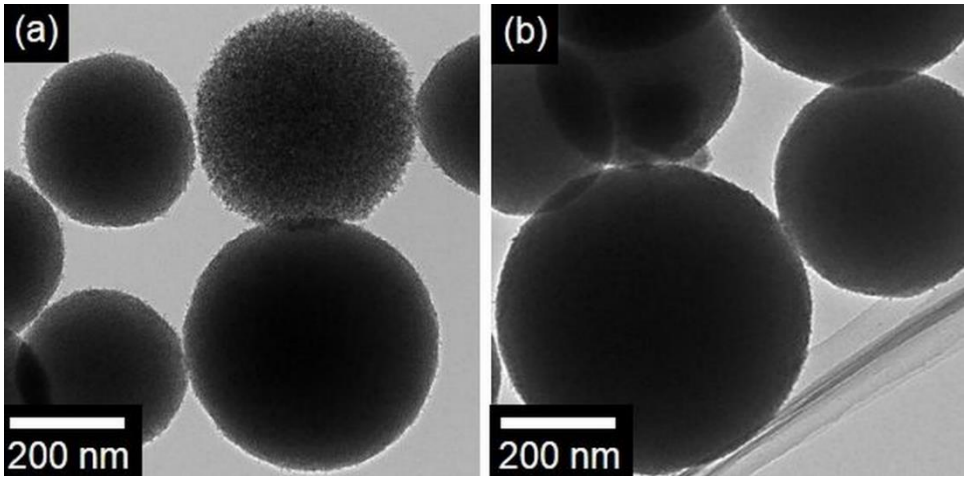

Figure 3-8. TEM images of TiO_2 MARIMO assemblies (a) before APPJ treatment and (b) after APPJ treatment for 1 h at a helium flow rate of 1.62 L/min and a working distance of 2 cm.

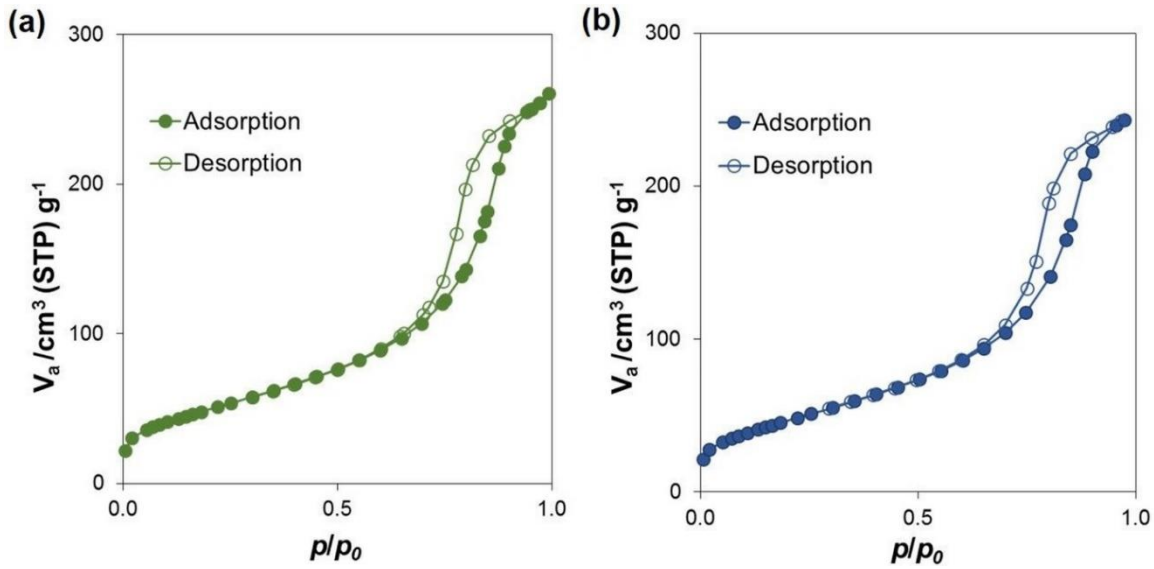

Figure 3-9. N_2 adsorption/desorption isotherms of solid TiO_2 MARIMO assemblies (a) before APPJ treatment and (b) after APPJ treatment for 1 h at a helium flow rate of 1.62 L/min and a working distance of 2 cm.

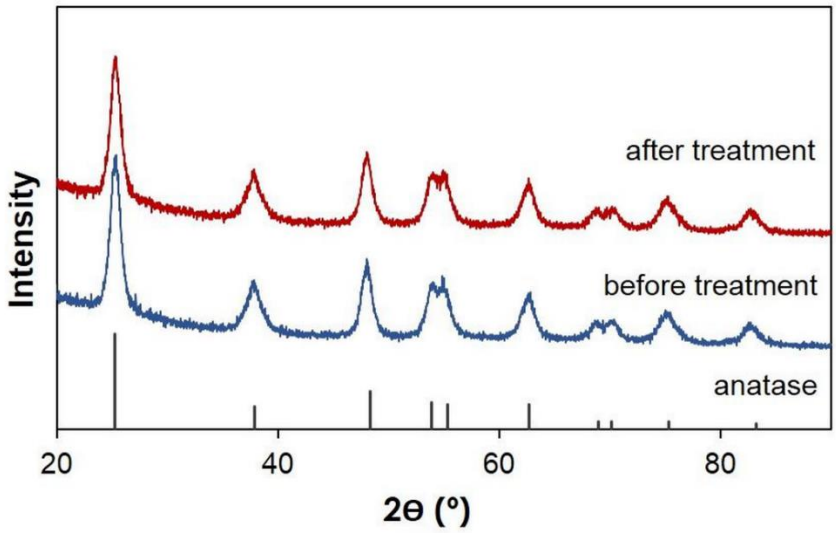

Figure 3-10. X-ray diffraction patterns of solid TiO_2 MARIMO assemblies before and after APPJ treatment for 1 h at helium flow rate of 1.62 L/min and a working distance of 2 cm.

The X-ray diffraction patterns shown in Figure 3-10 clearly indicate that there were no significant change in the crystal structure of the anatase TiO_2 after the APPJ treatment of the TiO_2 MARIMO assemblies. Thus, the APPJ treatment sufficiently removed the surface contaminants from the TiO_2 MARIMO assemblies without damaging the surface morphologies or crystal structures of the assemblies.

Another example of porous spherical nanoparticles, commercially available SiO_2, was also treated with the helium APPJ. Mass spectra of the SiO_2 spherical nanoparticles after the APPJ treatment clearly show the complete removal of contaminants (Figure 3-11) without any change in the morphology according to SEM images (Figure 3-12). In addition, similar results shown in Figures 3-13 and 3-14 confirm the ability of the plasma treatment to be used without damage on fragile cheek-brush and urchin-like structures of TiO_2 assemblies obtained by similar methods to the synthesis of TiO_2 MARIMO assemblies.[35] As a result, the non-thermal helium APPJ can be seen to be one of the best techniques for cleaning the surfaces of nanomaterials without structural damage.

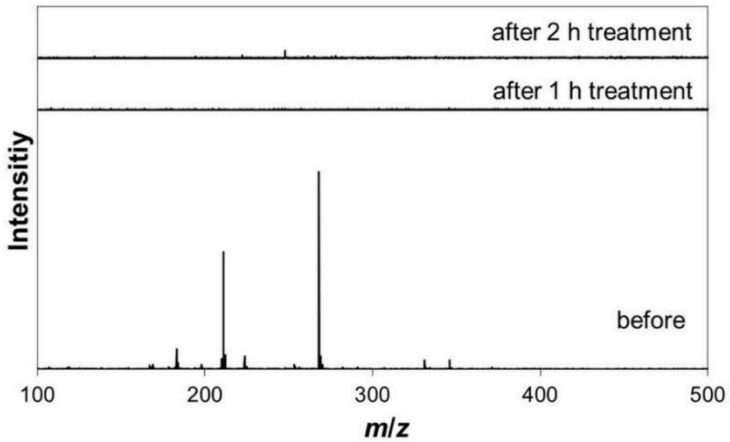

Figure 3-11. Mass spectrum of commercial SiO_2 nanoparticles before APPJ treatment compared with those obtained after APPJ treatment for 1 h and 2 h.

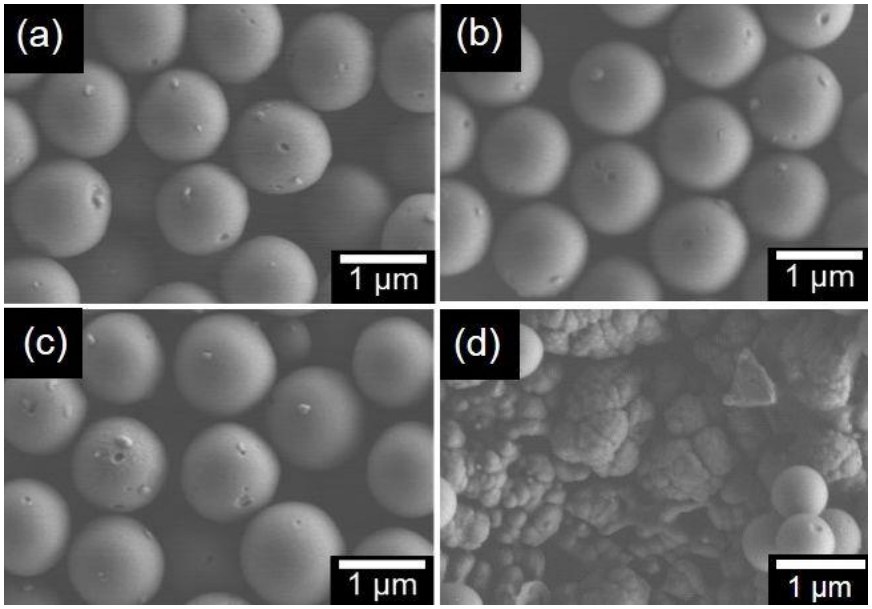

Figure 3-12. SEM images of commercial SiO_2 nanoparticles (a) before APPJ treatment, after APPJ treatment at a helium flow rate of 1.62 L/min and a 2 cm for (b) 1 h and (c) 2 h, and (d) with a working distance of 1 cm for 1 h.

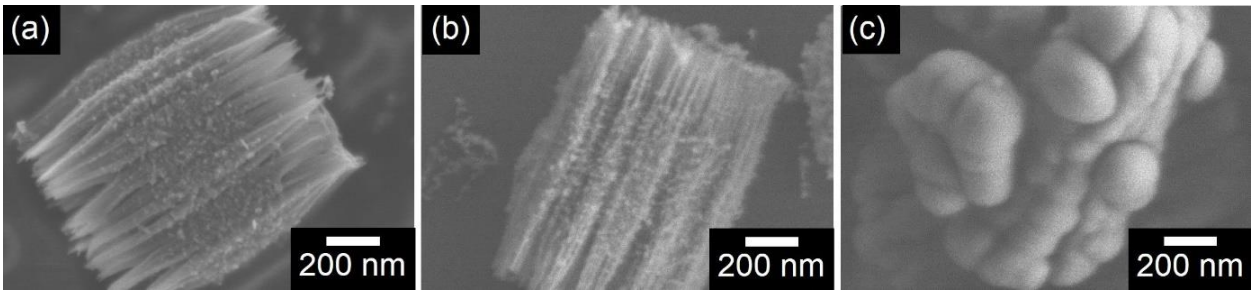

Figure 3-13. SEM images of cheek-brush TiO_2 assemblies (a) without APPJ treatment and after APPJ treatment at a helium flow rate of 1.62 L/min for (b) 1 h at a working distance of 2 cm and (c) 20 min at a working distance of 1 cm.

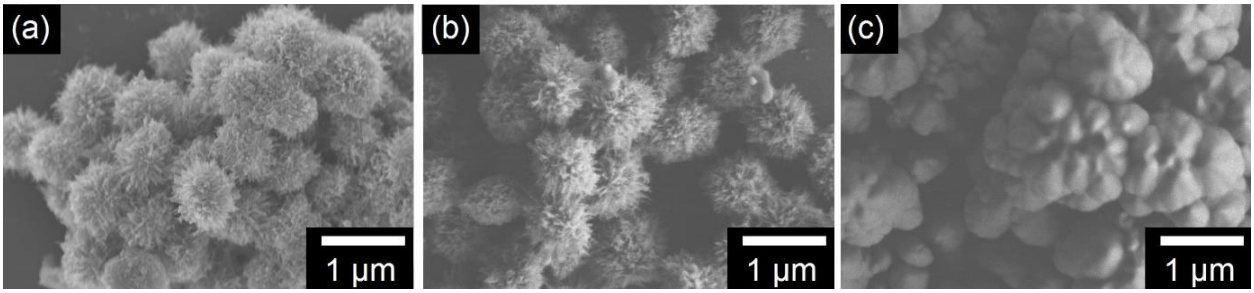

Figure 3-14. SEM images of urchin-like TiO_2 assemblies (a) without APPJ treatment and after APPJ treatment at a helium flow rate of 1.62 L/min for (b) 1 h at a working distance of 2 cm and (c) 20 min at a working distance of 1 cm.

3.3.3 Photocatalytic activity enhancement by plasma treatment

3.3.3.1 Photocatalytic degradation of methylene blue

The effect of the helium APPJ treatment on the photocatalytic activity of the TiO_2 MARIMO assemblies was studied through the photocatalytic degradation of methylene blue under UV irradiation as a model reaction (Figure 3-15a). When aqueous solutions of methylene blue were photoirradiated in the presence of catalysts, the APPJ-treated TiO_2 MARIMO assemblies performed far better catalytic ability, enabling faster degradation of methylene blue (78% decrease in 1 h) than seen for the as-prepared assemblies (34% decrease in 1 h). Based on the changes in absorbance over time, a pseudo-first-order kinetics model was applied to obtain rate constants (k) (Figure 3-15b). The calculated rate constants significantly increased from 8.3×10^{-3} min^{-1} for the as-prepared TiO_2 MARIMO assemblies to 3.2×10^{-2} min^{-1} for the APPJ-treated ones. Thus, photocatalytic activity was

accelerated 3.8 times by the simple APPJ treatment. Similar results were observed in the case of hollow MARIMO TiO_2 (Appendix B).

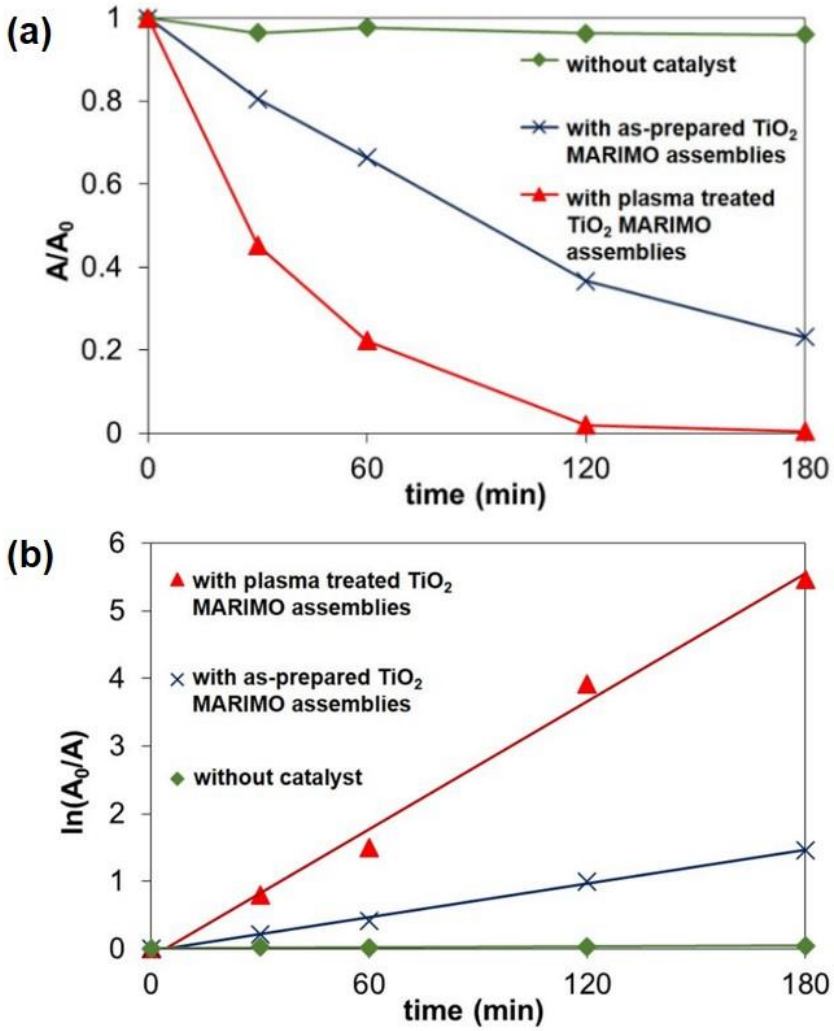

Figure 3-15 Photocatalytic degradation of methylene blue using as-prepared and APPJ-treated TiO_2 MARIMO assemblies (a), and its logarithmic plot (b).

3.3.3.2 Transient photocurrent responses

Transient photocurrent response measurements were also performed as another method evaluating the effect of surface activation by the APPJ treatment on the photocatalytic activity. Here, a standard three-component photoelectrochemical cell composed of working, reference, and Pt electrodes was used. The photocurrent responses of the as-prepared and the APPJ-treated TiO_2 MARIMO assemblies were recorded over several on-off cycles of UV irradiation. During UV irradiation, TiO_2 produces electrons and holes, with the separation efficiency of these playing a major role in the photocatalytic reaction. Thus, a higher photocurrent indicates a better catalytic activity derived from more efficient separation of electrons and holes.[42]

In Figure 3-16, the measured photocurrent of the APPJ-treated TiO_2 MARIMO assemblies was significantly higher than that of those without treatment. For the first cycle, the APPJ treatment led to an almost 100% improvement in the activity of the TiO_2 MARIMO assemblies, confirming excellent surface activation after plasma treatment, which allowed higher electron-hole generation, separation, and transfer efficiencies. Even after several cycles, the plasma-treated samples still had activities that were around 50% higher than those of the as-prepared samples. Similar trends were also observed in the case of hollow MARIMO TiO_2 (Appendix B).

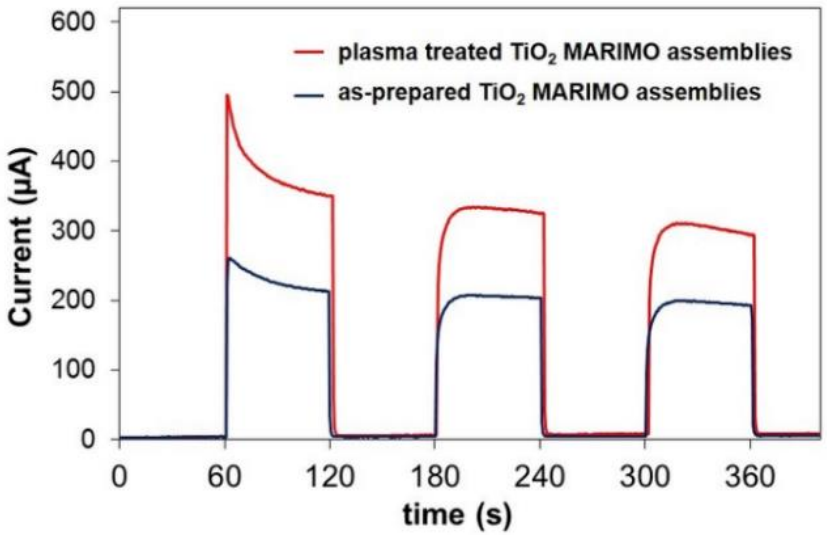

Figure 3-16. Transient photocurrent responses of as-prepared and APPJ-treated TiO_2 MARIMO assemblies.

3.4 Conclusions

In conclusion, facile treatment of porous nanomaterials by a non-thermal helium APPJ was developed to clean and activate the porous nanoparticle assembly surfaces without damaging their original surface morphologies and crystal structures. To ensure the cleanliness of the nanoparticle surfaces, a new technique for detecting trace amounts of contaminants on nanoparticles by LDI-TOF MS was developed. The non-thermal helium APPJ treatment enhanced the photocatalytic activity of the TiO_2 MARIMO assemblies, as confirmed through methylene blue degradation and transient photocurrent measurements under UV irradiation. The non-thermal helium APPJ treatment is expected to become one of the standard methods for surface treatment of porous nanomaterials with fragile structures.

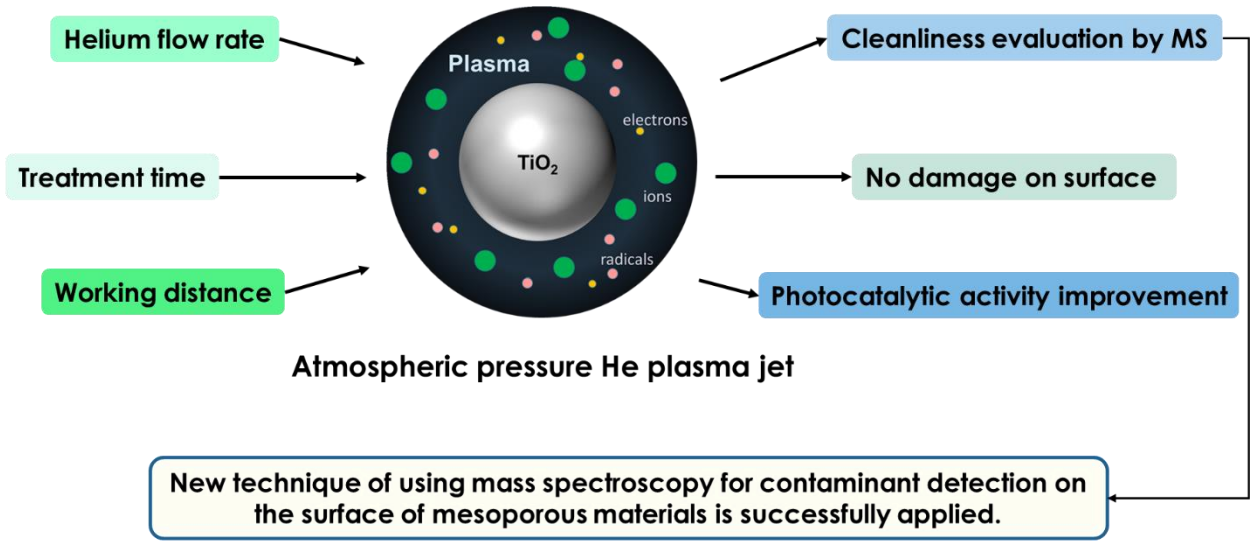

Figure 3-17. Illustration of the conclusions for APPJ treatment of TiO_2 MARIMO assemblies.

References

[1] Biener J., Wittstock A., Baumann T. F., Weissmuller J., Baumer M., and Hamza A. V. Surface Chemistry in Nanoscale Materials, *Materials* **2009**, 2, 2404-2428.

[2] Nanda K. K., Meisels A., Kruis F. E., Fissan H., and Stappert S. Higher Surface Energy of Free Nanoparticles, *Phys. Rev. Lett*. **2003**, 91, 1-4.

[3] Qi W. H., and Wang M. P. Size and shape dependent lattice parameters of metallic nanoparticles, *J. Nanopart. Res*. **2005**, 7, 51-57.

[4] Dabek L. Removal of Adsorbed Organic Impurities from Surface of Spent Catalysts Pd/Activated Carbons, *Adsorption* **2005**, 11, 781-785.

[5] Medina-Juarez O., Garcia-Sanchez M. A., Arellano-Sanchez U., Kornhauser-Straus I., and Rojas-Gonzalez F. Optimal Surface Amino-Functionalization Following Thermo-Alkaline Treatment of Nanostructured Silica Adsorbents for Enhanced CO_2 Adsorption, *Materials* **2016**, 9, 1-24.

[6] Naresh N., Wasim F. G. S., Ladewig B. P., and Neergat M. Removal of surfactant and capping agent from Pd nanocubes (Pd-NCs) using tert-butylamine: its effect on electrochemical characteristics, *J. Mater. Chem. A* **2013**, 1, 8553-8559.

[7] Sun T., Blanchard P. Y., and Mirkin M. V. Cleaning Nanoelectrodes with Air Plasma, *Anal. Chem*. **2015**, 87, 4092-4095.

[8] Teramoto Y., Shiono T., Ono R., and Oda T. Surface Treatment of TiO_2 Electrode for Dye-Sensitized Solar Cells Using Low-Temperature and Low-Energy Dielectric Barrier Discharge in Air, *Jpn. J. Appl. Phys*. **2011**, 50, 1-4.

[9] Colon G., Sanchez-Espana J. M., Hidalgo M. C., and Navio J. A. Effect of TiO_2 acidic pre-treatment on the photocatalytic properties for phenol degradation, *J. Photochem. Photobiol. A* **2006**, 179, 20-27.

[10] Fadoni M., and Lucarelli L., in Surface Science and Catalysis, Vol. 120, ed. A. Dabrowski, Elsevier Science B.V., Amsterdam, Netherlands, **1999**, pp. 177-225.

[11] Vig J. R., and Bus J. W. UV/Ozone Cleaning of Surfaces, *IEEE Trans. Parts, Hybrids, Packag.* **1976**, 4, 365-370.

[12] Hook A. A., Ohlhausen J. A., Krim J., and Dugger M. T. Evaluation of Oxygen Plasma and UV Ozone Methods for Cleaning of Occluded Areas in MEMS Devices, *J. Microelectromech. Syst.* **2010**, 19, 1292-1298.

[13] Huang H., and Tang L. Treatment of organic waste using thermal plasma pyrolysis technology, *Energy Convers. Manage*. **2007**, 48, 1331-1337.

[14] Boulos M. I. Thermal plasma processing, *IEEE Trans. Plasma Sci.* **1991**, 19, 1078-1089.

[15] Grill A., Cold Plasma Materials Fabrication: From Fundamentals to Applications, Wiley-IEEE Press, New York, United States **1994**, pp.151-179.

[16] Lieberman M. A., and Lichtenberg A. J., Principles of Plasma Discharges and Materials Processing, Second Edition, John Wiley & Sons, Inc., New Jersey, United States **2005**, p. 20.

[17] Weiss M., Gumbel D., Hanschmann E. M., Mandelkow R., Gelbrich N., Zimmermann U., Walther R., Ekkernkamp A., Sckell A., Kramer A., Burchardt M., Lillig C. H., and Stope M. B. Prediction formulas for individual opioid analgesic requirements based on genetic polymorphism analyses., *PLoS One* **2015**, 10, 1-17.

[18] Kim W., Woo K. C., Kim G. C., and Kim K. T. Nonthermal-plasma-mediated animal cell death, *J. Phys. D: Appl. Phys*. **2011**, 44, 013001.

[19] Li L., Li J., Shen M., Zhang C., and Dong Y. Cold plasma treatment enhances oilseed rape seed germination under drought stress, *Sci. Rep*. **2015**, 5, 13033.

[20] Jiang J., Lu Y., Li J., Li L., He X., Shao H., and Dong Y. Effect of seed treatment by cold plasma on the resistance of tomato to Ralstonia solanacearum (Bacterial Wilt), *PLoS One* **2014**, 9, 1-6.

[21] Oh J.-S., Kakuta Y., Yasuoka Y., Furuta H., and Hatta A. Localized DLC etching by a non-thermal atmospheric-pressure helium plasma jet in ambient air, *Diamond Relat. Mater*. **2014**, 50, 91-96.

[22] Oh J.-S., Furuta H., Hatta A., and Bradley W. Investigating the effect of additional gases in an atmospheric-pressure helium plasma jet using ambient mass spectrometry, *Jpn. J. Appl. Phys.* **2015**, 54, 1-5.

[23] Oh J.-S., Olabanji O. T., Hale C., Mariani R., Kontis K., and Bradley J. W. Imaging gas and plasma interactions in the surface-chemical modification of polymers using micro-plasma jets, *J. Phys. D: Appl. Phys*. **2011**, 44, 155206.

[24] Bradley J. W., Oh J.-S., Olabanji O. T., Hale C., Mariani R., and Kontis K. Schlieren Photography of the Outflow From a Plasma Jet, *IEEE Trans. Plasma Sci.* **2011**, 39, 2312-2313.

[25] Oh J.-S., Aranda-Gonzalvo Y., and Bradley J. W. Time-resolved mass spectroscopic studies of an atmospheric-pressure helium microplasma jet, *J. Phys. D: Appl. Phys*. **2011**, 44, 365202.

[26] McKay K., Oh J.-S., Walsh J. L., and Bradley J. W. Mass spectrometric diagnosis of an atmospheric pressure helium microplasma jet, *J. Phys. D: Appl. Phys*. **2013**, 46, 464018.

[27] Tachibana K. Current status of microplasma research, *IEEJ Trans Electr. Electron. Eng*. **2006**, 1, 145-155.

[28] Oh J.-S., Kakuta M., Furuta H., Akatsuka H., and Hatta A. Effect of plasma jet diameter on the efficiency of reactive oxygen and nitrogen species generation in water, *Jpn. J. Appl. Phys*. **2016**, 55, 06HD01.

[29] Oh J.-S., Szili E. J., Gaur N., Hong S.-H., Furuta H., Kurita H., Mizuno A., Hatta A., and Short R. D. How to assess the plasma delivery of RONS into tissue fluid and tissue, *J. Phys. D: Appl. Phys*. **2016**, 49, 304005.

[30] Thevenet F., Sivachandiran L., Guaitella O., Baraket C., and Rousseau A. Plasma–catalyst coupling for volatile organic compound removal and indoor air treatment: a review, *J. Phys. D: Apply. Phys.* **2014**, 47, 1-14.

[31] Kim H. H., Tsubota S., Date M., Ogata A., and Futamura S. Catalyst regeneration and activity enhancement of Au/TiO_2 by atmospheric pressure nonthermal plasma, *Appl. Cat. A* **2007**, 329, 93-98.

[32] Mahmood A., and Woo S. I. Enhancement of catalytic activity of Au/TiO2 by thermal and plasma treatment, *Korean J. Chem. Eng*. **2013**, 30, 1876-1881.

[33] Fujishima A., and Honda K. Electrochemical Photolysis of Water at a Semiconductor Electrode, *Nature* **1972**, 238, 37-38.

[34] Wang P., Ueno K., Takigawa H., and Kobiro K. Versatility of one-pot, single-step synthetic approach for spherical porous (metal) oxide nanoparticles using supercritical alcohols, *J. Supercrit. Fluids* **2013**, 78, 124-131.

[35] Duriyasart F., Hamauzu H., Ohtani M., and Kobiro K. Three-Dimensionally Branched Titanium Dioxide with Cheek-Brush Morphology: Synthesis and its Application to Polymer Composites, *ChemistrySelect* **2016**, 1, 5121-5128.

[36] Kitano K., Hamaguchi S., and Aoki H., US Pat., 8232729 B2, **2012**.

[37] Li C., Sun Z., Xue Y., Yao G., and Zheng S. A facile synthesis of g-C_3N_4/TiO_2 hybrid photocatalysts by sol–gel method and its enhanced photodegradation towards methylene blue under visible light, *Adv. Powder Technol*. **2016**, 27, 330-337.

[38] Bardosh L., and Lebedev Y. A. Spherical microwave electrode discharge. Phenomenology and results of probe measurements, *Tech. Phys*. **1998**, 43, 1428-1431.

[39] Karas M., and Hillenkamp F. Laser desorption ionization of proteins with molecular masses exceeding 10,000 daltons, *Anal. Chem*. **1988**, 60, 2299-2301.

[40] Lo C. Y., Lin J. Y., Chen W. Y., Chen C. T., Chen Y. C. Surface-assisted laser desorption/ionization mass spectrometry on titania nanotube arrays, *J. Am. Soc. Mass Spectrom*. **2008**, 19, 1014-1020.

[41] Wang X., Dolocan A., Chou H., Tao L., Dick A., Akinwande D., and Wilson C. G. Direct Observation of Poly (Methyl Methacrylate) Removal from a Graphene Surface, *Chem. Mater*. **2017**, 2033-2039.

[42] Xiang Q., Yu J., and Jaroniec M. Preparation and Enhanced Visible-Light Photocatalytic H_2-Production Activity of Graphene/C_3N_4 Composites, *J. Phys. Chem. C* **2011**, 115, 7355-7363.

CHAPTER IV

High Surface Roughness of Mesoporous Spherical Nanoparticle Assembly of TiO_2 for Supporting Well-dispersed Au Nanoparticle

4.1 Introduction

Much attention has been paid to well-dispersed metal nanoparticles in many fields of physics, chemistry, materials science, and practical applications, including synthetic chemistry, energy-conversion, industrial mass production, environmental issues, and biomedical applications.[1-11] In order to obtain good dispersion of nanoparticles, surface of the metal nanoparticles are usually modified directly by mixing with organic materials or dispersion media, such as fatty acids with long alkyl chain and amine derivatives.[12-14] In the field of catalyst, the dispersion media are called "supports." There are many kinds materials for supports utilized in this field, such as active carbon, diatomite, zeolites, metal oxides, and metal-organic-frameworks.[15-21] Among them, metal oxides are considered to use commonly, since they can serve not only high heat tolerance and mechanical strength required for high temperature vapor phase reactions but also wide surface area. The larger surface area of the support is expected to dilute catalyst metals on the support surface, resulting in the better reaction heat release, especially in exothermic reaction. It is also believed that the metal oxide surface also affords electronic effect on their catalytic activity of supported metal nanoparticles. Thus, rational combination of catalyst nanoparticles and supports is the most important for the high performance catalysts.

In the case of exothermic reactions, the temperature of catalysts, especially very surface of the catalysts, becomes notably high. Under such high temperature conditions, one of the most serious problems is catalyst sintering, because of which several catalyst nanoparticles migrate and agglomerate to form large particles leading to the loss of catalyst surface area at the elevated temperature (Figure 4-1).[22-26] Ablation of the nanoparticles from the support surface, so called leaching, is another common problem that shortens the catalyst life-time. Generally, once the catalyst nanoparticles are sintered or leached, they do not reproduce the original sizes, morphology, surface area, and crystal structure. Thus, it is better to focus on the prevention of sintering and leaching rather than regenerate the nanoparticles.

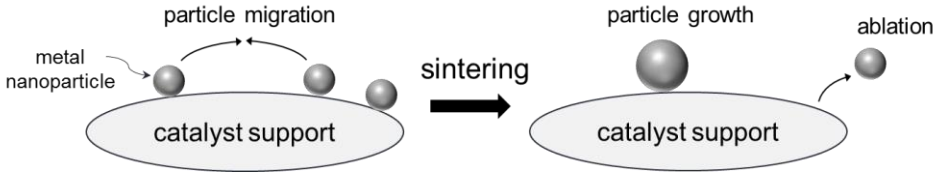

Figure 4-1. Illustration of sintering of metal catalyst at high temperature and ablation.

To prevent the sintering and leaching of metal nanoparticles, several methods such as alloying, ligand-assisted pinning, fixation on defects, and encapsulation as core-shell/sheath structures by oxides or polymer coatings are reported (Figure 4-2).[27-37] Those strategies mainly focus on the isolation of the individual nanocatalyst resulting in low possibility of catalyst aggregation/growth. However, some of them limit the accessibility of reactant to the active site of the catalyst, which affect the reaction rate. Beside, most of their preparation methods are usually complex and multi-steps reactions are required.

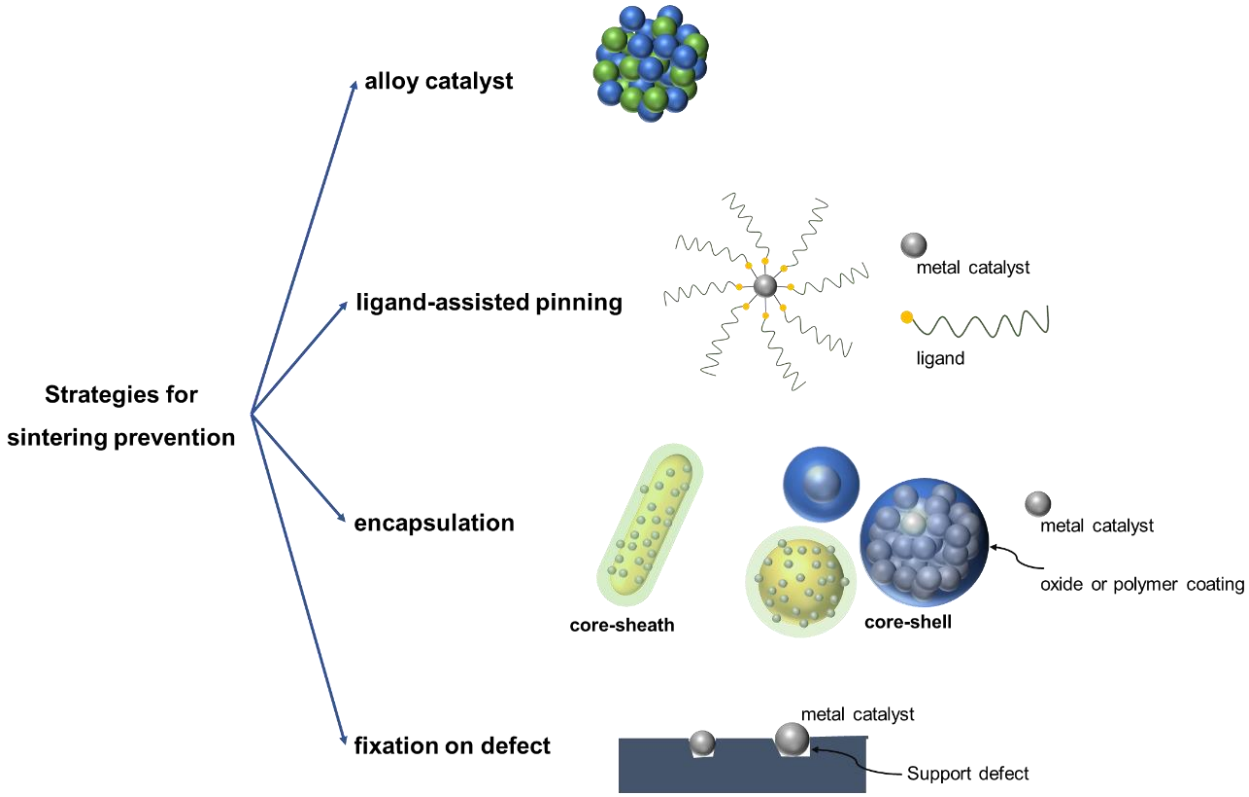

Figure 4-2. Schematic representations of example methods for catalyst sintering prevention.

At the same time, the simple one-pot and single-step solvothermal approach has been reported to fabricate solid and hollow TiO_2 nanoparticle assemblies with fine primary particles (< 5 nm) and large surface area (200-400 m^2/g) (Figure 4-3).[38] The assemblies with mesoporous morphologies are called **m**icro/**m**eso-porously **a**rchitected **r**oundly **i**ntegrated **m**etal **o**xides (MARIMOs). They have a unique surface roughness derived from their inherent fine primary particles, which are expected to disperse metal nanoparticles well and lead to larger amounts of metal nanoparticles loading onto their surface.

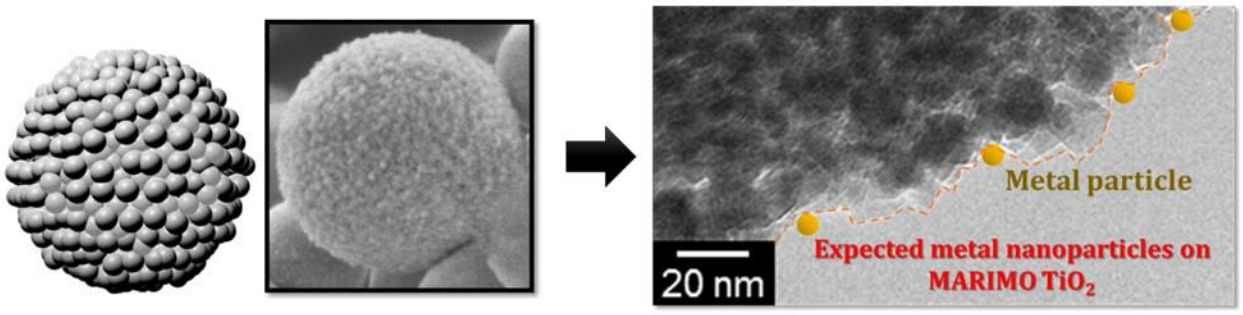

Figure 4-3. MARIMO TiO_2 with its unique surface as an effective support for metal nanoparticle.

A preliminary result was reported on a completely new approach to suppress sintering of metal nanoparticles supported on TiO_2 support.[39] It is stated that nano-concave-convex structure on the surface of the MARIMO TiO_2 nanoparticle assemblies prevented the migration of metal nanoparticles even at high temperature (Figure 4-4a) and steric bulkiness derives from the concave-convex nanostructure suppressed the fusion of several embedded nanoparticles by the difficulties of contacting between each nanoparticle. In this year (February, 2017), Liu et al reported the similar concept on the suppression of sintering using "silica" support with wide mouthed compartments.[22] They demonstrated sintering-resistance of Pt nanocatalysts on silica nanosheets. The nanosheets have special three-dimensional assemble structure consisting of large amount of compartments, which effectively separated each catalyst to stay in each large spaces. According to the significant long distance between each catalyst, it is difficult for them to travel across the wall and aggregate together. Furthermore, reactant gases can easily access to the catalyst due to their wide mouthed structure. However, amount of catalyst metal nanoparticles on the support should be not so much to keep the nanoparticles independent.

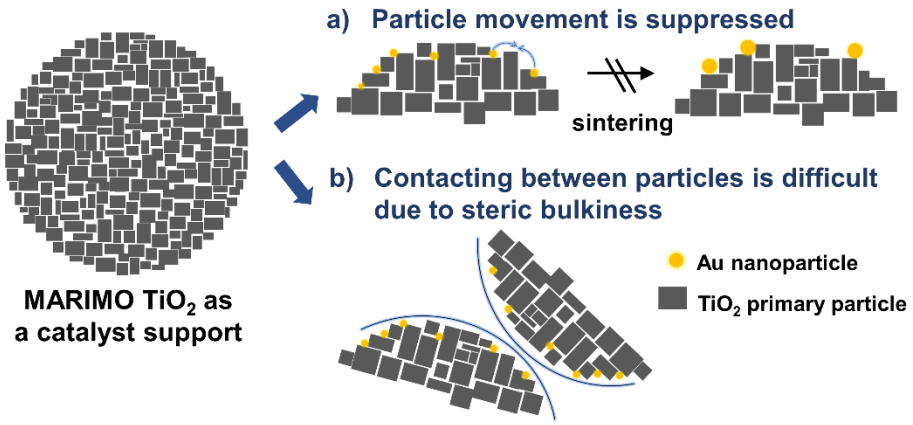

Figure 4-4. Supposed mechanisms of the sintering prevention by using rough surface support for metal nanoparticle.

In this chapter, a new strategy for sintering delay and resistance of catalysts by using a new type of TiO_2 catalyst support, with a concave-convex structure and high surface roughness at the nanometer level owing to systematic agglomeration of TiO_2 ultrafine primary particles, is proposed. This chapter reports good dispersion ability of metal nanoparticles onto the nano-concave-convex surface of TiO_2 MARIMO nanoparticle assemblies even by the use of common loading method without any special technique. Au is also chosen as the catalyst metal, since it can be sintered easily at high temperature. [40] A highly exothermic CO oxidation (283 kJ/mol) is also selected as a probe reaction operated at high temperatures.[41] The deposition-precipitation method reported by Haruta et al. is adopted to prepare TiO_2 supported Au catalysts.[42]

4.2 Experimental Section

4.2.1 Materials

Methanol, titanium tetraisopropoxide, formic acid, chloroauric acid ($HAuCl_4 \cdot 4H_2O$), and sea sand (300-600 μm, 30-50 mesh) were purchased from the Wako Pure Chemical Industries Co., Ltd. MARIMO TiO_2 nanoparticle assemblies were received from UJIDEN Chemical Industry Co., Ltd. P25 (non-porous mixed anatase-rutile phase with surface area around 50 m^2/g TiO_2 nanoparticles) and ST-01 (anatase phase with high surface area of around 300 m^2/g TiO_2 nanoparticles) were received from Evonik Industries and Ishihara Sangyo Kaisha, Ltd., respectively. All chemicals were used as received without further treatment. Reverse osmosis water was used throughout the experiments.

4.2.2 Au/TiO_2 catalyst preparation

Au/TiO_2 catalysts with 1wt% and 5wt% Au amounts were prepared by common deposition-precipitation method using 2 mg and 10 mg of chloroauric acid ($HAuCl_4 \cdot 4H_2O$), respectively. pH values of aqueous solutions of chloroauric acid in 20 mL water were adjusted to 8.0 by addition of 1.0 mol/L NaOH solution. TiO_2 support (100 g) was then added to the solution. The mixture was sonicated for 10 min and stand at 70 °C for 1 h. After cooling to room temperature, the mixture was washed with water and the suspension was centrifuged. The obtained solid was dried *in vacuo* at room temperature for 12 h and calcined in air at 300 °C for 4 h.

4.2.3 Catalyst characterizations

The catalyst morphologies were observed by scanning electron microscope (FE-SEM, Hitachi S8020) and transmission electron microscope (TEM, JEOL JEM-2100F). Energy dispersive X-ray spectroscopy was performed on Oxford INCA Energy TEM250 attached on the TEM for elemental analysis of the catalysts. Power X-ray diffraction (XRD) pattern was obtained on Rigaku SmartLab (Cu Kα radiation, DteX-25 detector).

4.2.4 CO pulse adsorption

The adsorption process was performed at 0 °C in a flow type reactor, BELCATII (Microtrac BEL Corp.) with TCD detector. A catalyst loading of 50 mg was fixed in a quartz tube fixed bed reactor using quartz wool on both sides. Before CO adsorption, the following pretreatment method was applied: The sample was heated to 40 °C by He gas flow for 15 min, followed by 15 min O_2, 20 min He, and 20 min H_2 treatments to completely reduce the metal catalyst. Then, He was flowed again to cool the catalyst to the desired adsorption temperature (0 °C) obtained by liquid nitrogen in cryo unit equipped with the reactor. Total gas flow rate was kept constant at 50 mL/min during the pretreatment. 10% CO content in He (*v*/*v*) was applied to the CO pulse adsorption with pulse size of 0.88 mL, with 5 min interval time.

4.2.5 Catalytic activity test

CO oxidation for catalytic activity study was carried out using a flow-type reactor (BELCATII, MicrotracBEL Corp.). A 20 mg of sample containing 5 mg of Au/TiO_2 catalyst dispersed in 15 mg of sea sand was placed in the fixed bed reactor stuffed by quartz wool on both sides. The sample was pretreated at 40 °C by flowing He for 35 min, followed by 15 min of O_2, 20 min of He again, 20 min of H_2, and 10 min of Ar with the constant gas flow rate of 50 mL/min. After the pretreatment, the reactant mixture gas $CO/O_2/Ar$ (13.3% CO, 6.7% O_2, and balance Ar) was fed through the catalyst bed at a flow rate of 30 mL/min. The reaction temperature was controlled by blowing liquid N_2 and/or heating the reactor. The outlet gases were analyzed by GC3200 gas chromatograph (GL Science) using a TCD detector. The cycle test was performed by repeating the reactions at the low and high temperatures alternatively for 10 cycles under the same reaction conditions, while only Ar gas was flowed during the cooling and heating steps.

4.3 Results and Discussion

4.3.1. Dispersion of metal catalyst on the support

There are several methods for sintering prevention by fixing metal nanoparticles on metal oxide supports (Figure 4-2), which include conventional impregnation, coprecipitation, deposition-precipitation, colloidal deposition, arc plasma deposition, mechanical mixing, sputtering, and grafting.[43] The selection of suitable method is crucial to obtain well-dispersed with uniform size metal catalyst on support material's surface since the dispersion ability and particle size of metal nanoparticles as well as durability of the metal support catalysts directly influence the catalysts performance. In this experiment, the conventional deposition-precipitation method reported by Haruta et al. is selected to obtain TiO_2 supported Au catalysts.[42] MARIMO TiO_2 nanoparticle assemblies were dispersed into chloroauric acid solution, whose pH was adjusted to 8.0 with NaOH solution. The obtained solid was washed by water and calcined in air at 300 °C for 4h. The catalyst products are called 1-Au/MARIMO and 5-Au/MARIMO; the numbers denote wt% of Au in the precursor mixtures of chloroauric acid and TiO_2 nanoparticle assemblies. As a control, commercially available Degussa P25 TiO_2 particles having an anatase-rutile mixed phase with the particle size of *ca.* 25 nm and without any porous structure were used. The obtained catalysts are denoted as 1-Au/P25 and 5-Au/P25, respectively. Ishihara Sangyo Kaisha ST-01 TiO_2 powder with an anatase phase having particles of ca. 7 nm and specific surface area of ca. 300 m^2/g was also utilized as the reference catalyst support. The obtained catalysts are denoted as 1-Au/ST-01 and 5-Au/ST-01, respectively (Table 4-1).

Table 4-1. Information of Au/TiO_2 catalysts.

Sample name	Support	Au in precursor solution (wt%)	Au content by EDX (wt%)	After cycle test (wt%)	After CO oxidation at 400 °C (wt%)
1-Au/MARIMO	MARIMO TiO_2	1	2.0	1.9	2.0
5-Au/MARIMO	MARIMO TiO_2	5	6.2	6.1	6.3
1-Au/ST01	ST-01 TiO_2	1	1.8	1.0	1.6
5-Au/ST01	ST-01 TiO_2	5	7.6	6.8	8.3
1-Au/P25	P25	1	0.0	-	0.3
5-Au/P25	P25	5	4.4	2.3	3.3
WGC Au/TiO_2*	-	-	1.8	1.8	1.7

*A commercially available Au/TiO_2 catalyst

In order to see Au nanoparticles on the MARIMO TiO_2 support surface, TEM and HAADF-STEM observations were performed. Unfortunately, direct observation of Au NPs was not successful (Figure 4-5), which can be ascribed to the resolution limit of TEM and HAADF-STEM instruments. However, the existence of Au atoms on MARIMO TiO_2 supports was directly and clearly confirmed by STEM/EDX analysis (Figure 4-6a, b). In addition, Au NPs were perfectly dispersed on MARIMO TiO_2, irrespective of Au contents of 1 and 5wt% (Figure 4-6a, b). Au/ST-01 also exhibits quite good dispersion ability of Au on TiO_2 support, however, several aggregation of Au clusters were observed in its HAADF-STEM/EDX and STEM/EDX analyses (Figures 4-6c, d, 4-7). Similar aggregation of Au clusters was observed in the case of Au/P25 (Figure 4-6f).

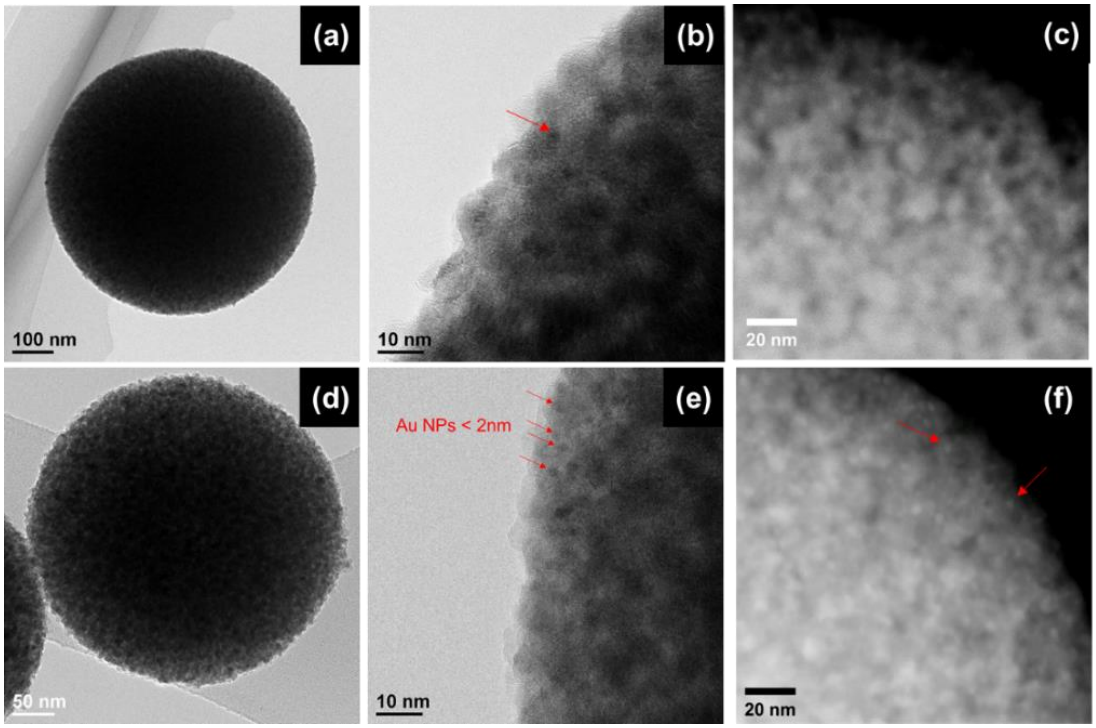

Figure 4-5. TEM and HAADF-STEM images of 1-Au/MARIMO (a-c) and 5-Au/MARIMO (d-e).

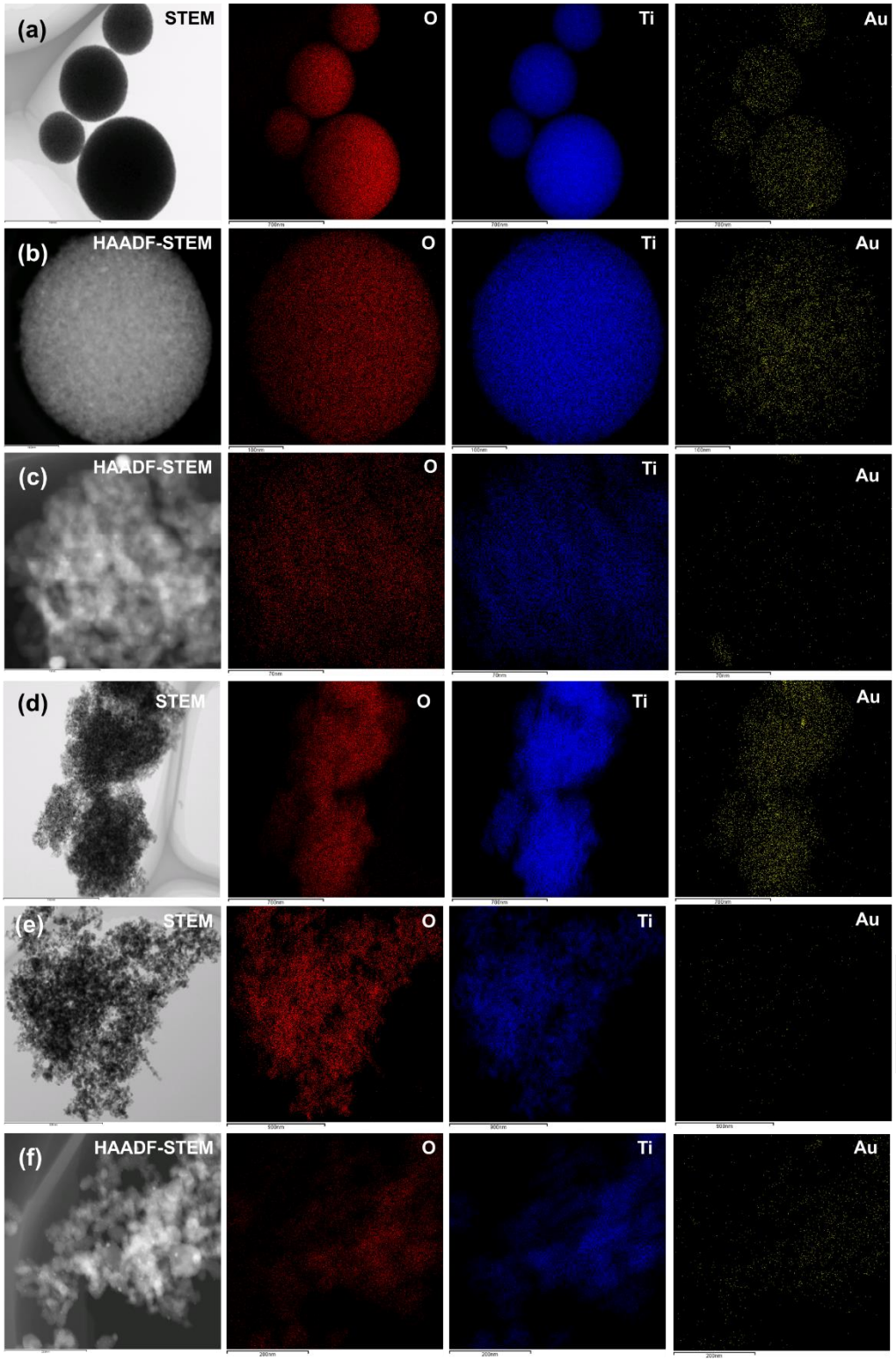

Figure 4-6. STEM, HAADF-STEM images, and EDX mappings of as–prepared catalysts.

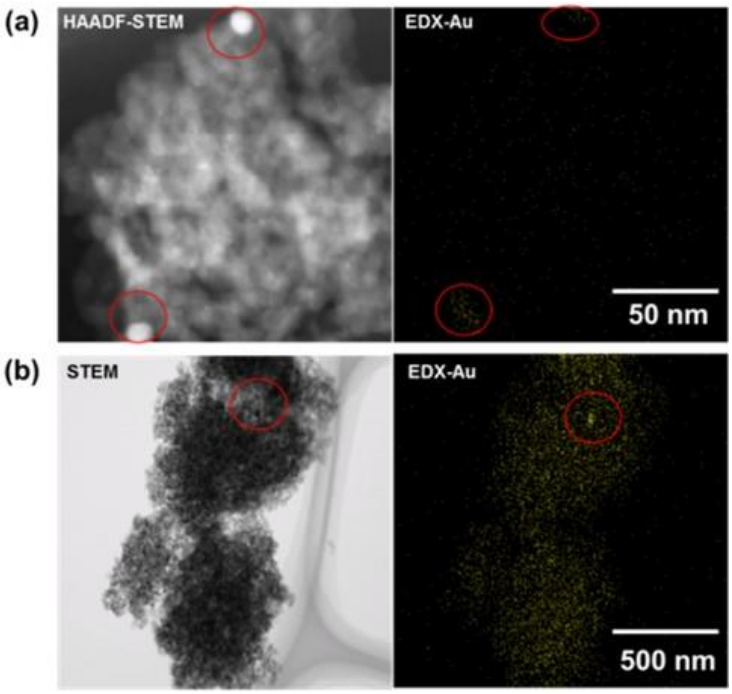

Figure 4-7. HAADF-STEM, STEM, and EDX mappings of 1-Au/ST01 (a) and 5-Au/ST01.

The amounts of Au atoms were estimated by STEM/EDX or HAADF-STEM/EDX analysis, as listed in Table 4-1. In the cases of MARIMO and ST-01 supports with a large specific surface area, Au contents increased a little bit as compared to those in the precursor solutions. In contrast, in the case of Au/P25 with a small specific surface area, the total amounts of Au loading were significantly lower than those in the precursor mixtures, which can be ascribed to the leaching of Au NPs from the surface of P25 during the washing process in the preparation of Au/P25 (Figure 4-6e, f). The obvious difference in the loading amount of Au clearly indicates that the wider surface area and/or the nanometer-scale surface concave-convex structure originated from their small primary particle size would catch and fix larger amounts of Au NPs on the surface, as illustrated in Figure 4-4a.

The measurements of CO pulse adsorption were also conducted to confirm the difference in dispersion ability of Au on MARIMO support comparing with P25 support. The CO pulse adsorption patterns show larger amount of CO adsorption on Au/MARIMO (0.31 cm^3[STP]/g) than that on Au/P25 (0.17 cm^3[STP]/g), clearly indicating the better dispersion ability of Au nanoparticles on MARIMO surface than that on P25 one (Figure 4-8).

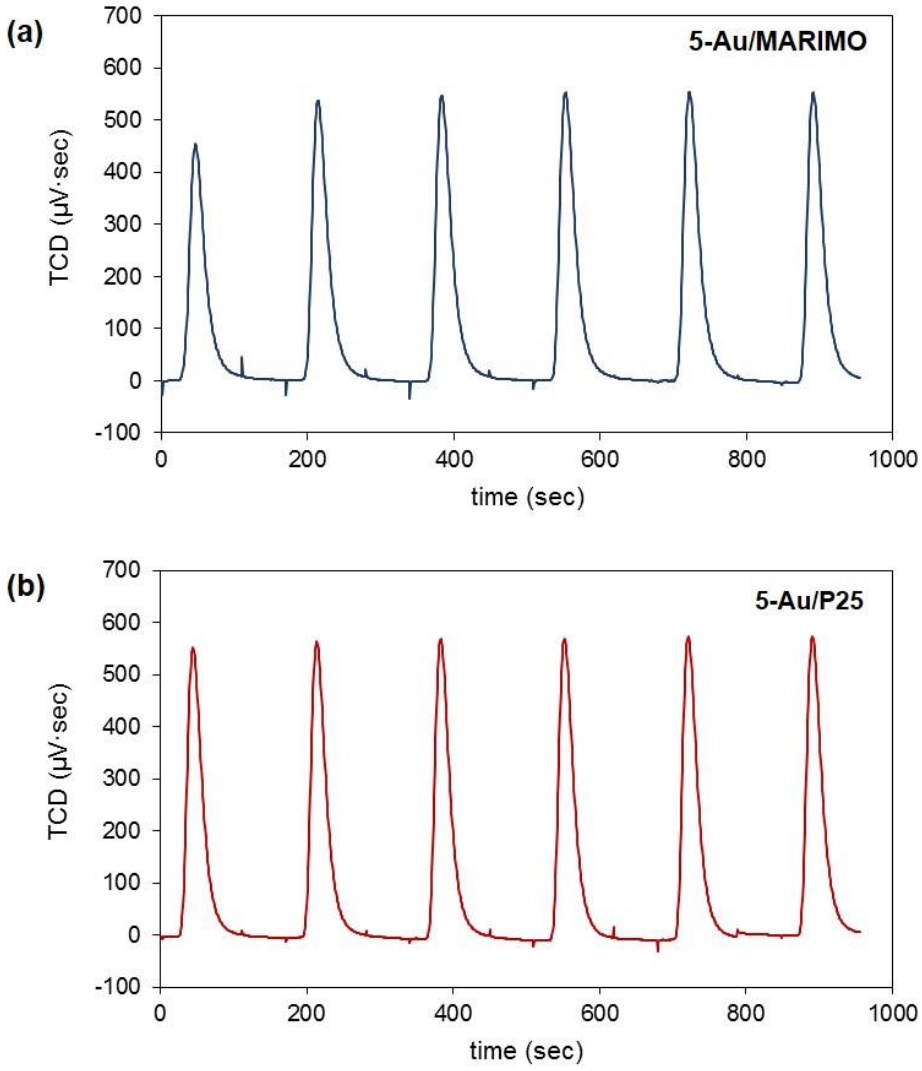

Figure 4-8. CO pulse adsorption patterns on Au/TiO_2 catalysts. (a) 5-Au/MARIMO and (b) 5-Au/P25.

Another method of XRD measurements were also employed for Au nanoparticle detections. X-ray diffraction patterns of Au/TiO_2 catalysts (Figures 4-9) have no discrepancy with the results of TEM observations. Anatase and/or rutile TiO_2 diffraction patterns were observed but not for Au crystal, indicating that crystal sizes of Au nanoparticles dispersed on the TiO_2 supports are too small to be observed.

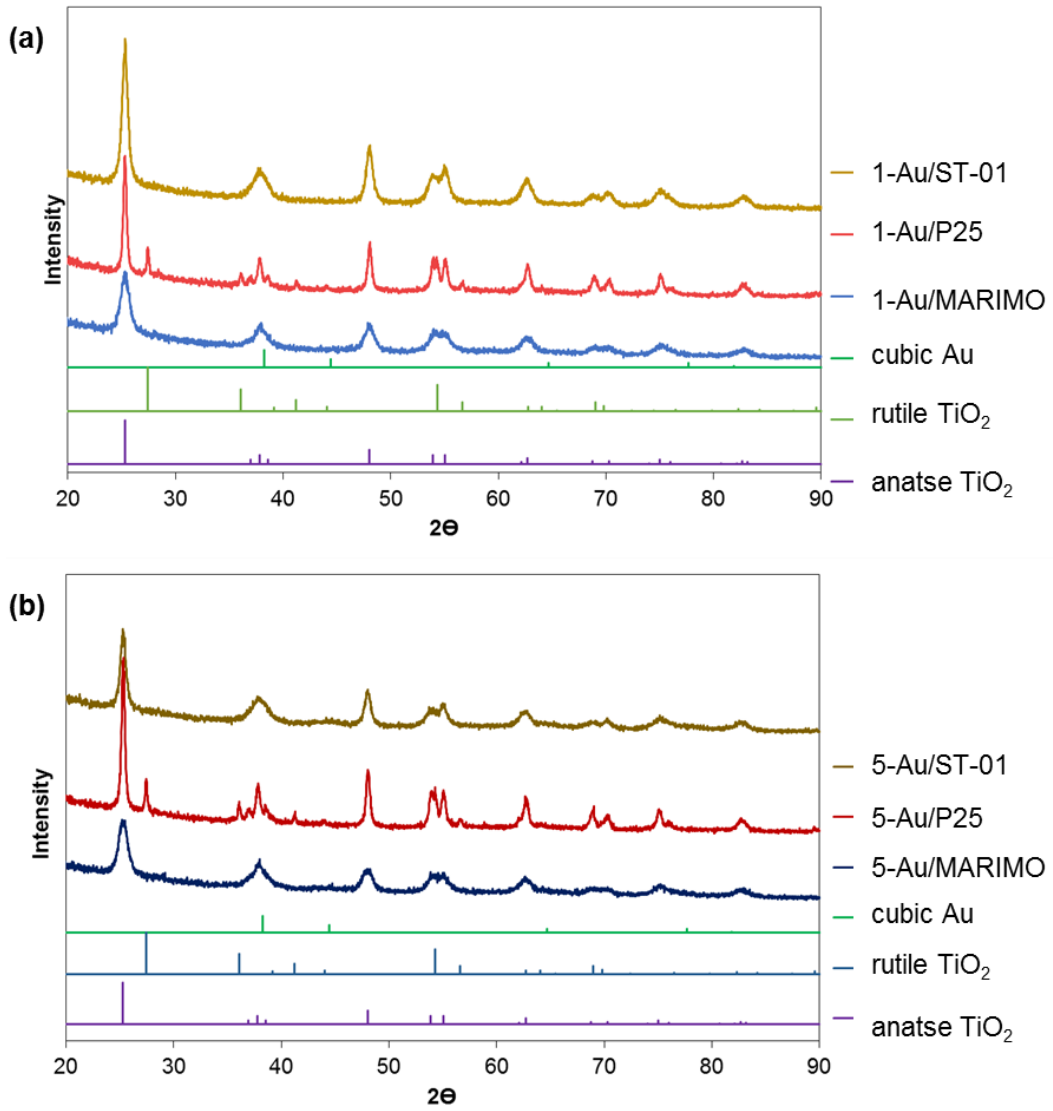

Figure 4-9. X-ray diffraction patterns of as-prepared 1wt% (a), and 5wt% (b) Au/TiO_2 catalysts.

4.3.2. Catalytic activity for CO oxidation

According to the small size and high loading content of Au nanoparticles as proved in section 4.3.1, Au/MARIMO TiO_2 is expected to exhibit higher catalytic activity for the probe reaction of CO oxidation. The results were more than expected (Figure 4-10a). When the temperature of the mixed reactant gas ($CO/O_2/Ar$) was increased to 60 °C, CO oxidation reaction suddenly occurred and the catalyst bed temperature increased to 80 °C, where CO conversion reached to 80%. When the catalyst temperature was increased to more than 80 °C, a gradual increasing in CO conversion was observed. However, when the reference catalyst 1-Au/ST-01 was used, the reaction started at a much higher temperature (120 °C) and only 65% of CO conversion was observed. In the case of 1-Au/P25, the reaction started at 150 °C, though CO conversion stayed at a low level of ca. 20%. Thus, the 1-Au/MARIMO catalyst showed a much better low-temperature activity as well as higher CO conversion, confirming the excellent ability of MARIMO structure as a support for catalytic reaction, as compared to those of the reference 1-Au/ST-01 and 1-Au/P25 catalysts. Similar trend was shown in 5wt% Au/TiO_2 (Figure 4-10b). The high amount of Au nanoparticles of more than 5wt% showed that the reaction required lower temperature of around room temperature compared to 1wt% Au loading.

In addition, low CO conversions were observed when 1-Au/P25 was used as a catalyst throughout all temperature ranges. On the other hand, although the total amounts of Au loading in 5-Au/P25 resulted in significantly lower than those of other kinds of supports (4.4wt% as shown in Figure 4-6f), CO oxidation occurred at as low temperature as in the case of MARIMO support (Figure 4-10b) which might be derived from anatase/rutile mixed crystalline structure of P25.

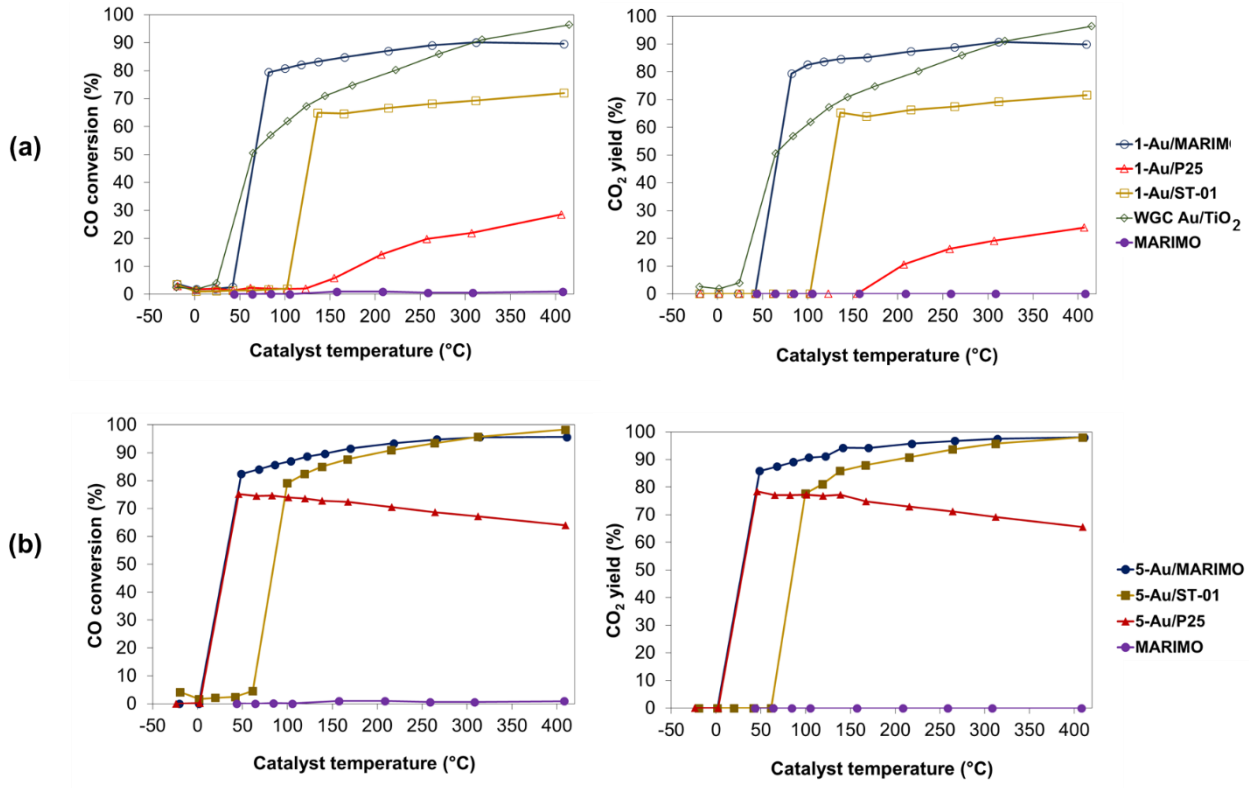

Figure 4-10. CO conversion and CO_2 yield from CO oxidation using different type of 1wt% (a), and 5wt% (b) Au/TiO_2 catalysts.

Also, the HAADF-STEM images and size distribution of Au nanoparticles (Figures 4-11b and 4-12) show small size of the Au catalyst of around 2-4 nm, which supports the occurrence of the reaction at comparatively low reaction temperature. However, the CO conversion in the case of 5-Au/P25 catalyst decreased gradually during the increase of reaction temperature, which can be explained by a hypothesis of which Au nanoparticles became aggregated and sintered on flat surface support comparing with high curvature surface support at high temperature. HAADF-STEM images of the catalysts after CO oxidation at 400 °C showed that sizes of Au particles on P25 and ST-01 TiO_2 supports (Figure 4-11e and 4-11f) were significantly increased as the size

distribution shown in Figure 4-12. Considering the MARIMO support, Au nanoparticles cannot be seen clearly due to the difficulty of the measurement on spherically aggregated nanoparticle assemblies as mentioned earlier. Nevertheless, there was no large particle found at the edge of the assembly (Figure 4-11d), which partially confirms no aggregation during CO oxidation at the temperature ranging from -20 °C to 400 °C. These results emphasized the importance of the MARIMO structure on their excellent ability for metal catalyst support. In addition, the 1-Au/MARIMO showed higher CO conversion at low temperature even comparing with the commercially available WGC reference Au/TiO_2 catalyst. So, the synthesized Au/MARIMO can be considered as an alternative choice for Au/TiO_2 catalyst.

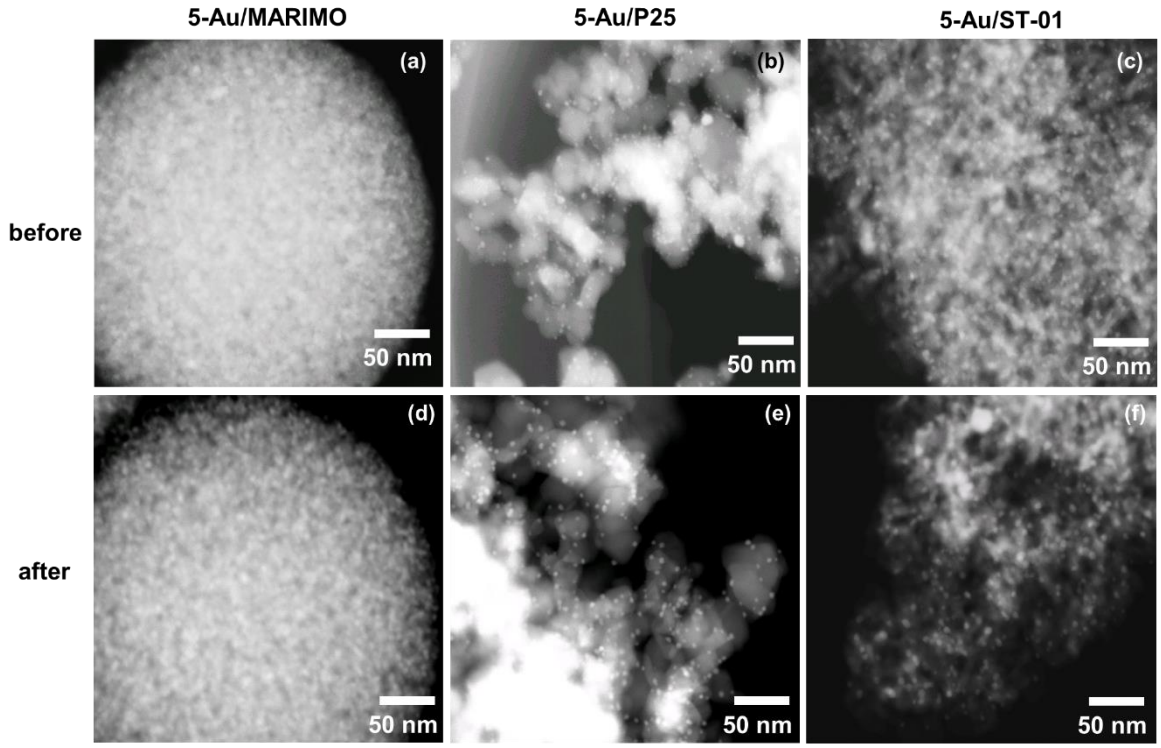

Figure 4-11. HAADF-STEM images of 5-Au/MARIMO (a, d), 5-Au-P25 (b, e), and 5-Au/ST01 (c, f) before (a, b, c), and after (d, e, f) CO oxidation at 400 °C, respectively.

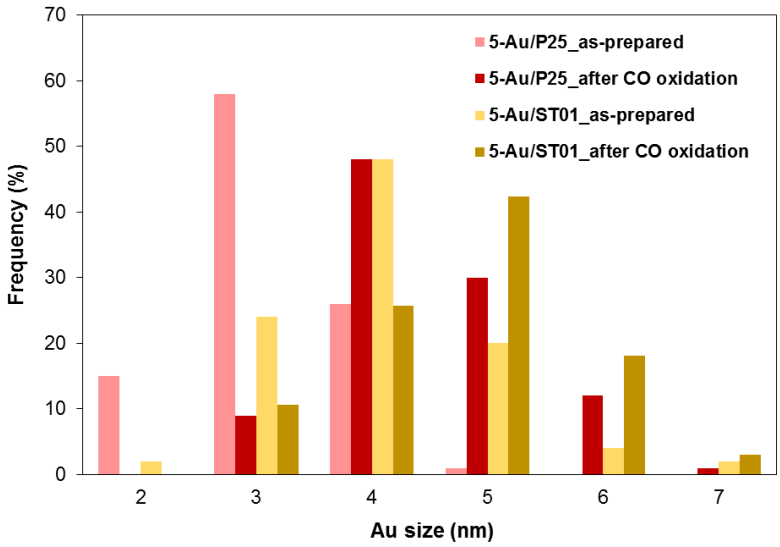

Figure 4-12. Au particle size distribution before and after CO oxidation at 400 °C.

Two important trends can be gleaned from these results: 1) the MARIMO support dispersed Au nanoparticles highly well, and as a result, they could not be observed by TEM and/or HAADF-STEM both before and after exothermic high-temperature CO oxidation, and 2) the ST-01 support having a specific surface area comparatively equal to that of MARIMO (*ca.* 300 m^2/g) also dispersed the Au nanoparticles well; however, the size of the dispersed Au nanoparticles was not very small as compared to that on the MARIMO support, which would be a reason for better low-temperature and higher CO oxidation activities of the 1-Au/MARIMO catalyst. Thus, specific surface area is not the most important factor for high performance catalyst supports.

4.3.3 Stability of the catalyst and supports

To investigate the catalyst stabilities and durabilities, the Au/TiO_2 catalysts were subjected to much severe heat stress by repeating the heating–cooling cycle (140–0 °C) of CO oxidation, in which the reactions occurred only at high temperatures (Figure 4-13). To compare between different types of the support structures with the same anatase crystalline phase of TiO_2, 1-Au/MARIMO and 1-Au/ST01 were tested by 10 heating–cooling cycles. As expected, in the case of the cycle test using the 1-Au/MARIMO catalyst, almost no significant change (0.8%) was observed in CO conversion, even after performing 10-cycle repeated test. However, an obvious decrease in CO conversion (*ca.* 35%; from 62% at the initial cycle to 40% at the last cycle) was observed for the 1-Au/ST-01 catalyst.

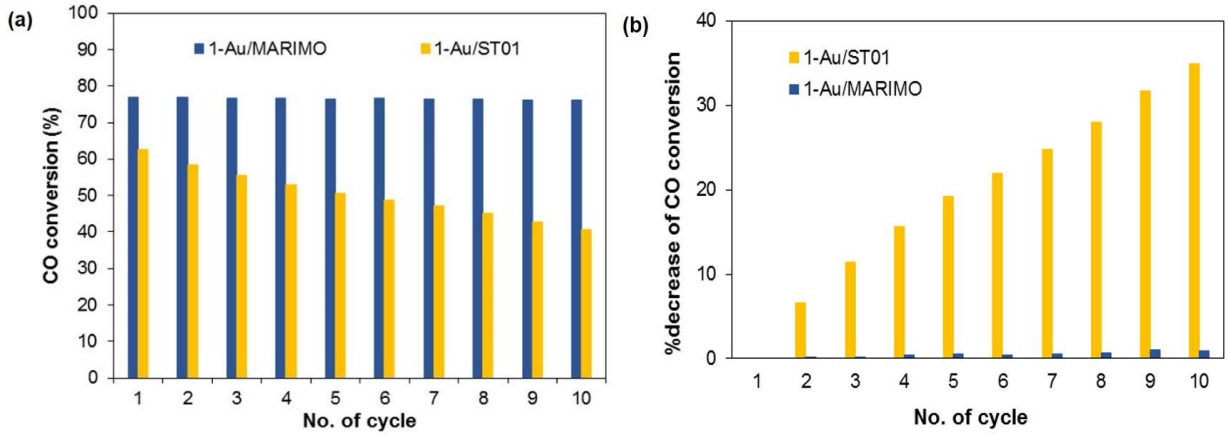

Figure 4-13. CO conversion (a), and its decrease (b) during stability test comparing between 1-Au/MARIMO and 1-Au/ST-01.

HAADF-STEM observations clearly visualized Au nanoparticle growth in the 1-Au/ST-01 catalyst (Figure 4-14), while only a small amount of grown Au nanoparticles were observed in the 1-Au/MARIMO catalyst.

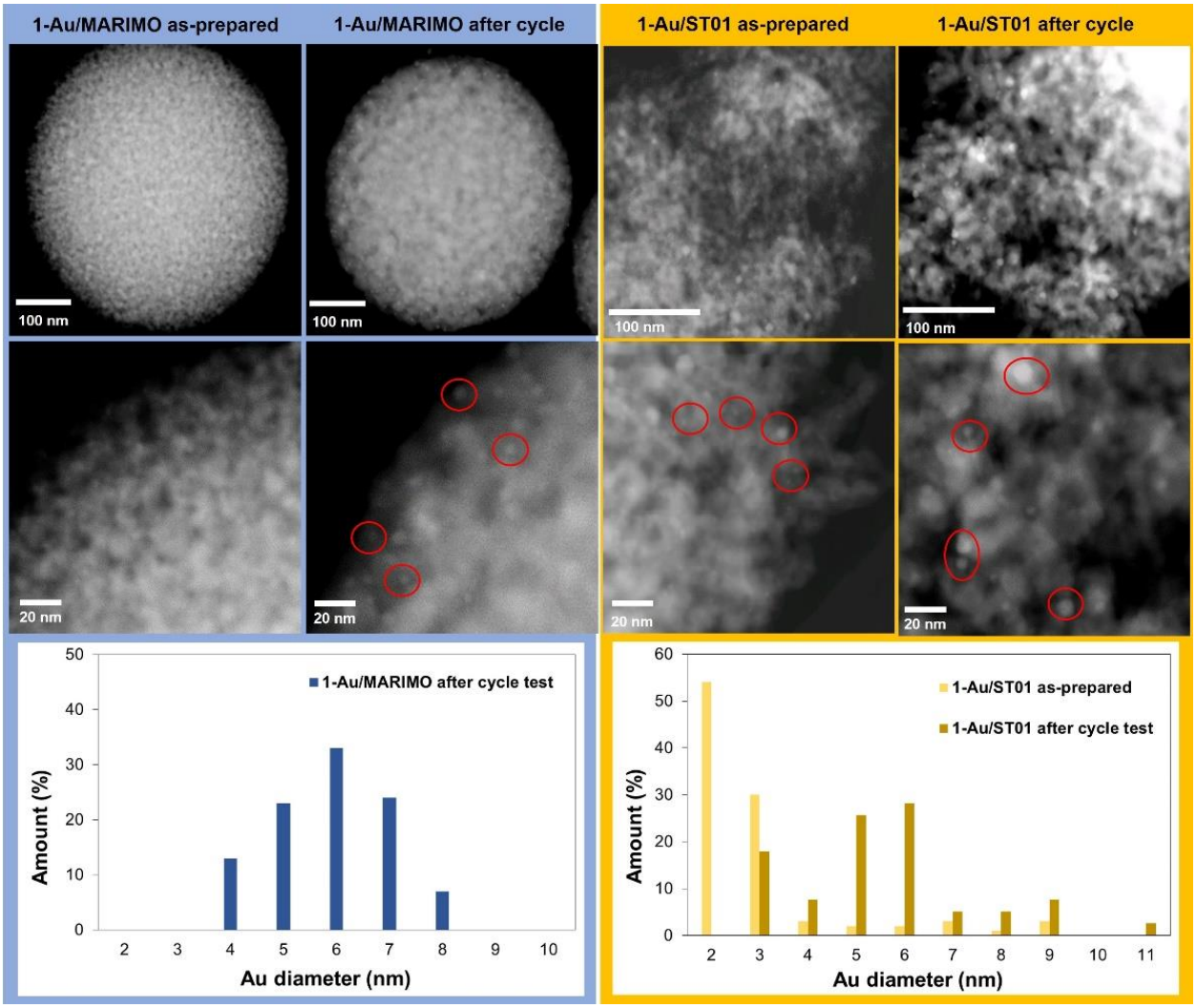

Figure 4-14. HAADF-STEM images and Au particle size distribution comparing between 1-Au/MARIMO and 1-Au/ST-01 before and after stability test.

Although the size distribution graph (Figure 4-14) of Au/MARIMO shows the existence of quite large particles (~8 nm) of Au catalyst after the test, there should exist much amount of very small size Au catalysts that were unable to be observed by the HAADF-STEM due to the limitation of the measurement caused by the distraction from the support structure. However, EDX measurement in Figure 4-15a clearly indicates the existence of higher amount of Au even after the cycle test. However, Au loading on ST-01 support after the cycle test (Figure 4-15b) showed comparatively lower than that of as-prepared sample (Table 4-1), suspecting leaching of the catalyst on ST-01 support could occur during the cycle test. On the contrary, the MARIMO support kept almost constant amount Au loading even after the cycle test, indicating excellent stability of Au/MARIMO during several cycles of reaction.

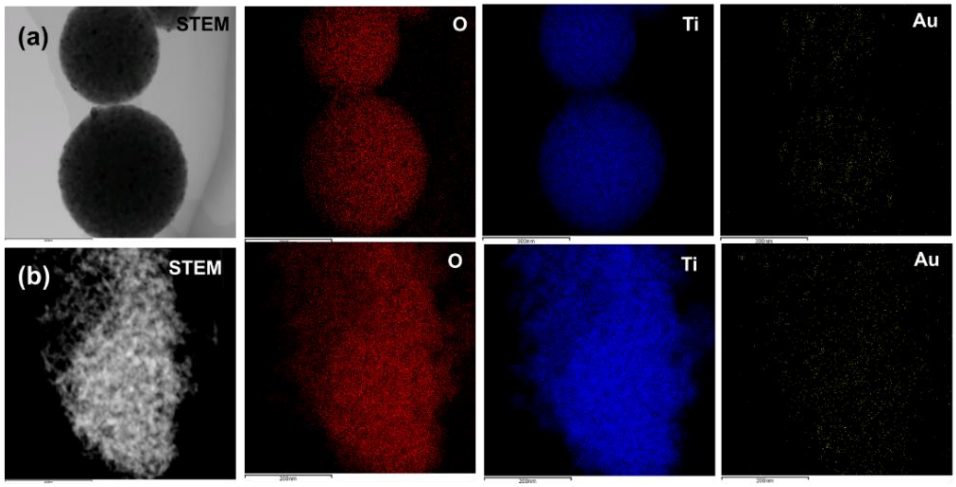

1-Au/MARIMO

	Weight.%	Atomic%
O	38.0	65.2
Ti	60.1	34.5
Au	1.91	0.27

1-Au/ST01

	Weight.%	Atomic%
O	48.8	74.3
Ti	50.3	25.6
Au	0.97	0.12

Figure 4-15. STEM, HAADF-STEM images and EDX mappings of 1wt% Au/TiO_2 after stability tests.

The following generalizations can be derived from these results: 1) the nanometer-scale concave-convex structure on the support surface dispersed the Au nanoparticles so well as in nanometer scale, and 2) high catalytic activity and sintering resistance of the Au/TiO_2 catalyst in CO oxidation are derived from not only because of the large surface area of the catalyst support but also because of the peculiar surface structures with the ultrafine concave-convex particle structure.

Additionally, a stability test of the reference commercially available WGC 1-Au/TiO_2 was investigated. The result of the test and the morphology of the catalyst before and after the cycle test can be found in Figure 4-16 and 4-17, respectively. The CO conversion showed a slightly observable decrease during several cycles of reactions (Figure 4-16). In the same time, the sintering of Au nanoparticles to become larger size were observed as shown in the red circle indicated in HAADF-STEM image (Figure 4-17). Size distribution histograms also confirmed the slight increase of the observed Au nanoparticle size.

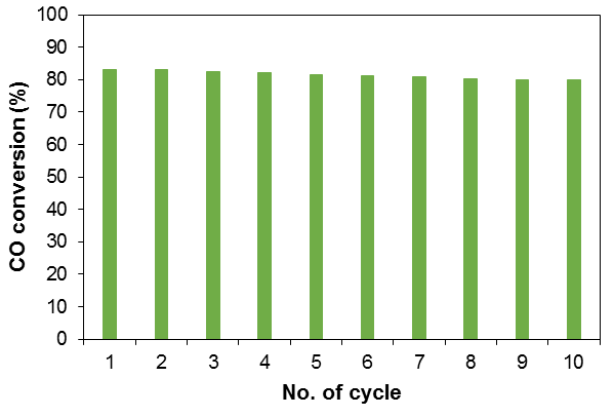

Figure 4-16. CO conversion during stability test using WGC 1-Au/TiO_2 Catalyst.

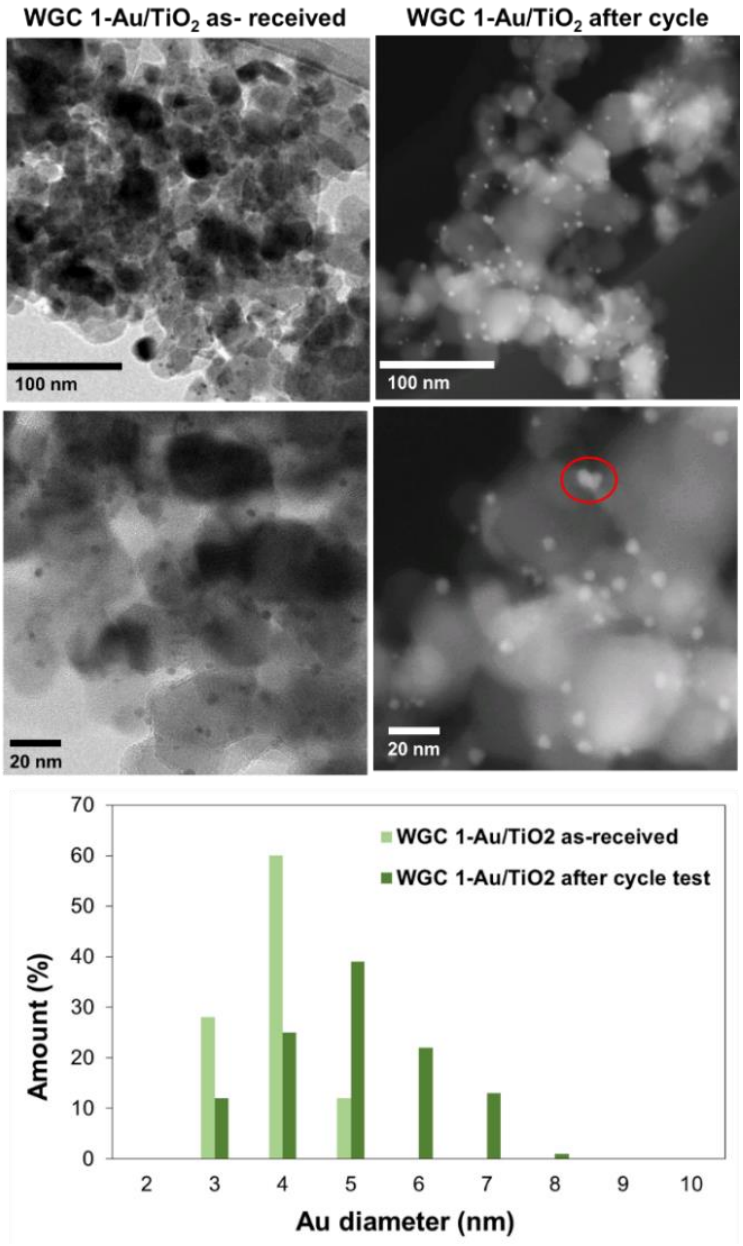

Figure 4-17. HAADF-STEM images and Au particle size distribution before and after stability test of WGC 1-Au/TiO_2.

Conclusions

MARIMO TiO_2 NP assemblies with a nanometer-scale concave-convex structure synthesized by one-pot solvothermal method was used as the catalyst support of Au nanoparticles, where the Au NPs were loaded on the support by Haruta's deposition-precipitation method. Larger amounts and better dispersion of Au nanoparticles on the MARIMO TiO_2 support were observed directly by TEM, HAADF-STEM, and EDX measurements as compared with those observed with commercially available P25 TiO_2. The MARIMO TiO_2-supported Au nanoparticle catalyst exhibited higher CO conversion at a wider temperature range than those of Au nanoparticle catalysts supported on commercially available ST-01 TiO_2. The MARIMO TiO_2-supported Au nanoparticle catalyst also showed excellent stability and durability that prevented the sintering of Au nanoparticles compared to the result obtained with other kinds of support structures as confirmed by the CO oxidation cycle test.

References

[1] Haibao H., and Dennis L.Y.C. Complete Oxidation of Formaldehyde at Room Temperature Using TiO_2 Supported Metallic Pd Nanoparticles, *ACS Catal.*, **2011**, 1, 348-354.

[2] Yan Z., Xu Z., Yu J., and Jaroniec M. Highly Active Mesoporous Ferrihydrite Supported Pt Catalyst for Formaldehyde Removal at Room Temperature, *Environ. Sci. Technol.*, **2015**, 49, 6637-6644.

[3] Wang S., Zhao C., Wang D., Wang Y., and Liu F. ˙OH-initiated heterogeneous oxidation of methyl orange using an Fe–Ce/MCM-41 catalyst, *RSC Adv*, 2016, **6**, 18800-18808.

[4] Zheng B., Wu S., Yang X., Jia M., Zhang W., and Liu G. Room Temperature CO Oxidation over $Pt/MgFe_2O_4$: A Stable Inverse Spinel Oxide Support for Preparing Highly Efficient Pt Catalyst, *ACS Appl. Mater. Interfaces*, **2016**, 8, 26683-26689.

[5] Zhao S., Hu F., and Li J. Hierarchical Core–Shell Al_2O_3@Pd-CoAlO Microspheres for Low-Temperature Toluene Combustion, *ACS Catal.*, **2016**, 6, 3433-3441.

[6] Zhong H., Iguchi M., Song F.-Z, Chatterjee M., Ishizaka T., Nagao I., Xu Q., and Kawanami H. Automatic high-pressure hydrogen generation from formic acid in the presence of nano-Pd heterogeneous catalysts at mild temperatures, *Sustainable Energy Fuels*, **2017**, 1, 1049-1055.

[7] Zhang T., Wu J., Wang X., Ni J., Li Y., and Niemantsverdriet J.W. Cobalt and cobalt carbide on alumina/NiAl(110) as model catalysts, *Catal. Sci. Technol.*, **2017**, **0000**

[8] Wang D., Xuan L., Zhong H., Gong Y., Shi X., Ye F., Li Y., and Jiang Q. Incorporation of well-dispersed calcium phosphate nanoparticles into PLGA electrospun nanofibers to enhance the osteogenic induction potential, *RSC Adv*., **2017**, 7, 23982-23993.

[9] Kuzuya A., and Ohya Y. DNA nanostructures as scaffolds for metal nanoparticles, *Polym. J.*, **2012**, 44, 452-460.

[10] Yun G., Hassan Z., Lee J., Kim J., Lee N.-S., Kim N. H., Baek K., Hwang I., Park C. G., and Kim K. Highly Stable, Water-Dispersible Metal-Nanoparticle-Decorated Polymer

Nanocapsules and Their Catalytic Applications, *Angew. Chem. Int. Ed.*, **2014**, 53, 6414-6418.

[11] Zhang L., Chang C., Hsu C.-W., Chang C.-W, and Lu S.-Y. Hollow nanocubes composed of well-dispersed mixed metal-rich phosphides in N-doped carbon as highly efficient and durable electrocatalysts for the oxygen evolution reaction at high current densities, *J. Mater. Chem. A*, **2017**, 5, 19656-19663.

[12] Liz-Marzan L. M., and Lado-Tourino I. Reduction and Stabilization of Silver Nanoparticles in Ethanol by Nonionic Surfactants, *Langmuir*, **1996**, 12, 3585-3589.

[13] Swami A., Kumar A., and Sastry M. Formation of Water-Dispersible Gold Nanoparticles Using a Technique Based on Surface-Bound Interdigitated Bilayers, *Langmuir*, **2013**, 19, 1168-1172.

[14] Yarulin A., Yuranov I., Cardenas-Lizana F., Abdulkin P., Kiwi-Minsker L. Size-Effect of Pd-(Poly(*N*-vinyl-2-pyrrolidone)) Nanocatalysts on Selective Hydrogenation of Alkynols with Different Alkyl Chains, *J. Phys. Chem. C*, **2013**, 117, 13424-13434.

[15] Perez-Mayoral E., Calvino-Casilda V., and Soriano E. Metal-supported carbon-based materials: opportunities and challenges in the synthesis of valuable products, *Catal. Sci. Technol.*, **2016**, 6, 1265-1291.

[16] Zhang Z., and Wang Z. Diatomite-Supported Pd Nanoparticles: An Efficient Catalyst for Heck and Suzuki Reactions, *J. Org. Chem.*, **2006**, 71, 7485-7487.

[17] Liu P., He H., Wei G., Liu D., Liang X., Chen T., Zhu J., and Zhu R. An efficient catalyst of manganese supported on diatomite for toluene oxidation: Manganese species, catalytic

performance, and structure-activity relationship, *Microporous Mesoporous Mater*., **2017**, 239, 101-110.

[18] Moteki T., Murakami Y., Noda S., Maruyama S., and Okubo T. Zeolite Surface As a Catalyst Support Material for Synthesis of Single-Walled Carbon Nanotubes, *J. Phys. Chem. C,* **2011**, 115, 24231-24237.

[19] Liu L., Wu Y., Hu J., Liu D., Zachariah M. R. Zeolite-Supported Iron Oxides as Durable and Selective Oxygen Carriers for Chemical Looping Combustion, *Energy Fuels,* **2017**, 31, 11225-11233.

[20] Lee S., Seo J., and Jung W.C. Sintering-resistant Pt@CeO_2 nanoparticles for high-temperature oxidation catalysis, *Nanoscale*, **2016**, 8, 10219-10228

[21] Xiang S., Zhou Y., Zhang Y., Zhang Z., Sheng X., Zhou S., and Yang Z. A highly reactive and enhanced thermal stability nanocomposite catalyst based on Au nanoparticles assembled in the inner surface of SiO_2 hollow nanotubes, *Dalton Trans*., **2014**, 43, 11039-11047.

[22] Liu J., Ji Q., and Imai T. Sintering-Resistant Nanoparticles in Wide-Mouthed Compartments for Sustained Catalytic Performance, *Sci. Rep.*, **2017**, 7, 41773

[23] Trimm D.L. The regeneration or disposal of deactivated heterogeneous catalysts, *Appl. Catal. A,* **2001**, 212, 153-160.

[24] Thomas H.W., Andrew D.T., Sivakumar C.R., and Abhaya D.K. Sintering of Catalytic Nanoparticles: Particle Migration or Ostwald Ripening?, *Acc. Chem. Res.,* **2013**, 46, 1720-1730.

[25] Bartholonew C.H. Mechnisms of catalyst deactivation, *Appl. Catal. A*, **2001**, 212, 17-60.

[26] Forzatti P., and Lietti L. Catalyst deactivation, *Catal.Today*, **1999**, 52, 165-181.

[27] Cao A., Lu R., and Veser G. Stabilizing metal nanoparticles for heterogeneous catalysis, *Phys. Chem. Chem. Phys.*, **2010**, 12, 13499-13510.

[28] Suryanarayanan V., Nair A.S., Tom R.T., and Pradeep T. Porosity of core–shell nanoparticles, *J. Mater. Chem.*, **2004**, 14, 2661-2666.

[29] Guo M., Lan G., Peng J., Li M., Yang Q., and Li C. Enhancing the catalytic activity of Ru nanoparticles deposited with carbon species in yolk–shell nanostructures, *J Mater Chem A*, **2016**, 4, 10956-10963.

[30] Sudheeshkumar V., Shivhare A., and Scott R.W.J. Synthesis of sinter-resistant Au@silica catalysts derived from Au_{25} clusters, *Catal. Sci. Technol.*, **2017**, 7, 272-280.

[31] Savva I., Kalogirou A.S., Chatzinicolaou A., Papaphilippou P., Pantelidou A., Vasile E., Vasile E., Koutentis P.A., and Christoforou T.K. PVP-crosslinked electrospun membranes with embedded Pd and Cu_2O nanoparticles as effective heterogeneous catalytic supports, *RSC Adv.*, **2014**, 4, 44911-44921.

[32] Moreno C., Divins N.J., Gazques J., Varela M., Angurell I., and Llorca J. Improved thermal stability of oxide-supported naked gold nanoparticles by ligand-assisted pinning, *Nanoscale*, **2012**, 4, 2278-2280.

[33] Xu Y., Zhang Y., Zhou Y., Zhang Z., Xiang S., Sheng X., Wang Q., and Zhang C. Synthesis of a hierarchical SiO_2/Au/CeO_2 rod-like nanostructure for high catalytic activity and recyclability, *RSC Adv.*, **2015**, 5, 34549-34556.

[34] Kondo T., Morimura T., Tsujimoto T., Aikawa T., and Yuasa M. Platinum Nanoparticle-embedded Porous Diamond Spherical Particles as an Active and Stable Heterogeneous Catalyst, *Sci. Rep*., **2017**, 7, 8651.

[35] Cho J., L Xu., Jo C., and Ryoo R. Highly monodisperse supported metal nanoparticles by basic ammonium functionalization of mesopore walls for industrially relevant catalysis, *Chem. Commun.*, 2017, **53**, 3810-3813

[36] Xu Y., Wang T., He Z., Zhong A., and Huang K. Well-dispersed gold nanoparticles anchored into thiol-functionalized hierarchically porous materials for catalytic applications, *Microporous Mesoporous Mater.*, 2016, **229**, 1-7

[37] Jiang H.-L., Liu B., Akita T., Haruta M., Sakurai H., and Xu Q. Au@ZIF-8: CO Oxidation over Gold Nanoparticles Deposited to Metal−Organic Framework, *J. Am. Chem. Soc.*, **2009**, 131, 11302-11303.

[38] Wang P., Ueno K., Takigawa H., and Kobiro K. Versatility of one-pot, single-step synthetic approach for spherical porous (metal) oxide nanoparticles using supercritical alcohols, *J. Supercrit. Fluids* **2013**, 78, 124-131.

[39] *The 20th Annual Meeting of Kochi Chemical Society*, Aug. 29, 2015.

[40] Zhen M., and Sheng D., in Heterogeneous Gold Catalysts and Catalysis, RSC 2015

[41] Hollemann A.F., Wiberg N., in Lehrbuch der Anorganischen Chemie. Walter de Gruyter, Berlin, **1995**

[42] Tsubota S., Haruta M., Kobayashi T., Ueda A., and Nakahara Y., in Preparation of Catalysts, Vol. V, eds. G. Poncelet, P.A. Jacobs, P. Grange and B. Delmon (Elsevier, Amsterdam, **1991**) p. 695.

[43] Signoretto M., Menegazzo F., Trevisan V., and Pinna F., in Gold Catalysis: Preparation, Characterization, and Applications, ed. Prati L. and Villa A., Pan Standford Publishing Pte. Ltd., Singapore, **2016**, 253-283.

CHAPTER V

Conclusions and Recommendations

Summary of the results

- Morphology controlled TiO_2 nanoparticle assemblies
  - Unique nanofiber bundles of TiO_2 with cheek brush morphology were easily obtained by simple one-pot and single-step solvothermal method.
  - The crucial conditions to obtain the uniform cheek brush morphology were investigated and a plausible mechanism of the structure formation is proposed.
  - The brush morphology further designed the application of TiO_2 as a crosslinker in polymer hydrogel, which significant improvement of tensile strength of the hydrogel compared to using inorganic crosslinkers with different morphologies.
- Surface activation of TiO_2 nanoparticle assemblies by facile treatment.
  - Facile treatment by APPJ sufficiently removed contaminants on the prepared spherical mesoporous TiO_2 without physical damage on their surface morphologies and properties.
  - LDI-TOF MS was firstly applied for the quantification of trace amount contaminants on porous nanomaterials.
  - Photocatalytic activities of TiO_2 nanoparticle assemblies were significantly improved by helium APPJ treatment confirming the successful of surface activation by the facile treatment.

- Surface activation by deposition of metal catalyst
    - Surface roughness containing highly concave-convex structure of the prepared spherical mesoporous TiO_2 gave high metal loading and dispersion ability as compared to TiO_2 with flat surface, when the surface was deposited by metal nanoparticle.
    - The spherical mesoporous TiO_2 as a metal catalyst support provided high catalytic activity compared to those of TiO_2 with different morphology.
    - Stability of the prepared spherical mesoporous TiO_2 support effectively extended catalyst lifetime and prevented catalyst sintering.

Conclusions

TiO_2 nanoparticle assemblies with controllable morphology were prepared by the simple one-pot single-step solvothermal method and the applications of each assemblies are depended on their morphology and surface properties. TiO_2 nanoparticle assemblies with three-dimensional branch morphology named “cheek-brush” have been successfully synthesized and their growth mechanism and application as a crosslinker to improve mechanical strength of polymer hydrogel have been proposed. Surface activation was confirmed by facile treatment using atmospheric plasma on each of previously prepared spherical nanoparticles, of which photocatalytic activities were significantly improved without any change in morphology and surface properties by the treatment indicating the new surface treatment method for mesoporous materials. The assemblies having unique surface roughness from their fine primary particles showed an excellent ability as a support material for metal nanoparticle. The assembly surface provided good dispersion ability of

a metal catalyst and high stability under high temperature reaction, resulting in high catalytic activity and durability of the metal catalyst, respectively.

Recommendations for future studies

According to the tunability of the developed one-pot solvothermal reaction, the optimization of the reaction can be conduct without complication to obtain various kind of materials with different morphologies and properties. It would be able to study and prepare many kinds of interesting advanced materials for specific applications depending on their adjustable properties. Similarly, since the ability for an effective support material of the synthesized MARIMO has been proved, other metal; apart from Au metal nanoparticle as a probe material, should be studied. Also, other methods for further treatments including surface activation may be applied to enhance their precious properties and explore their wide area of applications in the future.

List of Publications and Presentations

Publications

1. **Duriyasart F.**, Hamauzu H., Ohtani M., and Kobiro K. Three-Dimensionally Branched Titanium Dioxide with Cheek-Brush Morphology: Synthesis and its Application to Polymer Composites, *ChemistrySelect* **2016**, 1, 5121-5128.
2. **Duriyasart F.**, Ohtani M., Oh J.-S., Hatta A., and Kobiro K. A new approach to surface activation of porous nanomaterials using non-thermal helium atmospheric pressure plasma jet treatment, *Chem. Commun.* **2017**, 53, 6704-6707.

Presentations in international conferences

1. **Duriyasart F.**, Hamauzu H., Ohtani M., and Kobiro K., Novel Hierachical Assemblies of TiO_2 with Cheek-brush Morphology as an Inorganic Crosslinker in Poly(*N*-isopropylalrylamide, *ISACS21 Challenge in Nanoscience*, Beijing, China, November **2016**.
2. **Duriyasart F.**, Hamauzu H., Ohtani M., and Kobiro K., Hierarchical Cheek-brush Morphology of Titanium Dioxide: Synthesis and its Effect on Tensile Strength of Nanocomposite Poly(*N*-isopropylacrylamide) Hydrogel, *The 11th SPSJ International Polymer Conference (IPC2016)*, Fukuoka, Japan **2016**.

Presentations in domestic conferences/symposiums

1. **Duriyasart F.**, Hamauzu H., Ohtani M., and Kobiro K., Synthesis of Nanofiber-bundles of Titania with Cheek-brush Morphology, *The Chemical Society of Kochi 2015 Meeting*, Kochi, August **2015**.
2. **Duriyasart F.**, Hamauzu H., Ohtani M., and Kobiro K., One-pot synthesis of titania nanofiber assemblies with cheek-brush morphology, *高知工科大学総合研究所ナノテク研シンシンポジウム 2015*, Kochi, November **2015**.
3. **Duriyasart F.**, Hamauzu H., Ohtani M., and Kobiro K., One-pot synthesis of nanofiber-bundles of TiO_2 with cheek brush-like morphology, *2016 CSJ Annual Meeting*, Kyoto, March **2016**.
4. **Duriyasart F.**, Hamauzu H., Ohtani M., and Kobiro K., Nanofiber-bundles of Titania with Cheek-brush Morphology Synthesis and Application, *2016 Joint Seminar KU-KUT Chemistry*, Kochi, June **2016**.
5. **Duriyasart F.**, Hamauzu H., Ohtani M., and Kobiro K., One-pot synthesis of hierarchical nanofiber assemblies of titania and their application for a hydrogel crosslinker, *Joint symposium medicine-engineering KU-KUT*, Kochi, June **2016**
6. **Duriyasart F.**, Ohtani M., and Kobiro K., Surface Treatment of Nanoassemblies by Non-thermal Helium Plasma Jet, *The Chemical Society of Kochi 2016 Meeting*, Kochi, August **2016**.
7. **Duriyasart F.**, Ohtani M., and Kobiro K., Photocatalytic activity enhancement of one-pot synthesized titania by facile non-thermal helium atmospheric plasma treatment, *2017 CSJ Annual Meeting*, Yokohama, March **2017**.

8. **Duriyasart F.**, Ohtani M., and Kobiro K., Catalytic performance of Au on highly uneven surface TiO_2 mesoporous nanoparticle assemblies, *The Chemical Society of Kochi 2017 Meeting*, Kochi, August **2017**.
9. **Duriyasart F.**, Toru I., Kahoko H., Ohtani M., and Kobiro K., Preparation of supported noble metal catalysts on porous metal oxide nanoparticle assemblies with highly indented surface, *第11回触媒道場*, Kochi, September **2017**.
10. **Duriyasart F.**, Kahoko H., Ohtani M., and Kobiro K., High Surface Roughness of Mesoporous Nanoassembly of TiO_2 for Supporting Well-dispersed Au Nanocatalyst, *高知工科大学総合研究所ナノテク研シンシンポジウム 2015*, Kochi, November **2017**.

Awards

1. CSJ Student Award 2016, **Duriyasart F.**, Hamauzu H., Ohtani M., and Kobiro K., One-pot synthesis of nanofiber-bundles of TiO_2 with cheek brush-like morphology, *2016 CSJ Annual Meeting*, Kyoto, March **2016**.
2. Poster Award, **Duriyasart F.**, Kahoko H., Ohtani M., and Kobiro K., High Surface Roughness of Mesoporous Nanoassembly of TiO_2 for Supporting Well-dispersed Au Nanocatalyst, *高知工科大学総合研究所ナノテク研シンシンポジウム 2015*, Kochi, November **2017**.

APPENDICES

APPENDIX A

Size calculation of cheek-brush TiO_2

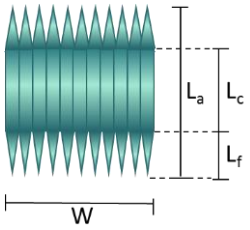

1. $Ti(O^iPr)_4$ + dimethyl phthalate (5.4 °C/min, 300 °C, 10 min)

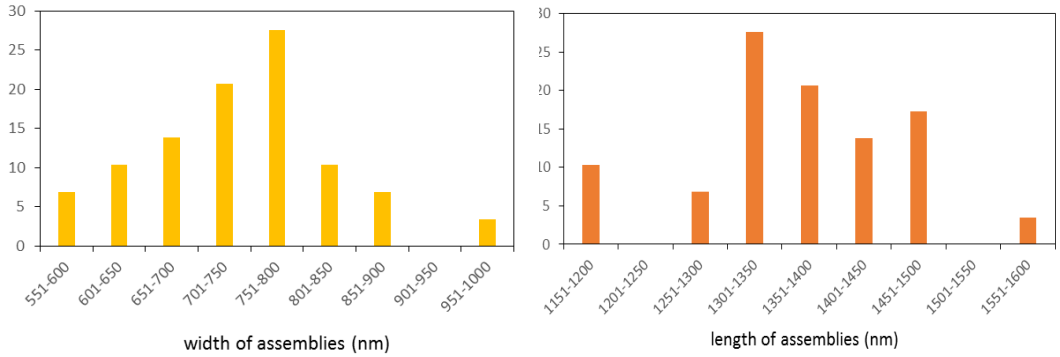

ID	Width, W (nm)	Length, L_a (nm)	Core length, L_c (nm)	Fiber length, L_f (nm)	W/L_a	W/L_c	L_f/L_c	L_c/L_a
1	763.259	1401.563	661.176	370.19	0.54	1.15	0.56	0.47
2	822.024	1426.65	671.797	377.43	0.58	1.22	0.56	0.47
3	595.426	1433.602	668.935	382.33	0.42	0.89	0.57	0.47
4	884.62	1558.468	599.045	479.71	0.57	1.48	0.80	0.38
5	770.447	1364.069	674.886	344.59	0.56	1.14	0.51	0.49
6	619.095	1399.576	655.595	371.99	0.44	0.94	0.57	0.47
7	753.39	1283.196	621.013	331.09	0.59	1.21	0.53	0.48
8	742.772	1392.978	718.514	337.23	0.53	1.03	0.47	0.52
9	605.549	1337.89	656.501	340.69	0.45	0.92	0.52	0.49
10	767.355	1385.802	714.895	335.45	0.55	1.07	0.47	0.52
11	614.54	1391.173	614.54	388.32	0.44	1.00	0.63	0.44
12	790.525	1332.285	592.651	369.82	0.59	1.33	0.62	0.44
13	568.356	1314.975	684.072	315.45	0.43	0.83	0.46	0.52
14	748.569	1481.628	625.91	427.86	0.51	1.20	0.68	0.42
15	851.504	1459.637	682.054	388.79	0.58	1.25	0.57	0.47
16	795.125	1374.939	740.148	317.40	0.58	1.07	0.43	0.54
17	687.145	1186.579	597.419	294.58	0.58	1.15	0.49	0.50
18	960.753	1185.303	701.157	242.07	0.81	1.37	0.35	0.59
19	835.941	1455.727	756.432	349.65	0.57	1.11	0.46	0.52
20	700.849	1331.818	585.312	373.25	0.53	1.20	0.64	0.44
21	674.726	1466.231	675.727	395.25	0.46	1.00	0.58	0.46
22	750.372	1254.45	610.172	322.14	0.60	1.23	0.53	0.49
23	736.012	1302.838	746.364	278.24	0.56	0.99	0.37	0.57
24	689.618	1433.904	696.945	368.48	0.48	0.99	0.53	0.49
25	712.131	1348.511	642.944	352.78	0.53	1.11	0.55	0.48
26	845.39	1479.365	683.993	397.69	0.57	1.24	0.58	0.46
27	670.508	1300.534	586.695	356.92	0.52	1.14	0.61	0.45
28	722.788	1186.783	582.999	301.89	0.61	1.24	0.52	0.49
29	783.763	1321.697	581.886	369.91	0.59	1.35	0.64	0.44
average	740.09	1365.25	656.20	354.52	0.54	1.13	0.55	0.48
SD	91.62	92.53	52.54	46.32	0.08	0.15	0.09	0.04

2. $Ti(O^iPr)_4$ + diethyl phthalate (5.4 °C/min, 300 °C, 10 min)

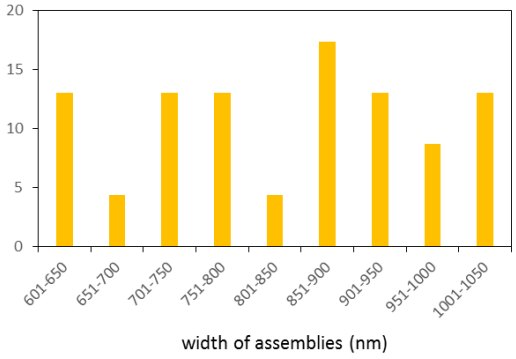

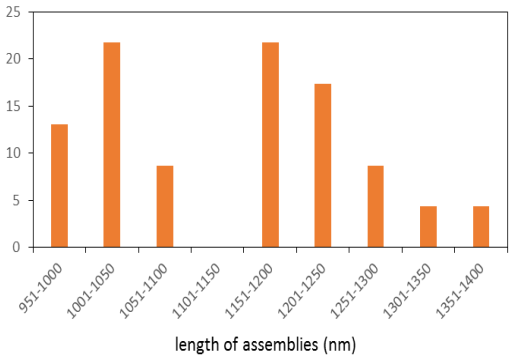

ID	Width, W (nm)	Length, L_a (nm)	Core length, L_c (nm)	Fiber length, L_f (nm)	W/L_a	W/L_c	L_f/L_c	L_c/L_a
1	629.07	1011.96	506.22	252.87	0.62	1.24	0.50	0.50
2	633.77	1027.62	516.65	255.49	0.62	1.23	0.49	0.50
3	640.43	1154.67	478.65	338.01	0.55	1.34	0.71	0.41
4	671.99	1094.62	506.86	293.88	0.61	1.33	0.58	0.46
5	709.49	1231.75	641.79	294.98	0.58	1.11	0.46	0.52
6	734.51	1197.20	611.75	292.72	0.61	1.20	0.48	0.51
7	735.03	991.94	486.49	252.73	0.74	1.51	0.52	0.49
8	775.45	1379.15	699.41	339.87	0.56	1.11	0.49	0.51
9	791.40	1150.92	561.52	294.70	0.69	1.41	0.52	0.49
10	796.74	1191.55	528.93	331.31	0.67	1.51	0.63	0.44
11	818.97	1046.30	602.02	222.14	0.78	1.36	0.37	0.58
12	865.96	1263.89	568.79	347.55	0.69	1.52	0.61	0.45
13	874.41	1096.66	613.88	241.39	0.80	1.42	0.39	0.56
14	877.98	1300.87	583.94	358.46	0.67	1.50	0.61	0.45
15	886.86	1216.63	646.69	284.97	0.73	1.37	0.44	0.53
16	908.83	1151.39	538.57	306.41	0.79	1.69	0.57	0.47
17	938.93	1033.29	483.29	275.00	0.91	1.94	0.57	0.47
18	941.85	978.91	588.91	195.00	0.96	1.60	0.33	0.60
19	952.54	999.46	638.69	180.38	0.95	1.49	0.28	0.64
20	962.57	1298.94	741.00	278.97	0.74	1.30	0.38	0.57
21	1028.81	1245.85	641.79	302.03	0.83	1.60	0.47	0.52
22	1035.32	1220.32	612.33	303.99	0.85	1.69	0.50	0.50
23	1040.56	1029.73	678.11	175.81	1.01	1.53	0.26	0.66
average	837.02	1144.07	585.92	279.07	0.74	1.44	0.49	0.51
SD	130.56	115.71	72.70	51.26	0.13	0.20	0.11	0.06

3. $Ti(O^iPr)_4$ + methyl benzoate (5.4 °C/min, 300 °C, 10 min)

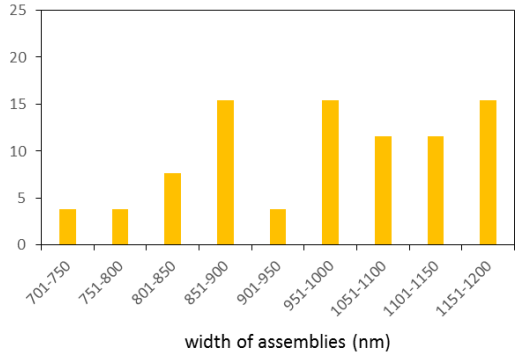

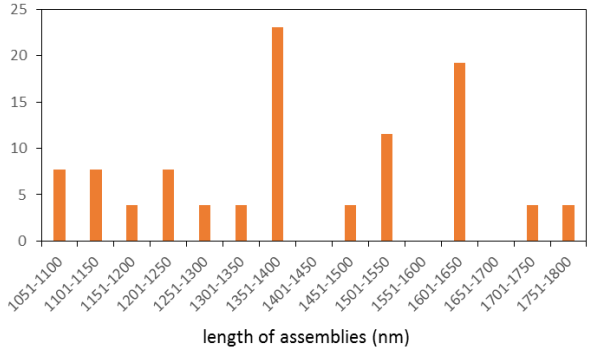

ID	Width, W (nm)	Length, L_a (nm)	Core length, L_c (nm)	Fiber length, L_f (nm)	W/L_a	W/L_c	L_f/L_c	L_c/L_a
1	981.583	1616.043	607.634	504.20	0.61	1.62	0.83	0.38
2	881.313	1360.396	663.935	348.23	0.65	1.33	0.52	0.49
3	963.401	1159.167	614.866	272.15	0.83	1.57	0.44	0.53
4	1042.753	1365.972	629.937	368.02	0.76	1.66	0.58	0.46
5	1064.624	1541.8	655.477	443.16	0.69	1.62	0.68	0.43
6	959.392	1137.478	666.851	235.31	0.84	1.44	0.35	0.59
7	1150.765	1786.096	1047.138	369.48	0.64	1.10	0.35	0.59
8	892.165	1603.569	756.286	423.64	0.56	1.18	0.56	0.47
9	1106.829	1600.018	898.757	350.63	0.69	1.23	0.39	0.56
10	1030.454	1061.074	583.003	239.04	0.97	1.77	0.41	0.55
11	1188.105	1391.272	855.363	267.95	0.85	1.39	0.31	0.61
12	835.403	1364.017	619.278	372.37	0.61	1.35	0.60	0.45
13	700.636	1207.078	631.347	287.87	0.58	1.11	0.46	0.52
14	885.66	1700.81	636.89	531.96	0.52	1.39	0.84	0.37
15	868.118	1338.249	688.543	324.85	0.65	1.26	0.47	0.51
16	799.251	1118.679	665.624	226.53	0.71	1.20	0.34	0.60
17	903.641	1450.583	705.79	372.40	0.62	1.28	0.53	0.49
18	1008.691	1602.326	659.329	471.50	0.63	1.53	0.72	0.41
19	1126.111	1374.882	703.6	335.64	0.82	1.60	0.48	0.51
20	1152.096	1366.287	696.715	334.79	0.84	1.65	0.48	0.51
21	995.367	1266.189	750.027	258.08	0.79	1.33	0.34	0.59
22	1075.631	1534.784	699.74	417.52	0.70	1.54	0.60	0.46
23	840.572	1228.343	611.022	308.66	0.68	1.38	0.51	0.50
24	1128.297	1505.478	682.697	411.39	0.75	1.65	0.60	0.45
25	1176.105	1614.986	737.905	438.54	0.73	1.59	0.59	0.46
26	1060.724	1065.513	651.021	207.25	1.00	1.63	0.32	0.61
average	992.99	1398.50	696.88	350.81	0.72	1.44	0.51	0.50
SD	129.99	203.35	101.71	87.77	0.12	0.19	0.15	0.07

4. $Ti(OBu)_4$ + dimethylphthalate (5.4 °C/min, 300 °C, 10 min)

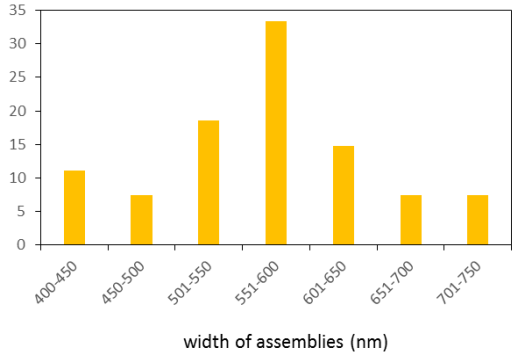

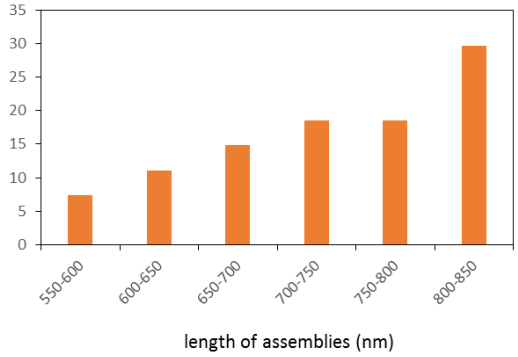

ID	Width, W (nm)	Length, L_a (nm)	Core length, L_c (nm)	Fiber length, L_f (nm)	W/L_a	W/L_c	L_f/L_c	L_c/L_a
1	703.005	816.086	370.184	222.95	0.86	1.90	0.60	0.45
2	554.789	670.911	357.258	156.83	0.83	1.55	0.44	0.53
3	624.094	649.051	615.111	16.97	0.96	1.01	0.03	0.95
4	563.726	747.233	374.609	186.31	0.75	1.50	0.50	0.50
5	444.473	709.508	434.265	137.62	0.63	1.02	0.32	0.61
6	417.97	835.326	329.154	253.09	0.50	1.27	0.77	0.39
7	585.312	813.699	359.069	227.32	0.72	1.63	0.63	0.44
8	615.463	767.777	350.694	208.54	0.80	1.75	0.59	0.46
9	539.631	849.407	356.274	246.57	0.64	1.51	0.69	0.42
10	595.38	664.193	318.05	173.07	0.90	1.87	0.54	0.48
11	586.695	713.95	411.98	150.99	0.82	1.42	0.37	0.58
12	528.143	655.595	307.863	173.87	0.81	1.72	0.56	0.47
13	706.99	846.252	477.811	184.22	0.84	1.48	0.39	0.56
14	664.355	681.42	416.156	132.63	0.97	1.60	0.32	0.61
15	571.769	717.987	321.514	198.24	0.80	1.78	0.62	0.45
16	566.213	554.643	232.457	161.09	1.02	2.44	0.69	0.42
17	567.738	714.404	291.268	211.57	0.79	1.95	0.73	0.41
18	420.034	779.338	305.926	236.71	0.54	1.37	0.77	0.39
19	539.38	558.381	307.16	125.61	0.97	1.76	0.41	0.55
20	665.656	789.67	329.154	230.26	0.84	2.02	0.70	0.42
21	540.681	806.093	266.262	269.92	0.67	2.03	1.01	0.33
22	506.948	608.398	240.792	183.80	0.83	2.11	0.76	0.40
23	647.049	619.619	294.863	162.38	1.04	2.19	0.55	0.48
24	451.29	797.737	372.657	212.54	0.57	1.21	0.57	0.47
25	568.071	827.266	417.194	205.04	0.69	1.36	0.49	0.50
26	487.44	799.395	476.962	161.22	0.61	1.02	0.34	0.60
27	626.039	820.148	365.557	227.30	0.76	1.71	0.62	0.45
average	566.23	733.83	359.27	187.28	0.78	1.64	0.56	0.49
SD	78.54	88.56	80.79	51.31	0.15	0.37	0.20	0.12

APPENDIX B

APPJ treatment on hollow spherical TiO_2 nanoparticle assemblies

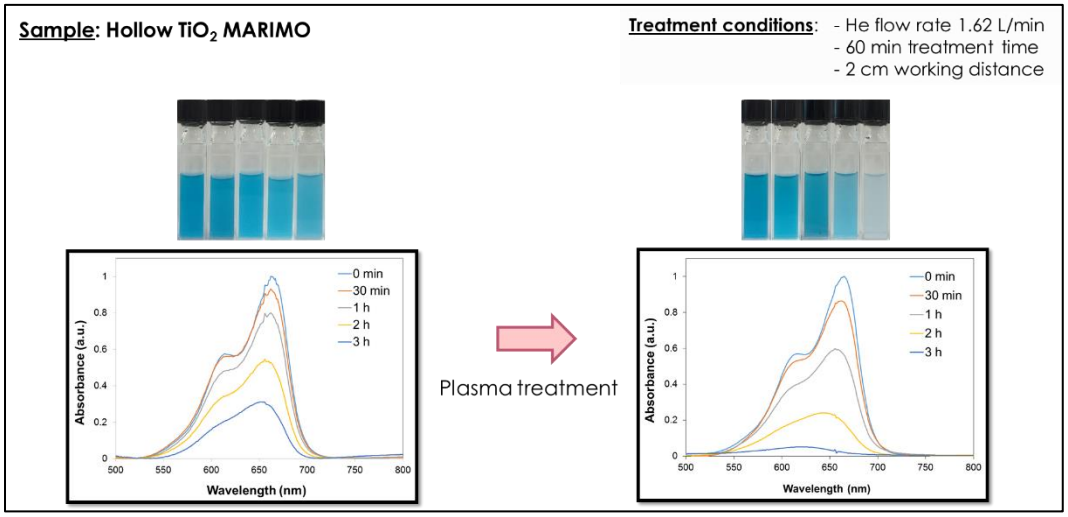

Figure B-1 Photocatalytic activity of hollow MARIMO TiO_2, before and after APPJ treatment, in methylene blue degradation.

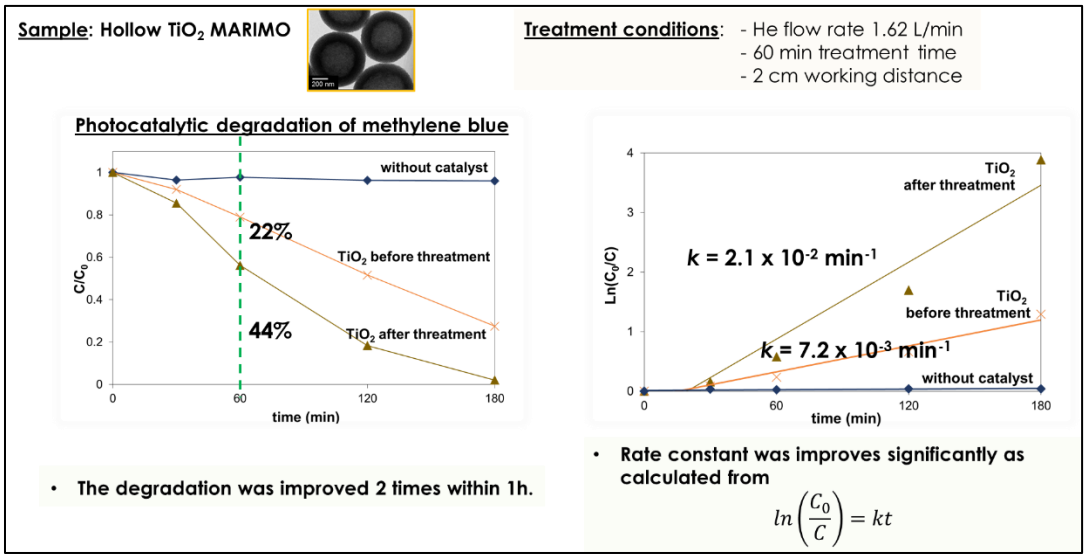

Figure B-2 Concentration and logarithmic plot of methylene blue degradation using hollow MARIMO TiO_2, before and after APPJ treatment, as photocatalysts.

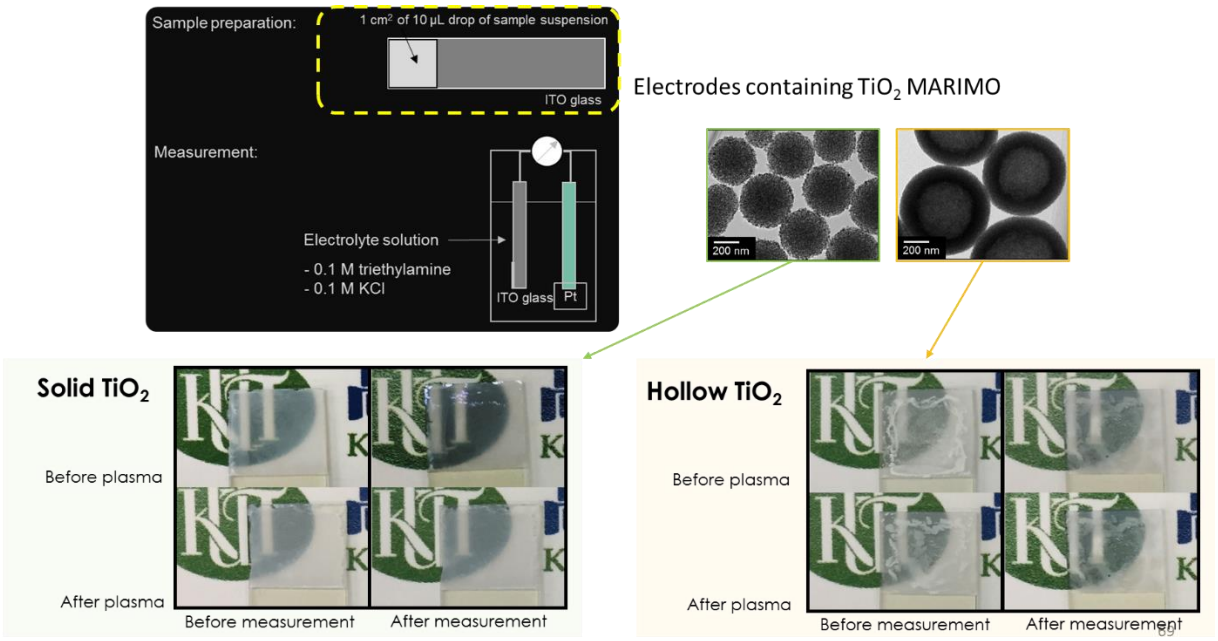

Figure B-3 Transient photocurrent response electrodes comparing between using solid and hollow MARIMO TiO_2, before and after APPJ treatment, as photocatalysts.

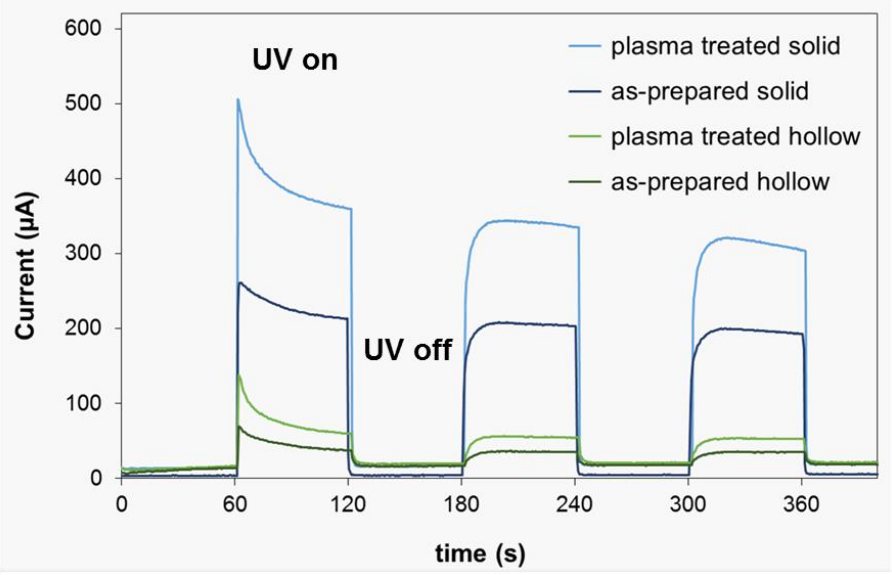

Figure B-4 Transient photocurrent responses comparing between solid and hollow MARIMO TiO_2, before and after APPJ treatment, as photocatalys.

APPENDIX C

Catalyst preparations

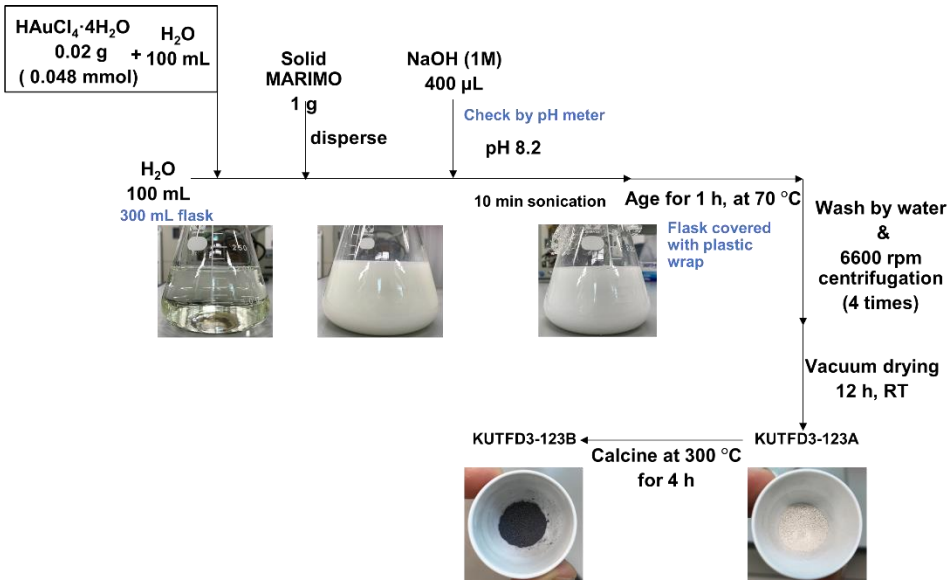

Figure C-1 An example of preparation procedure for 1-Au/MARIMO.

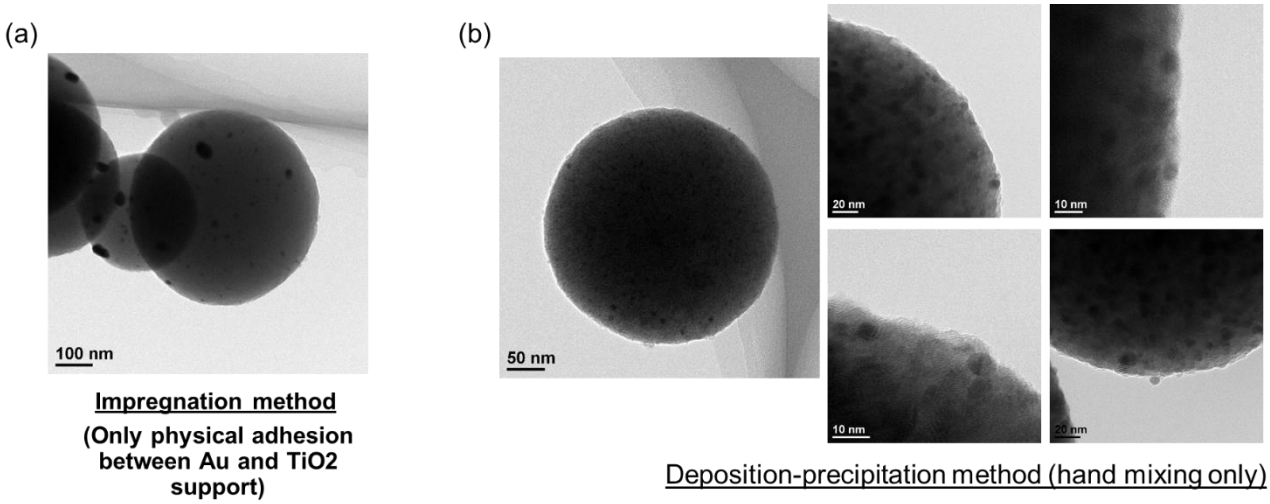

Figure C-2 TEM images showing poor Au dispersion with large size Au particles on MARIMO prepared by (a) impregnation method and (b) deposition-precipitation method without sonication mixing.

Apparatus for CO oxidation

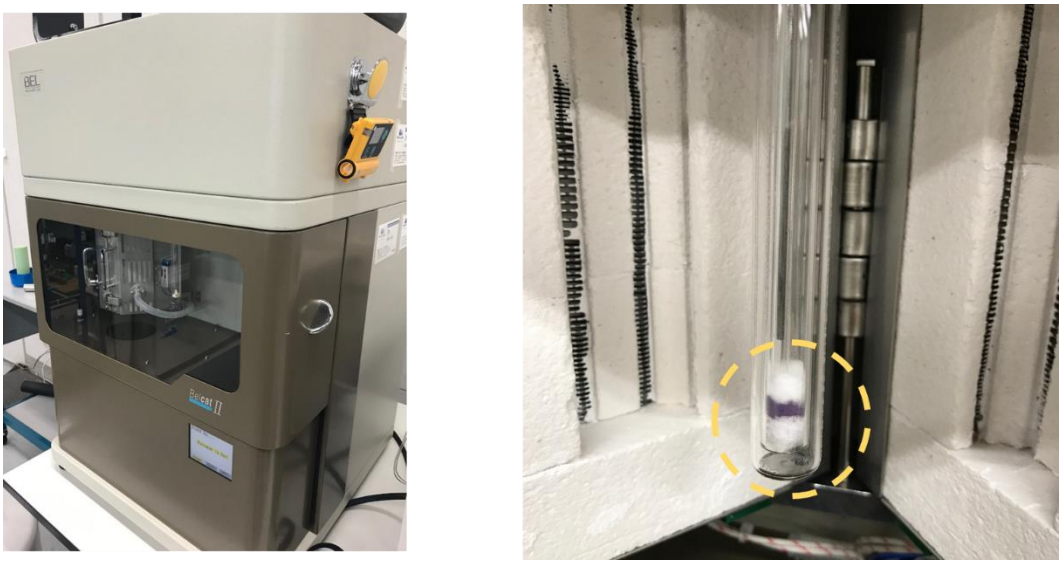

Figure C-3 Photographs of gas phase reactor for CO oxidation (BELCATII, Microtrac BEL Corp.) and the catalyst setting.

Characterization/Evaluation of catalysts after CO oxidations and stability test

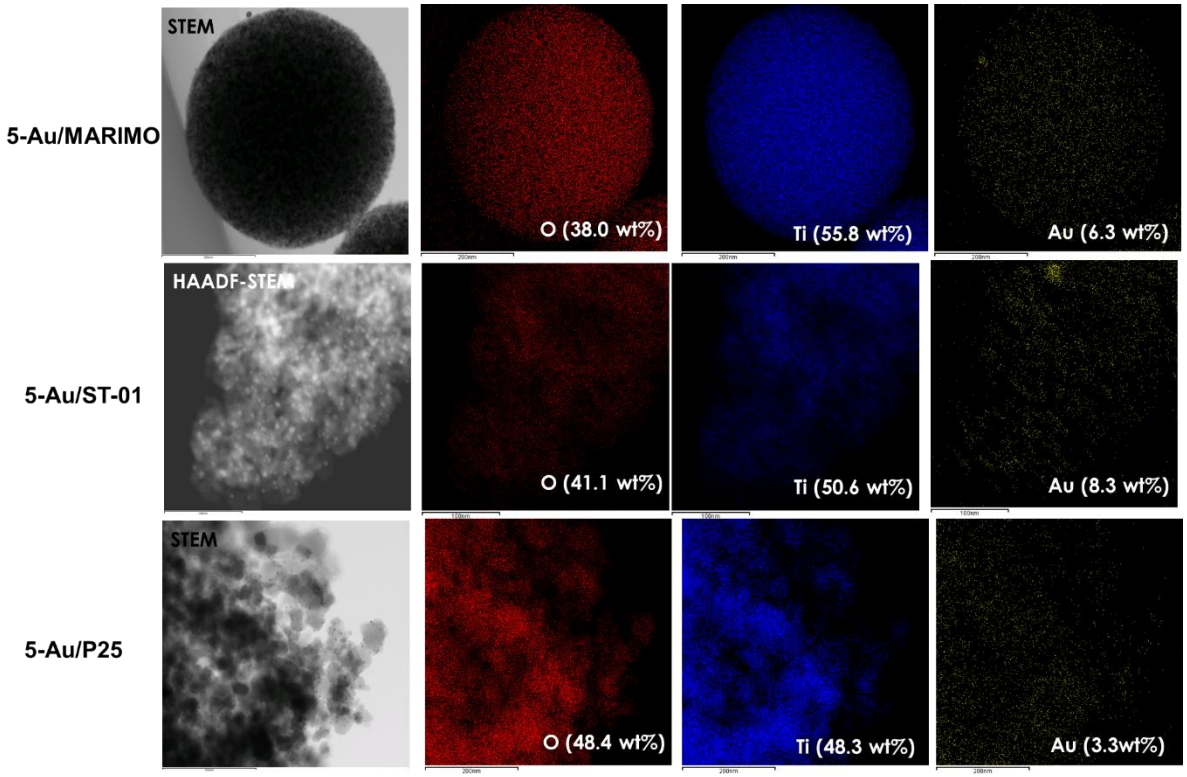

Figure C-4 HAADF-STEM images and EDX mappings of Au/TiO_2 catalysts after 400 ºC CO oxidation.

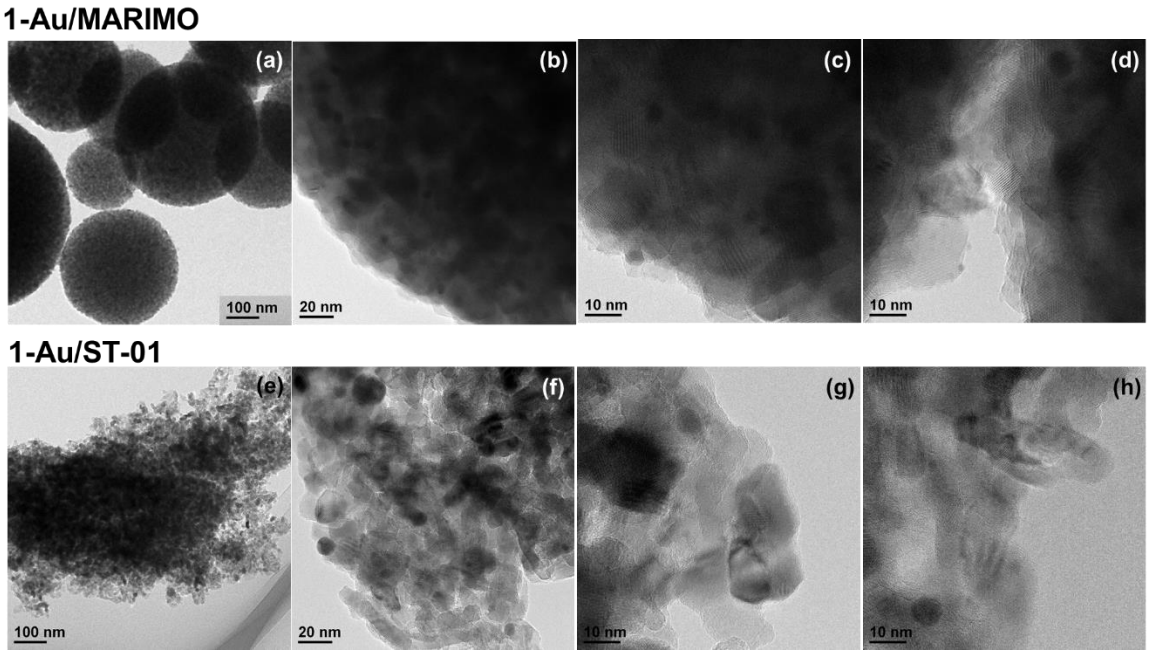

Figure C-5 TEM images of 1-Au/MARIMO (a-d) and 1-Au/ST-01 (e-h) after stability test.

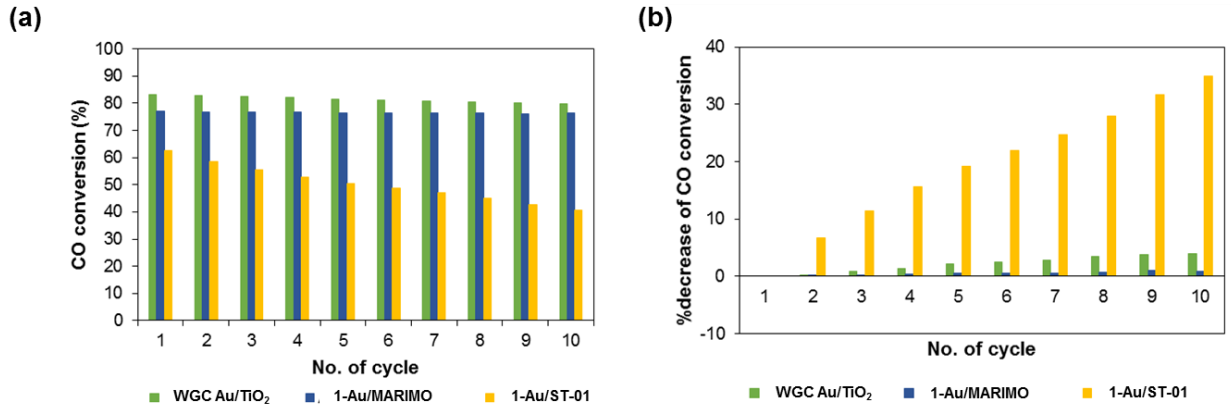

Figure C-6 CO conversion (a), and its decrease (b) during stability test using different type of Au/TiO_2.

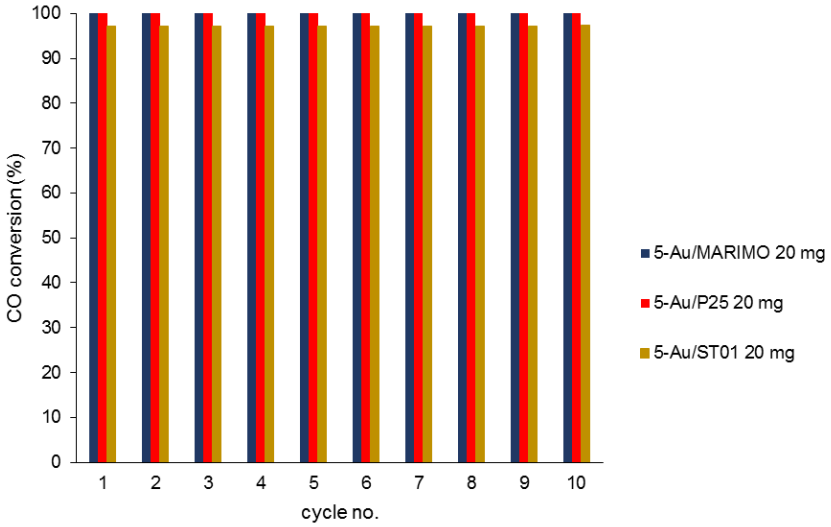

Figure C-7 CO conversion during stability test using different type of 5wt% Au/TiO_2 catalysts.

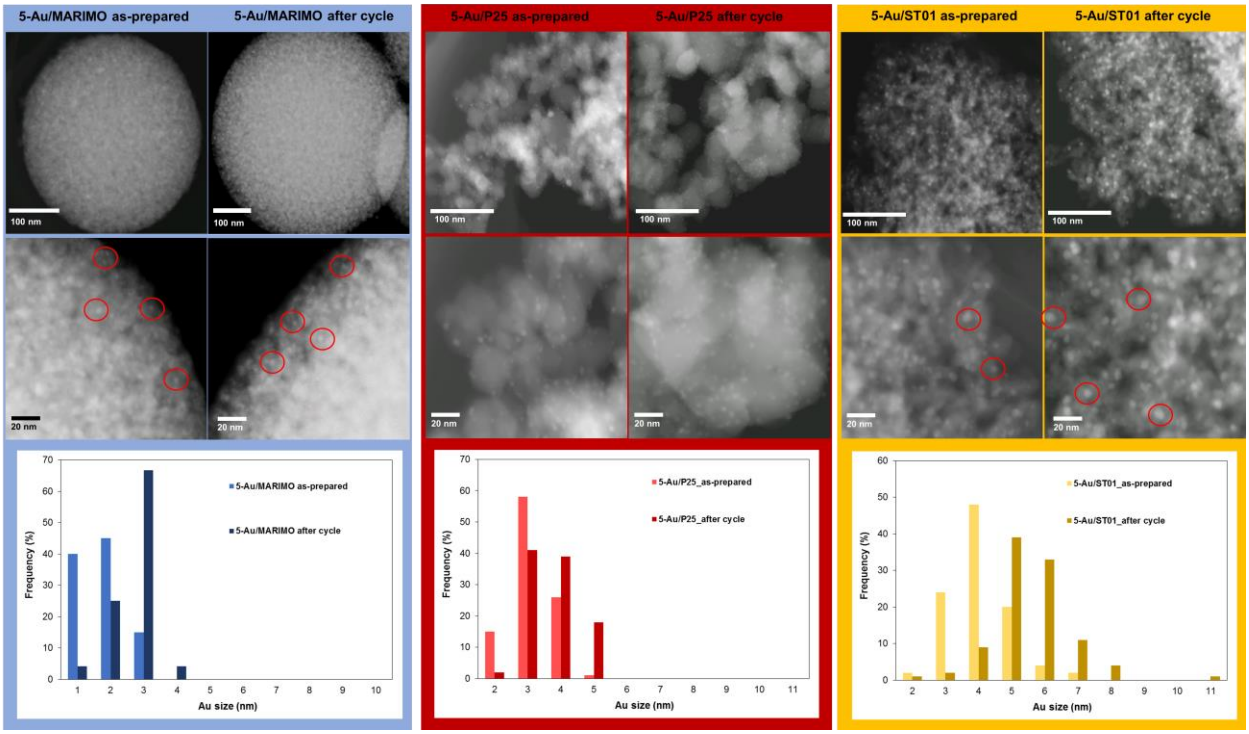

Figure C-8 HAADF-STEM images and Au particle size distribution comparing between 5-Au/MARIMO, 5-Au/P25, and 5-Au/ST-01 before and stability test.

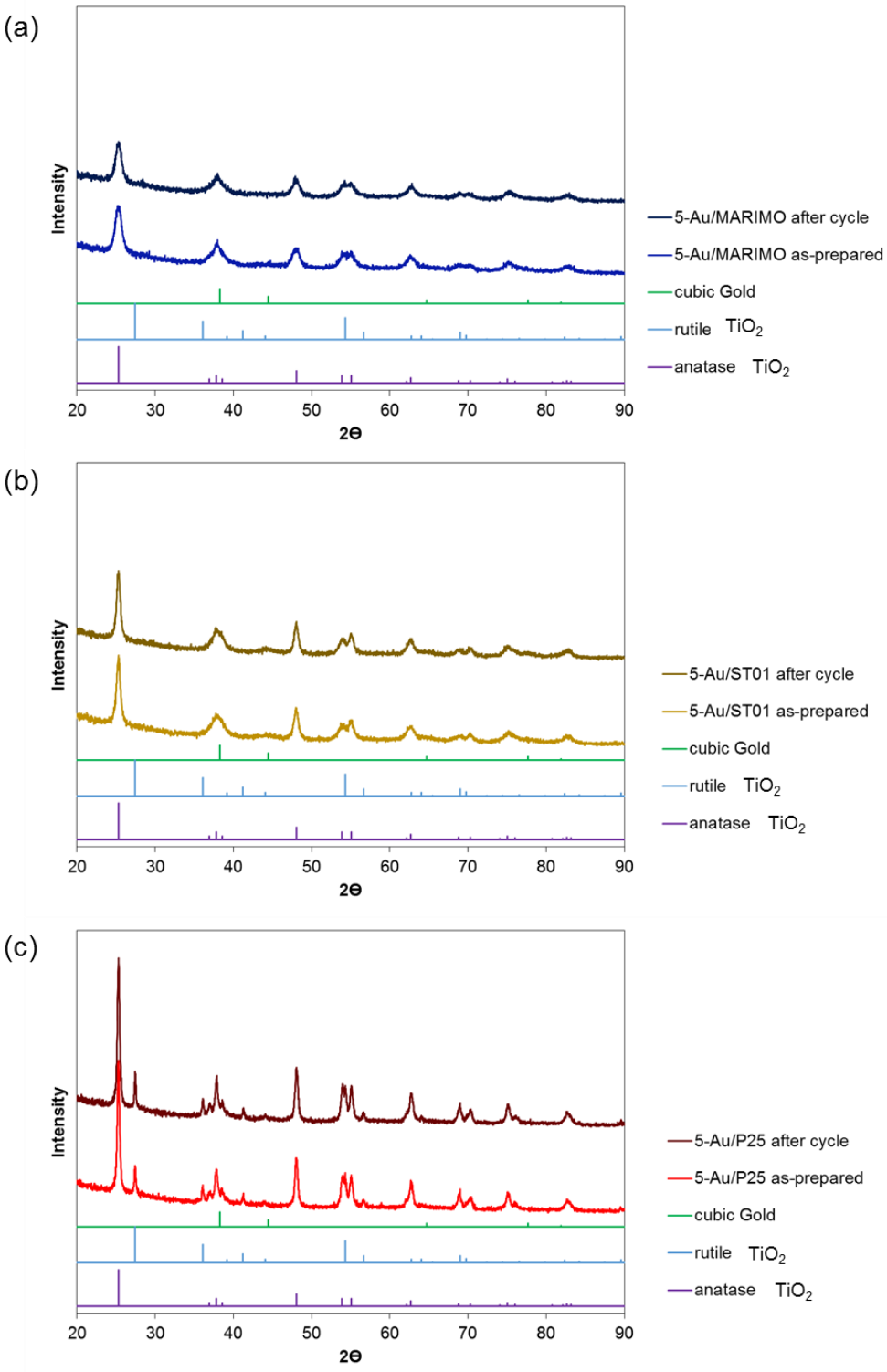

Figure C-9 X-ray diffraction patterns of 5wt% (a) Au/MARIMO, Au/ST-01, and Au/P25 comparing between as-prepared samples and the samples after stability test.